High-resolution Monte Carlo study of finite-size behavior at phase transitions in spin models

by

Jiahao Xu

(Under the Direction of David P. Landau)

Abstract

We have studied the finite-size behavior at magnetic phase transitions by using extensive Monte Carlo simulations. For the second-order transition in the simple cubic Ising model, we have investigated the critical behavior by implementing the Wolff cluster flipping algorithm and data analysis with histogram reweighting in quadruple precision arithmetic. By analyzing data with cross correlations between various thermodynamic quantities obtained from the same data pool, we have obtained the critical quantities with precision that exceeds all previous Monte Carlo estimates. For the first-order "spin-flop" transition in the 3D anisotropic Heisenberg antiferromagnet in an external field, we have explored the finite-size behavior of the transition between the Ising-like antiferromagnetic state and the canted, XY-like state. Finite-size scaling for a first-order phase transition where a continuous symmetry is broken is developed using an approximation of Gaussian probability distributions with a phenomenological "degeneracy" factor, q, included. Our theory yields $q = \pi$, and it predicts that for large linear dimension L the field dependence of all moments of the order parameters as well as the fourth-order cumulants exhibit universal intersections, where the values of these intersections can be expressed in terms of the factor q. The agreement

between our theory and high-resolution multicanonical simulation data implies a heretofore unknown universality can be invoked for first-order phase transitions.

INDEX WORDS: Monte Carlo simulations, phase transition, finite-size behavior, critical exponents, histogram reweighting, cross correlations, three-dimensional Ising model, three-dimensional Heisenberg model

High-resolution Monte Carlo study of finite-size behavior at phase transitions in spin models

by

Jiahao Xu

A Dissertation Submitted to the Graduate Faculty
of The University of Georgia in Partial Fulfillment
of the
Requirements for the Degree

Doctor of Philosophy

Athens, Georgia

2019

High-resolution Monte Carlo study of finite-size behavior at phase transitions in spin models

by

Jiahao Xu

Major Professor: David P. Landau

Committee: Heinz-Bernd Schüttler
Steven P. Lewis
Shan-Ho Tsai

Electronic Version Approved:

Suzanne Barbour
Dean of the Graduate School
The University of Georgia
August 2019

Acknowledgments

First and foremost, I would like to express my sincere appreciation to my advisor, Dr. David P. Landau, for his invaluable instructions, generous support, and great patience throughout my Ph.D. studies. I benefited a lot from his extraordinarily intelligent supervising strategies, which encouraged me to have my own independent ideas and think critically. He is not only my research advisor, but also my life mentor. He told me to be open to new technologies and learn new things as much as I can. Because one day, when there is an opportunity, I may have one more choice in my future career path.

In addition, I am grateful for Dr. Heinz-Bernd Schüttler, Dr. Steven P. Lewis and Dr. Shan-Ho Tsai for being members of my advisory committee. Their experience and suggestions provided me with unlimited help to my research and dissertation.

What's more, I would like to thank Dr. Alan M. Ferrenberg, Dr. Shan-Ho Tsai, and Dr. Kurt Binder for the excellent collaboration in my research. They are great physicists and I learned so much from them.

Also, I truly appreciate many members of the CSP. I benefited a lot from the discussion with Dr. Dilina Perera, Dr. Guangjie Shi, Mr. Alfred Farris, Mr. Matthew Wilson, Mr. Lingyun Wu, Mr. Zewen Zhang, Mr. Shengming Zhang, and Mr. Yifan Dai. I thank Mr. Mike Caplinger and Mr. Jeff Deroshia for their technical support to my office desktop and the hal system usage.

Last but not least, I would like to thank my family for their constant support and love. My parents are my first teachers and they taught me how to be a man: You can make mistakes, but you should not make the same mistakes twice!

Contents

List of Figures

List of Tables

Chapter 1

Introduction

Generally speaking, a phase in a thermodynamic system has some uniform physical properties. During a phase transition, some specific properties would change dramatically, often discontinuously. If the first derivative of the free energy ($F = k_B T \ln Z$, where k_B is the Boltzmann constant, T is the temperature, and Z is the partition function [6]) with respect to some thermodynamic variable is discontinuous at the transition point, this transition is denoted as first-order. Likewise, if the first derivative of the free energy is continuous but the second derivative is discontinuous, the transition is termed second-order. A second-order transition is usually named as a critical transition, and the temperature at which the transition takes place is called the critical temperature [1]. Fig. 1.1(a, b) describe the characteristic behaviors for a first-order phase transition, where the curves of the free energy F for the ordered and disordered states meet at the transition temperature T_{tr} with different slope values, and the internal energy $U = -T^2 \partial(F/T)/\partial T$ is separated by the latent heat at T_{tr}. In contrast, Fig. 1.1(c, d) are corresponding to a second-order phase transition, where the free energy F varies continuously at the critical temperature T_c [1].

The research on phase transitions has long been a popular area in various scientific fields. Even after many years of study, there remain open questions even for the Ising universality

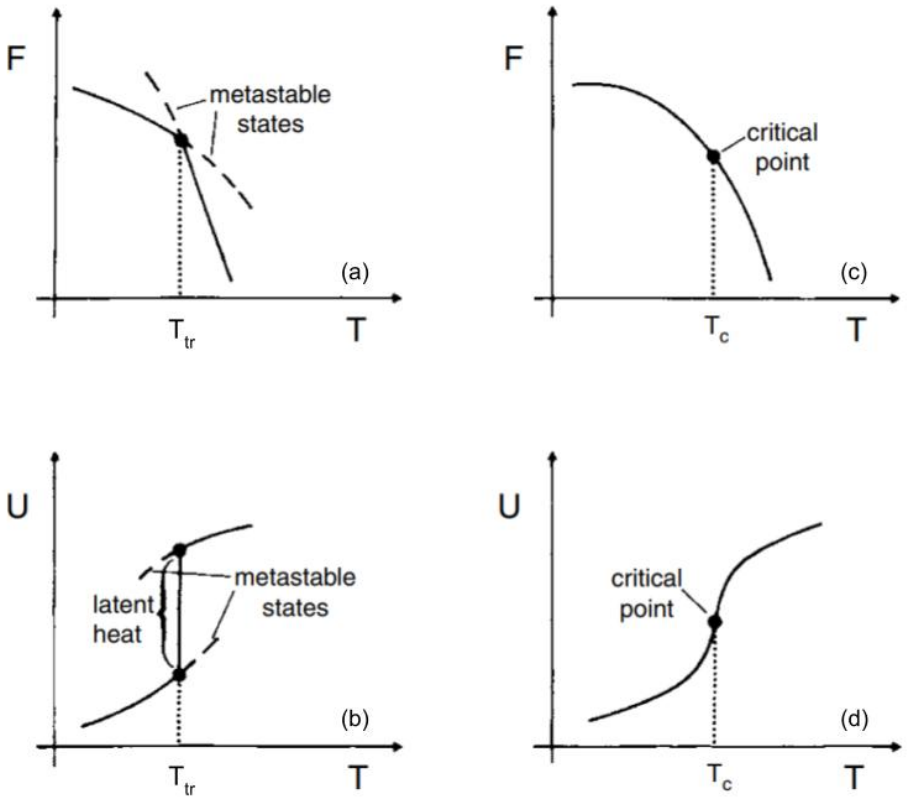

Figure 1.1: Schematic variation of the free energy F and the internal energy U with temperature T. (a, b) and (c, d) are for systems undergoing first-order and second-order phase transitions, respectively. Graph is taken from Ref [1].

class, which is a well studied case in statistical mechanics. In the past several decades, extensive effort by numerical and theoretical approaches has been under taken to understand the nature and classification of phase transitions.

In general, a phase transition is between a disordered phase and an ordered phase. To distinguish the two phases, an order parameter is a quantity of the system that is non-zero in the ordered phase while it is identically zero in the disordered phase. It changes dramatically at the transition point.

For different kinds of systems, the order parameter would be defined differently. In a ferromagnet, the spontaneous magnetization is the order parameter. In a liquid-gas system, it would be the density difference between the liquid phase and the gas phase. As for liquid crystals, it would be the degree of the orientational order [1, 6, 7].

For a second-order phase transition, it has been showed that the thermodynamic properties follow a set of power laws near the critical temperature T_c [1, 8, 9]. For example, in a magnetic system the spontaneous magnetization m, the specific heat C, the susceptibility χ, and the correlation length ξ vary as follow,

$$m \propto \varepsilon^{\beta}, \tag{1.1}$$

$$C \propto \varepsilon^{-\alpha} + b_C, \tag{1.2}$$

$$\chi \propto \varepsilon^{-\gamma} + b_\chi, \tag{1.3}$$

$$\xi \propto \varepsilon^{-\nu} \tag{1.4}$$

where $\varepsilon = |1 - T/T_c|$, b_C and b_χ are analytic background terms, and the powers are denoted as "critical exponents".

In addition, it is believed that the values of the critical exponents are the property of the system itself (such as the lattice dimension), and they are independent of the parameters contained in the model, such as the interaction coupling J, or the lattice type of the model (e.g. square or triangle). This important and striking property of second-order phase transitions is known as universality. Thus, different models in the same universality class have common critical exponents [1, 10]. (The values of critical exponents do depend on the dimension of the lattice though.)

However, the fundamental concepts mentioned above are valid only in the thermodynamic limit ($L \to L_\infty$). In a finite-size system, these properties may not hold. For example, the correlation length ξ is a quantity to describe the dimension of correlated spins in a system.

Based on Eq. (1.4), it diverges as the temperature approaches to the critical point (ν is positive). But in a system of finite size, the correlation length ξ won't be greater than the lattice dimension. This means that there is a "cut-off" in the divergence of ξ. Similar effects occur at other quantities as well. And this is called the finite-size effect [1, 7, 10]. Due to the finite-size effect, the effective transition point and the effective values of the critical exponents in a finite system would be different than those in an infinite size system. To extract the values for different thermodynamic quantities at $L \to L_\infty$, we can use finite-size scaling methods [11–14], which will be discussed in the following chapters.

Similar to a second-order transition, there exists finite-size effect in a first-order transition as well. In contrast, the above-mentioned power laws and the universality hypothesis do not hold for a first-order transition. As the correlation length does not diverge in a first-order transition, a different approach for finite-size scaling is needed.

High-resolution study of finite-size behavior at phase transitions play an important role for developing theories, and Monte Carlo simulation is one of the best suited methods for delivering quantitative information. In this work, multiple simulation algorithms (Metropolis algorithm [15], Wolff cluster flipping algorithm [16], and multicanonical sampling [17]) have been implemented based on requirements, and data for different models have been analyzed with similar techniques, such as the histogram reweighting method.

In the next chapter we will define the 3D Ising model, describe the Monte Carlo sampling method, demonstrate the histogram reweighting techniques [18, 19], cross correlation analysis [20, 21] and finite-size scaling methods [11–13, 22]. The results of high-resolution Monte Carlo simulations of critical behavior will be presented in Chapter 3. In Chapter 4 we will clearly define the 3D XXZ Heisenberg model to study the "spin-flop" transition (between the Ising-like antiferromagnetic state and the rotationally degenerate, canted XY-like state), delineate the simulation methodology used to generate data for different lattice sizes, and provide a theoretical formulation for the understanding of the finite-size behavior of this

model. In Chapter 5 we will present the results of careful simulations which are then used to test the theory. Our conclusions are summarized in Chapter 6.

Chapter 2

Model and methods for a second-order transition

2.1 Three-dimensional Ising model

We have considered the simple cubic, ferromagnetic Ising model with nearest-neighbor interactions on $L \times L \times L$ lattices with periodic boundary conditions in zero magnetic field. Each of the lattice sites i has a spin, σ_i, which can take on the values $\sigma_i = +1$ for spin up and $\sigma_i = -1$ for spin down. The Hamiltonian is given by

$$\mathcal{H} = -J \sum_{\langle i,j \rangle} \sigma_i \sigma_j, \tag{2.1}$$

where $\langle i, j \rangle$ denotes distinct pairs of nearest-neighbor sites and $J > 0$ is the interaction constant. We also define the dimensionless energy E as

$$E = -\sum_{\langle i,j \rangle} \sigma_i \sigma_j. \tag{2.2}$$

In discussing the critical properties of the Ising model, it is easier to deal with the inverse temperature, so we define the dimensionless coupling constant $K = J/k_BT$ and use K for the discussion.

2.2 Related work and remaining questions for the 3D Ising model

The Ising Model [23] has long played an important role in the theory of phase transitions, and has served as a testing ground for new numerical and theoretical approaches. While the exact solution for the one-dimensional Ising model has been published in 1925 [23] and the two-dimensional Ising model has been solved in 1944 [24], the analytical solution for three dimensions is still a mystery. Nevertheless, Monte Carlo simulations [25], nonequilibrium relaxation Monte Carlo [26], Monte Carlo renormalization group [27,28], field-theoretic methods [29,30] and high-temperature series expansions [31] have provided precise information about the nature of the phase transition [32] by the end of the last century, although in some cases the results did not agree within the error bars.

Simulations were insufficient to validate Rosengren's "exact conjecture", which claimed that the critical temperature of the 3D simple cubic Ising model is given by $\tanh(J/k_BT_c) = (\sqrt{5}-2)\cos(\pi/8)$ [33]. In addition, Fisher pointed out that other "exact conjectures" gave quite similar numerical values [34]. Therefore, although precise values did exist for the 3D Ising critical temperature, there still remain unanswered questions. (For a rather complete review of results prior to 2002 see Ref. [32].)

Recent developments have reinvigorated interest in the critical behavior of the 3D Ising model. The conformal bootstrap method, using the constraints of crossing symmetry and unitarity in conformal field theories, has given unparalleled precision in the estimates for the critical exponent ν for the 3D Ising model [4, 35, 36]. New Monte Carlo simulations based

on non-perturbative approaches [37–39] and tensor renormalization group theory with high-order singularity value decomposition [40] also yielded very precise results. Although Zhang claimed to have solved the 3d Ising model exactly [41], Wu, McCoy, Fisher and Chayes [42–44] have given very convincing arguments that this "exact" solution is simply incorrect.

Many systems characterized by short-range interactions and a scalar order parameter (such as the unidirectional magnetization or the density) belong to the Ising universality class. This universality class comprises not only the anisotropic systems (e.g. a spin-$\frac{1}{2}$ Ising model with nearest neighbor interactions, a spin-1 model with nearest neighbor interactions), but also models for alloys, gas-liquid systems and liquid mixtures [45]. By examining the critical behavior of the 3D Ising model, it will provide a valuable benchmark for comparison with results for other models presumed to be in the Ising universality class.

2.3 Sampling methods

The Wolff cluster flipping algorithm [16] has been applied to sample the states on the simple cubic lattice, as it is more efficient than using the Metropolis algorithm [15] when the simulated temperature is very closed to the critical point (where there exists a critical slowing down). Clusters are grown and flipped sequentially, and they are generated by drawing bonds to all nearest neighbors of the growing cluster with probability

$$p = 1 - e^{-2K\delta_{\sigma_i\sigma_j}}. \tag{2.3}$$

To accelerate the Wolff algorithm, the energy and magnetization are calculated by only looking at the spins that actually get flipped in the process. Instead of flipping spins immediately, they were set to be zero temporarily and a list of those spins was maintained. By setting the spins in that cluster equal to zero we don't calculate the internal energy

of the cluster since the energy change only comes from the edges of the cluster. However, the change of the magnetization is related to the number of spins in the cluster. After the changes have been calculated, we go back and set all of the "zeroed" spins to their correct value (flipped from their original value). Thus, the energy and magnetization are calculated once, then the changes are added to them to get the updated values.

New random numbers were generated by using the Mersenne Twister generator [46]. We have implemented the Mersenne Twister algorithm with both 32-bit word length and 53-bit word length. No difference was detected under statistical error between data from both versions.

Simulations were performed at $K_0 = 0.221\,654$, which is an estimate for the critical inverse temperature K_c by MCRG analysis [28] and also used in an earlier, high resolution Monte Carlo study [25]. Lattices sizes studied were $L = 16$, 24, 32, 48, 64, 80, 96, 112, 128, 144, 160, 192, 256, 384, 512, 768, and 1024. For each system 2×10^5 Wolff steps were discarded for equilibrium before measurements were taken. Even for the largest lattice size, $L = 1024$, the energy had reached the equilibrium value by 130 000 cluster steps, and then the simulation was run another ten times the equilibrium relaxation time before the data accumulation began. For $L \leq 768$, we started from an ordered state and the relaxation to equilibrium was less than a thousand Wolff flips in all cases [47]. Our procedure insured that not only equilibrium had been reached but also the correlation with the initial states had been lost. For $L = 1024$, we started from a random state, but our procedure insured that the system had reached the equilibrium and that more than 10 times the equilibrium relaxation time had elapsed before collecting data measurements. From 6000 runs to 12 000 runs of 5×10^6 measurements for each lattice size were performed. In total, around 2×10^7 CPU core hours were used and more than 5TB data were generated by using 5 different Linux clusters. For the largest lattice, $L = 1024$, the average cluster size is around 1.1×10^6,

and the run length for a single run is around 4000 times the correlation time for the internal energy.

2.4 Quantities to be analyzed

In tradition, it has been difficult to estimate the critical exponent ν of the correlation length from Monte Carlo simulation data because few quantities are able to provide a direct measurement. Ferrenberg and Landau [25] showed that ν can be estimated more precisely if multiple quantities, including traditional quantities which have the same critical properties, are included. The logarithmic derivative of any power of the magnetization

$$\frac{\partial \ln \langle |m|^i \rangle}{\partial K} = \frac{1}{\langle |m|^i \rangle} \frac{\partial \langle |m|^i \rangle}{\partial K} = \frac{\langle |m|^i E \rangle}{\langle |m|^i \rangle} - \langle E \rangle, \tag{2.4}$$

which for $i = 1, 2, ...,$ can yield the ν estimate. In our analysis, we have considered the logarithmic derivatives of $\langle |m| \rangle$, $\langle |m|^2 \rangle$, $\langle |m|^3 \rangle$ and $\langle |m|^4 \rangle$. In addition, we also included the Binder's (reduced) magnetization cumulant U_{2i} [3] defined by

$$U_{2i} = 1 - \frac{\langle |m|^{2i} \rangle}{3 \langle |m|^i \rangle^2}, \quad i = 1, 2, 3, ... \tag{2.5}$$

whose derivative with respect to K is able to estimate ν as well. In our analysis, we have considered the second-order, fourth-order and sixth-order cumulants U_2, U_4 and U_6. For the fourth-order cumulant U_4, for instance, we have

$$\frac{\partial U_4}{\partial K} = -\frac{1}{3 \langle |m|^2 \rangle^2} (\langle m^4 E \rangle - \langle m^4 \rangle \langle E \rangle) + \frac{2 \langle m^4 E \rangle}{3 \langle |m|^2 \rangle^3} (\langle m^2 E \rangle - \langle m^2 \rangle \langle E \rangle). \tag{2.6}$$

The inverse critical temperature $K_c(L)$ can be estimated from the locations of the peaks in the above quantities as well as the specific heat,

$$C = K^2 L^{-d}(\langle E^2\rangle - \langle E\rangle^2), \tag{2.7}$$

the derivative of $|m|$ with respect to K,

$$\frac{\partial\langle|m|\rangle}{\partial K} = \langle|m|E\rangle - \langle|m|\rangle\langle E\rangle, \tag{2.8}$$

the finite-lattice susceptibility,

$$\chi' = KL^d(\langle|m|^2\rangle - \langle|m|\rangle^2), \tag{2.9}$$

and the zero of the fourth-order energy cumulant,

$$Q_4 = 1 - \frac{\langle(E - \langle E\rangle)^4\rangle}{3\langle(E - \langle E\rangle)^2\rangle^2}. \tag{2.10}$$

Note that in Eq. (2.9), it is the finite-lattice susceptibility, but not the "true" susceptibility calculated from the variance of m, $\chi = KL^d(\langle m^2\rangle - \langle m\rangle^2)$, which has no peak for finite L. (For sufficiently long runs, $\langle m\rangle = 0$ for zero magnetic field, so that any peak in χ is merely due to the finite statistics of the simulation.). All of the above quantities were calculated by using the GCC Quad-Precision Math Library which provides quadruple (128-bit) precision.

2.5 Finite-size scaling analysis

The critical behavior of a system in the thermodynamic limit at a second-order phase transition can be extracted from the size dependence of the singular part of the free energy density. This finite-size scaling theory was first developed by Fisher [11–13, 22].

According to finite-size scaling theory, (assume homogeneity and hyperscaling), and using L (linear dimension) and T (temperature) as variables, the free energy of a system is described by the following scaling ansatz,

$$F(L,T) = L^{-(2-\alpha)/\nu}\mathcal{F}(\varepsilon L^{1/\nu}, hL^{(\gamma+\beta)/\nu}), \tag{2.11}$$

where $\varepsilon = (T-T_c)/T_c$ (T_c is the critical temperature for the infinite-lattice), h is the magnetic field, the critical exponents α, β, γ and ν are the infinite lattice values, and $\mathcal{F}$ is the scaling function. The choice of the scaling variable $x = \varepsilon L^{1/\nu}$ is motivated by the observation that the correlation length, which diverges as $\varepsilon^{-\nu}$ as the transition is approached, is limited by the lattice size L. Various thermodynamic properties can be determined from Eq. (2.11) and have corresponding scaling forms, e.g.,

$$m = L^{-\beta/\nu}\mathcal{M}^0(\varepsilon L^{1/\nu}), \tag{2.12}$$

$$\chi = L^{\gamma/\nu}\chi^0(\varepsilon L^{1/\nu}) + b_\chi, \tag{2.13}$$

$$C = L^{\alpha/\nu}\mathcal{C}^0(\varepsilon L^{1/\nu}) + b_C, \tag{2.14}$$

where $\mathcal{M}^0(x)$, $\chi^0(x)$ and $\mathcal{C}^0(x)$ are scaling functions, and b_χ, b_C are analytic background terms. x is the only relevant thermodynamic variable, as we are interested in zero-field properties ($h = 0$).

A number of different practical implementations based on finite size scaling (FSS) schemes have been derived and successfully applied to the analysis of the critical phenomena [25, 32, 37]. In the following analysis, we determine the effective transition temperature very precisely based on the location of peaks in multiple thermodynamic quantities as discussed in Sec. 2.4.

For example, as for a finite lattice, the peak of the specific heat C occurs at the temperature where the scaling function $\mathcal{C}^0$ is maximum, i.e., when

$$\left.\frac{\partial \mathcal{C}^0(x)}{\partial x}\right|_{x=x^*} = 0. \tag{2.15}$$

The temperature where the peak is located is the finite-lattice (effective) "transition" temperature $T_c(L)$, on the condition $x = x^*$ which varies with L asymptotically as

$$T_c(L) = T_c + T_c x^* L^{-1/\nu}. \tag{2.16}$$

The FSS ansatz is valid only for sufficiently large lattice size L and T sufficiently close to T_c. Corrections to scaling and finite-size scaling appear for smaller systems and temperatures away from T_c must be taken into account. There are two kinds of correction terms, one is due to the irrelevant scaling fields which can be expressed in terms of an exponent θ, e.g. $a_1\varepsilon^\theta + a_2\varepsilon^{2\theta} + \cdots$, while the other is due to the non-linear scaling fields, e.g. $b_1\varepsilon^1 + b_2\varepsilon^2 + \cdots$. The temperatures that we consider in our analysis differ from T_c (or $\varepsilon = 0$) by amounts proportional to $L^{-1/\nu}$ (Eq. (2.16)), so that the correction terms can be expressed by the power-law $a_1 L^{-\theta/\nu} + a_2 L^{-2\theta/\nu}$ and $b_1 L^{-1/\nu} + b_2 L^{-2/\nu}$.

By including correction terms, the estimate for $T_c(L)$ can be expressed to be

$$\begin{aligned} T_c(L) = T_c + A'_0 L^{-1/\nu}(1 + A'_1 L^{-\omega_1} + A'_2 L^{-2\omega_1} + \cdots \\ + B'_1 L^{-\omega_2} + B'_2 L^{-2\omega_2} + \cdots + C'_1 L^{-(\omega_1+\omega_2)} + \cdots \\ + D'_1 L^{-\omega_\nu} + D'_2 L^{-2\omega_\nu} + \cdots + E'_1 L^{-\omega_{NR}} + \cdots), \end{aligned} \tag{2.17}$$

where ω_i $(i = 1, 2, ...)$ are the correction exponents, $\omega_\nu = 1/\nu$ is the correction exponent corresponding to the non-linear scaling fields [48], and ω_{NR} is the correction exponent due to the breaking of the rotational invariance of the lattice [49]. As we have defined the coupling

as $K = J/k_BT$, $K_c(L)$ can be expressed as

$$\begin{aligned} K_c(L) = K_c + A_0 L^{-1/\nu}(1 + A_1 L^{-\omega_1} + A_2 L^{-2\omega_1} + \cdots \\ + B_1 L^{-\omega_2} + B_2 L^{-2\omega_2} + \cdots + C_1 L^{-(\omega_1+\omega_2)} + \cdots \\ + D_1 L^{-\omega_\nu} + D_2 L^{-2\omega_\nu} + \cdots + E_1 L^{-\omega_{NR}} + \cdots), \end{aligned} \tag{2.18}$$

We first estimate the critical exponent ν using the quantities discussed in Sec. 2.4. And then insert it into Eq. (2.18), so that there is one less unknown parameter to do the non-linear fit to Eq. (2.18). To do this, we can use the critical scaling form without the prior knowledge of the transition coupling K_c

$$\begin{aligned} \left.\frac{\partial U_{2i}}{\partial K}\right|_{\max} = U_{i,0} L^{1/\nu}(1 + a_1 L^{-\omega_1} + a_2 L^{-2\omega_1} + \cdots \\ + b_1 L^{-\omega_2} + b_2 L^{-2\omega_2} + \cdots + c_1 L^{-(\omega_1+\omega_2)} + \cdots \\ + d_1 L^{-\omega_\nu} + d_2 L^{-2\omega_\nu} + \cdots + e_1 L^{-\omega_{NR}} + \cdots), \end{aligned} \tag{2.19}$$

$$\begin{aligned} \left.\frac{\partial \ln \langle |m|^i \rangle}{\partial K}\right|_{\max} = D_{i,0} L^{1/\nu}(1 + a_1 L^{-\omega_1} + a_2 L^{-2\omega_1} + \cdots \\ + b_1 L^{-\omega_2} + b_2 L^{-2\omega_2} + \cdots + c_1 L^{-(\omega_1+\omega_2)} + \cdots \\ + d_1 L^{-\omega_\nu} + d_2 L^{-2\omega_\nu} + \cdots + e_1 L^{-\omega_{NR}} + \cdots), \end{aligned} \tag{2.20}$$

Once ν is determined from the fit of Eq. (2.19) and Eq. (2.20), we can estimate the critical inverse temperature K_c with a fixed value of ν.

In addition, the inverse transition temperature can also be determined by the Binder's fourth-order cumulant crossing technique [3]. As the lattice size $L \to \infty$, the fourth-order magnetization cumulant $U_4 \to 0$ for $K < K_c$ and $U_4 \to 2/3$ for $K > K_c$. For large enough

lattice sizes, curves for U_4 cross as a function of inverse temperature at a "fixed point" U^*, and the location of the crossing "fixed point" is K_c. U_4 can be plotted as a function of K for different lattice sizes, and the location of the intersections between curves for the two lattice sizes is given by

$$K_{\rm cross}(L,b) = K_c + a_1 L^{-1/\nu-\omega_1}\left(\frac{b^{-\omega_1}-1}{b^{1/\nu}-1}\right) + a_2 L^{-1/\nu-\omega_2}\left(\frac{b^{-\omega_2}-1}{b^{1/\nu}-1}\right) + \cdots , \qquad (2.21)$$

where L is the size of the smaller lattice, $b = L'/L$ is the ratio of two lattice sizes, and ω_1, ω_2 are correction exponents in the finite-size scaling formulation.

2.6 Data analysis methods

2.6.1 Histogram reweighting

One limitation on the resolution of Monte Carlo simulations near phase transition is that it needs to perform a large number of runs at different temperature to precisely locate the peaks in response functions. Using histograms we can extract more information from a single Monte Carlo simulation [18,19], because samples taken from a known probability distribution can be translated into samples from another distribution over the same state space.

First, an importance sampling Monte Carlo simulation is carried out at the inverse temperature K_0, which generates configurations with a probability proportional to the Boltzmann weight, $\exp(-K_0 E)$. The probability of simultaneously observing the system with total (dimensionless) energy E and total magnetization M is,

$$P_{K_0}(E,M) = \frac{1}{Z(K_0)} W(E,M)\exp(-K_0 E), \qquad (2.22)$$

where $Z(K_0)$ is the partition function, and $W(E, M)$ is the number of configurations with energy E and magnetization M.

Then, a histogram $H_0(E, M)$ of the energy and the magnetization at K_0 is constructed, which can provide an estimate for the equilibrium probability distribution. It becomes exact in the limit of an infinite-length run. Thus,

$$H_0(E, M) = \frac{N}{Z(K_0)} \tilde{W}(E, M) \exp(-K_0 E), \tag{2.23}$$

where $\tilde{W}(E, M)$ is an estimate for the true density of states $W(E, M)$ and N is the number of measurements made. For an infinite-length run, we can replace $W(E, M)$ with $\tilde{W}(E, M)$, which will yield the relationship between the histogram measured at $K = K_0$ and the (estimated) probability distribution for arbitrary (neighboring) K,

$$P_K(E, M) = \frac{H_0(E, M) e^{\Delta K E}}{\sum H(E, M) e^{\Delta K E}}, \tag{2.24}$$

where $\Delta K = K_0 - K$. Based on $P_K(E, M)$, the average value of any function $f(E, M)$ of E and M at the coupling K, can be calculated,

$$\langle f(E, M) \rangle_K = \sum_{E,M} f(E, M) P_K(E, M). \tag{2.25}$$

As K can be varied continuously, the histogram method is able to locate the peaks for different thermodynamic derivatives precisely (e.g. applying the golden-section search method [50]) in a certain reliable range. In this way, the critical behavior can be studied with high resolution by using Monte Carlo.

2.6.2 Jackknife method with cross correlations

Ideally, in a Monte Carlo simulation, the current configuration only depends on the previous configuration (Markov chain). But in practice, it is also likely to be correlated to the earlier configurations. Generally, the farther away two configurations are, the less correlation. Because of the memory of Markov chain, neighboring measurements in the time-series are correlated, such that the fluctuations look to be smaller than they should be. To deal with this issue, we can consider blocks of original data, and use jackknife resampling [51].

An important advance by Weigel and Janke [20, 21] was the innovative observation that the cross correlation between different quantities could lead to systematic bias in the estimates of critical quantities extracted from the data (in the same data pool originally).

As for a set (sample) of n measurements of a random variable $\mathbf{x} = (x_1, x_2, \cdots, x_n)$, and an estimator $\hat{\theta} = f(\mathbf{x})$. We wish to estimate the value and error of $\hat{\theta}$. The jackknife focuses on the samples that leave out one measurement at a time. We define the jackknife average, x_i^J, by,

$$x_i^J = \frac{1}{n-1} \sum_{j \neq i} x_j, \tag{2.26}$$

where $i = 1, 2, \cdots, n$, so x_i^J is the average of all the x values except x_i. Similarly, we define

$$\hat{\theta}_i^J = f(x_i^J). \tag{2.27}$$

We state that, the jackknife estimate of $\hat{\theta} = f(\mathbf{x})$ is the average of $\hat{\theta}_i^J$, i.e.

$$\bar{\theta} = \frac{1}{n} \sum_{i=1}^{n} \hat{\theta}_i^J = \frac{1}{n} \sum_{i=1}^{n} f(x_i^J), \tag{2.28}$$

and the jackknife error $\sigma(\hat{\theta})$, is given by,

$$\sigma(\hat{\theta}) = \left[\frac{n-1}{n}\sum_{i=1}^{n}(\hat{\theta}_i^J - \bar{\theta})^2\right]^{1/2}. \tag{2.29}$$

In Eq. (2.28) and Eq. (2.29), each data block has only one element. More generally, there can exist multiple adjacent elements in each block. For example, we can have n data blocks, where each block has $N_b = N/n$ adjacent elements (N is the total number of measurements in the time series).

If attempting to extract the parameter $\hat{\theta}$ based on multiple estimates $\hat{\theta}^{(k)}(k = 1, 2, 3\cdots)$ from the same original time-series data, there will be significant cross correlation between estimates $\hat{\theta}^{(k)}$ and $\hat{\theta}^{(l)}$. For instance, we can determine a number of estimates for ν from different approaches (more discussion will be at Sec. 3.1). Let's denote them to be $\nu^{(k)}(k = 1, 2, 3\cdots)$. Although different $\nu^{(k)}$ are determined by different quantities, they are from the same original dataset, since quantities are calculated based on the same configurations of the system.

To reduce the cross correlation effectively, we can consider the jackknife covariance matrix $\mathbf{G}$ [51]. For a number of estimates $\hat{\theta}^{(k)}$, the r^{th} row, c^{th} column entry of matrix $\mathbf{G}$ is given by,

$$\mathbf{G}_{rc}(\hat{\theta}) = \frac{n-1}{n}\sum_{i=1}^{n}(\hat{\theta}_i^{J,(r)} - \bar{\theta}^{(r)})(\hat{\theta}_i^{J,(c)} - \bar{\theta}^{(c)}). \tag{2.30}$$

The m different estimates $\hat{\theta}^{(k)}(k = 1, 2, \cdots, m)$ for the same parameter $\hat{\theta}$, should have the same expectation. Therefore, the estimated value for $\hat{\theta}$ can be determined by a linear combination,

$$\bar{\theta} = \sum_{k=1}^{m}\alpha_k\hat{\theta}^{(k)}. \tag{2.31}$$

where $\sum_k \alpha_k = 1$. Based on the cross correlation analysis from Refs. [20, 21], a Lagrange multiplier would be introduced, where the constraint $\sum_k \alpha_k = 1$ is enforced to minimize the

variance,

$$\sigma^2(\hat{\theta}) = \sum_{k=1}^{m}\sum_{l=1}^{m}\alpha_k\alpha_l(\langle\hat{\theta}^{(k)}\hat{\theta}^{(l)}\rangle - \langle\hat{\theta}^{(k)}\rangle\langle\hat{\theta}^{(l)}\rangle). \tag{2.32}$$

The optimal choice for the weights is as follows,

$$\alpha_k = \frac{\sum_{l=1}^{m}[\mathbf{G}(\hat{\theta})^{-1}]_{kl}}{\sum_{k=1}^{m}\sum_{l=1}^{m}[\mathbf{G}(\hat{\theta})^{-1}]_{kl}}, \tag{2.33}$$

where $\mathbf{G}(\hat{\theta})^{-1}$ is the inverse of the covariance matrix. The weights are bounded to be $0 \leq \alpha_k \leq 1$ traditionally. However, the optimal choices given in Eq. (2.33) are the more general unbounded weights, which can be negative. The negative weights may lead to the average lying outside the range of individual estimates, where individual variances are connected due to cross correlations. Thus, they can help alleviate the effect of cross correlations.

Based on the optimal choice for the weights, the variance can be expressed by,

$$\sigma^2(\hat{\theta}) = \frac{1}{\sum_{k=1}^{m}\sum_{l=1}^{m}[\mathbf{G}(\hat{\theta})^{-1}]_{kl}}. \tag{2.34}$$

2.7 Testing methodology and quality control

At such a level of resolution of this study, the finite precision of the pseudo-random number generator and the restriction of a variable stored in the memory are some new challenges. In the Wolff algorithm, the probability of adding a spin to the cluster is related to K by

$$p = 1 - e^{-2K\delta_{\sigma_i\sigma_j}}.$$

At the desired simulated coupling $K_0 = 0.221\,654$, when this probability is converted to a 32-bit unsigned number for comparison with pseudo-random numbers generated in the simulation, it will be truncated from 1537987121.70821 to 1537987121 due to the finite

precision. When such number is reconverted back into a value of K, the result differs from 0.221 654 in the 10th decimal place. For the largest system sizes, $L = 1024$, this is only a factor of 20 smaller than the statistical error. By performing simulations with a 53-bit pseudo-random number generator we have verified that this is not significant for the current analysis, but for future studies of larger systems and/or higher precision, a 32-bit random number generator would not suffice. For the data analysis we used the corrected effective K_0 instead of 0.221 654 and for $L = 1024$ we used the multiple-histogram method [19] to combine results for the 32- and 53-bit pseudorandom number generators.

To estimate the critical quantities (e.g. ν and K_c) by using the finite-size scaling analysis with high precision, it is necessary to look for the peak values of derivatives of the thermodynamic quantities and their corresponding locations with very high resolution. Double precision may not be enough to fulfill the task, since the imprecision will accumulate during calculation. So the quadruple precision arithmetic has been used in the data analysis (GCC Quad-Precision Math Library).

In addition, both the Wolff cluster flipping algorithm and the Metropolis single spin-flip algorithm have been implemented to simulate the 32^3 systems. For each algorithm, a total of 3×10^{10} measurements were taken. The Wolff cluster simulation for $L = 32$ was also performed with the *MRG32K3A* random number generator from Pierre L'Ecuyer, "Combined Multiple Recursive Random Number Generators", Operations Research, 47, 1 (1999), 159-164. (We used the implementation by Guskova, Barash and Shchur in their *rngavxlib* random number library [52].) The values of the maxima and the corresponding locations in all quantities agree, to within the error bars, with those from the Metropolis simulations and the Wolff simulations by using the Mersenne twister. Also, the t-test comparisons yielded no p-values less than 0.2. Thus, the problems found by Ferrenberg et al. [53] using other random number generators were not noticeable here.

Chapter 3

Results: critical behavior in the simple cubic Ising model

3.1 Critical exponent of the correlation length ν and the critical coupling K_c

3.1.1 Finite-size scaling analysis to determine ν

First, we performed an analysis with only one correction term,

$$X_{\max} = X_0 L^{1/\nu}(1 + a_1 L^{-\omega_1}), \tag{3.1}$$

where X is the quantity we have used to estimate the critical exponent ν: the logarithmic derivatives $\partial \ln \langle |m|^i \rangle / \partial K$ for $i = 1, 2, 3, 4$; the magnetization cumulant derivatives $\partial U_{2i}/\partial K$ for $i = 1, 2, 3$. Least-squares fits have been performed for Eq. (3.1). χ^2 per degree of freedom (dof) is used as the quality of the fit, and ideally it is approximately 1 (with values too large

Table 3.1: Results for the critical exponent ν with Eq. (3.1) when only considering one correction term as a function of $L_{\min}$, where $L_{\min}$ is the minimal lattice size that is included into the fit.

$L_{\min}$	ν
16	0.629 756(32)
24	0.629 765(42)
32	0.629 749(48)
48	0.630 05(13)
64	0.629 83(13)
80	0.629 80(14)
96	0.629 72(12)
112	0.629 61(10)
128	0.629 56(11)
144	0.629 63(14)
160	0.629 554(95)

indicating a poor quality of fit while values too small indicating that the error is too large). In our analysis, the χ^2 per dof is between 0.50 to 1.73 which is a reasonable range.

By calculating the covariance matrix and doing the cross-correlation analysis, we give estimates for ν in Table 3.1, where the minimum lattice size included in the analysis, $L_{\min}$, is eliminated one by one.

In Fig. 3.1, we see that the estimated value for the critical exponent ν seems to be stable for small values of $L_{\min}$ ($L_{\min}$ = 16, 24, 32). And there is a sudden jump from $L_{\min}$ = 32 to $L_{\min}$ = 48. Finally, ν value tends to be stable at the large lattices ($L_{\min} \geq 112$), around 0.629 60.

The finite-size effect is strong for small lattice sizes. We observe that there is a systematic decrease in the value of ν as $L_{\min}$ increases. Thus, only considering one correction term is insufficient. But the first three values for ν seem to be abnormal. This is because a single correction term attempts to account for all finite-size effects with estimates for different sizes

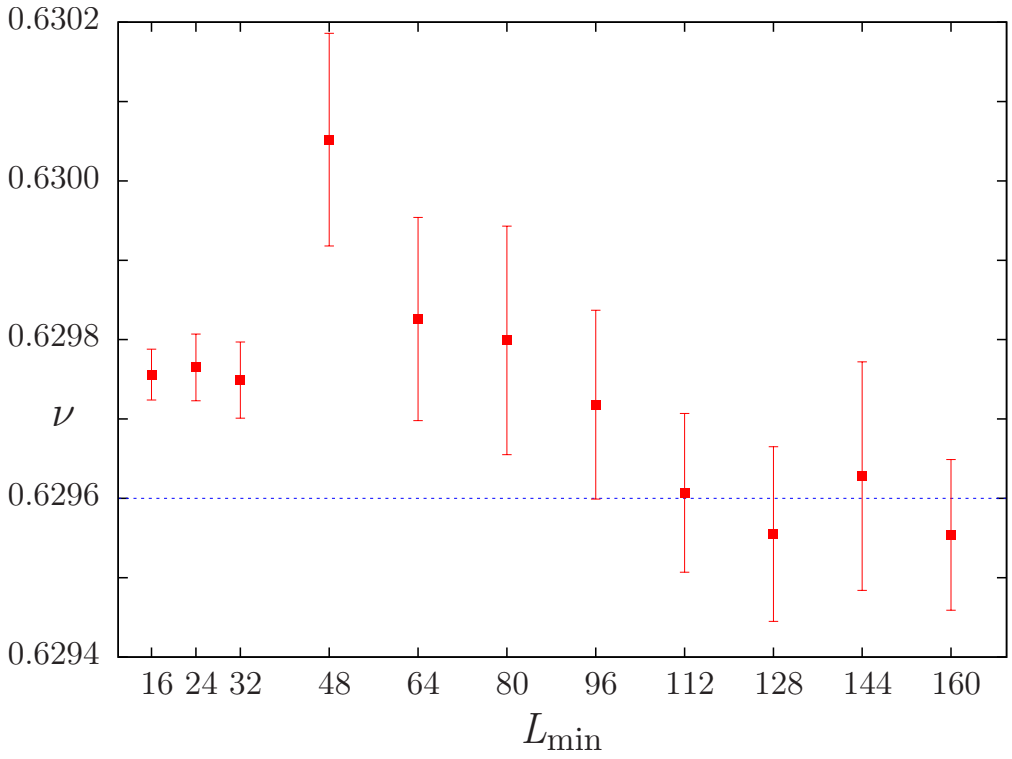

Figure 3.1: Results for the critical exponent ν when only considering one correction term as a function of $L_{\min}$, where $L_{\min}$ is the minimal lattice size that is included into the fit.

having different uncertainties. Therefore, the value of the correction exponent from such fits differs from the theoretical prediction (0.8303(18)) [4]. Including small lattices, the estimate for the correction exponent ω is larger than 0.8303 and the resulting estimate for ν is smaller than it should be. ν seems to be stable at around 0.629 75 when $L_{\min} \leq 32$. However, all fitting (unknown) parameters would vary altogether in order to minimize the least squares in a high-dimension loss function space. Since a single correction term contributes differently for different system sizes, it would result in inconsistent estimates for ν and ω. In consequence, more correction terms need to be taken into account for a high precision analysis.

Because of the lack of a sufficient number of degrees of freedom, it is difficult to include two or more unknown correction exponents as fitting parameters. However, the conformal

bootstrap [4, 35], gives a theoretical prediction for the confluent correction exponents,

$$\omega_1 = 0.8303(18), \quad \omega_2 \approx 4. \tag{3.2}$$

In correction term corresponding to the non-linear scaling fields [48],

$$\omega_\nu = 1/\nu. \tag{3.3}$$

Also, a correction term due to the breaking of the rotational invariance of the lattice [49] may play a role,

$$\omega_{NR} = 2.0208(12). \tag{3.4}$$

In our analysis, any types of correction terms in Eq. (2.19) and Eq. (2.20) are permitted to contribute an amount of correction, such that it is statistically significant. But due to the finite precision of our estimates for thermodynamic quantities and the limited number of system sizes in the analysis we found that including more than three correction terms did not lead to meaningful fits. Consistent estimates for the asymptotic values of the critical exponent ν have been yielded by performing least squares fits with 7 different combinations of three correction terms. We have found that the best fit was obtained by using $\omega_1 = 0.83$, $\omega_2 = 4$ and $\omega_\nu = 1.6$. We will now show these results in detail.

For the reasons stated above, the fitting model for the peak value of quantity X is,

$$X_{\max} = X_0 L^{1/\nu}(1 + a_1 L^{-\omega_1} + a_2 L^{-\omega_2} + a_3 L^{-\omega_\nu}). \tag{3.5}$$

We have analyzed the data fitting model Eq. (3.5) for three cases: using one fixed correction exponent $\omega_1 = 0.83$; two fixed exponents $\omega_1 = 0.83$, $\omega_2 = 4$; and three fixed exponents $\omega_1 = 0.83$, $\omega_2 = 4$, $\omega_\nu = 1.6$, respectively. The results for ν are shown in Table 3.2.

Table 3.2: Estimates for ν with: one fixed correction exponent $\omega_1 = 0.83$, two fixed exponents $\omega_1 = 0.83$, $\omega_2 = 4$, and three fixed exponents $\omega_1 = 0.83$, $\omega_2 = 4$, $\omega_3 = 1.6$ as a function of $L_{\min}$.

$L_{\min}$	$\nu(\omega_1$ fixed)	$\nu(\omega_{1,2}$ fixed)	$\nu(\omega_{1,2,3}$ fixed)
16	0.631 814(18)	0.630 806(30)	0.630 072(45)
24	0.631 046(26)	0.630 513(40)	0.630 049(57)
32	0.630 722(33)	0.630 241(55)	0.629 980(77)
48	0.630 350(48)	0.630 278(78)	0.629 99(11)
64	0.630 319(62)	0.630 21(11)	0.630 06(15)
80	0.630 285(78)	0.630 10(15)	0.629 93(21)
96	0.630 25(10)	0.629 93(18)	0.629 90(29)
112	0.630 14(13)	0.630 01(17)	0.629 93(18)
128	0.630 04(15)	0.630 04(15)	0.629 84(22)
144	0.629 85(18)	0.629 85(18)	0.629 96(26)

By looking at Fig. 3.2, we observe that, with only one fixed confluent correction exponent ($\omega_1 = 0.83$) being considered, the estimated value for the critical exponent ν decreases systematically up to $L_{\min} = 128$. After that, the ν value seems to converge. Also, χ^2 per dof is very high when $L_{\min}$ is small, which indicates that only considering one correction term into the fit is inadequate, especially for the small lattice sizes ($L_{\min} = 16$, 24, 32). When considering two fixed confluent correction exponents ($\omega_1 = 0.83$, $\omega_2 = 4$), ν decreases as $L_{\min}$ increases for $L_{\min} \leq 96$. The ν value appears to be statistically fluctuating when $L_{\min} \geq 96$. Still, χ^2 per dof is high when $L_{\min}$ is small, which means that two correction terms are still not enough for small lattice sizes ($L_{\min} = 16$, 24) within our resolution. Compared with the analysis with only one fixed correction exponent, the estimated values for ν are highly consistent when $L_{\min} \geq 128$. This is because when $L_{\min}$ becomes large enough, the second confluent correction term contributes little.

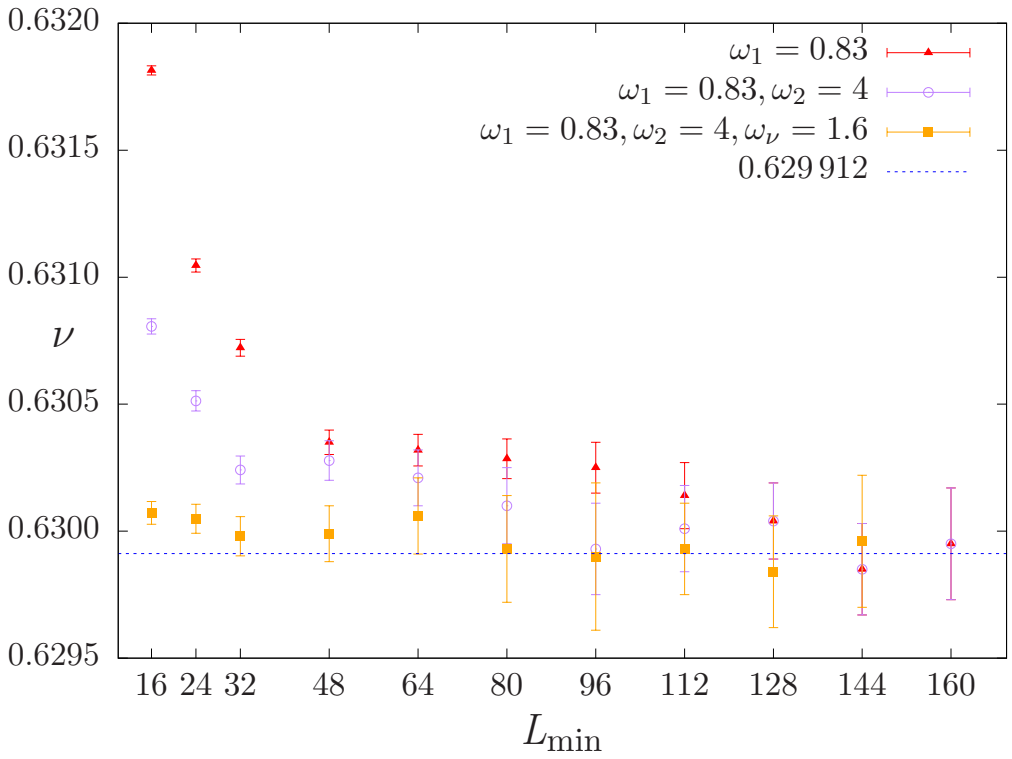

Figure 3.2: Results for the critical exponent ν when considering one fixed correction exponent $\omega_1 = 0.83$, two fixed exponents $\omega_1 = 0.83$, $\omega_2 = 4$, and three fixed exponents $\omega_1 = 0.83$, $\omega_2 = 4$, $\omega_\nu = 1.6$ as a function of $L_{\min}$.

With three correction exponents, two for confluent corrections ($\omega_1 = 0.83$, $\omega_2 = 4$) and one for the non-linear scaling fields ($\omega_\nu = 1.6$), the estimate for the critical exponent ν shows statistical fluctuation. The values for χ^2 per dof for each quantity is reasonable (between 0.53 to 1.78). But, all estimates for the critical exponent $\nu > 0.629\,97$ if $L_{\min} < 80$, while $\nu < 0.629\,97$ if $L_{\min} \geq 80$. It looks like that there is still a very small systematic decrease of ν as $L_{\min}$ increases, which indicates that three correction terms may not be adequate to account for all finite-size effects for small lattice sizes ($L \leq 80$) with such precision. Therefore, the value for ν is estimated by taking the average of ν obtained from different fits for different $L_{\min}$ varying from 80 to 144, $\nu = 0.629\,912$. To estimate the error of ν, we used the jackknife method on estimates of ν from three correction term analysis using different ranges of $L_{\min}$:

Table 3.3: Results for the critical exponent ν from jackknife analysis on estimates for ν that are from the three correction terms analysis for values of $L_{\min}$ within the ranges shown (with Eq. (3.5)).

$L_{\min}$	ν
16-144	0.629 97(21)
24-144	0.629 96(19)
32-144	0.629 95(16)
48-144	0.629 94(16)
64-144	0.629 94(15)
80-144	0.629 912(86)
96-144	0.629 908(81)

consider estimates for ν from $L_{\min} = 96$ to 144, then do a jackknife analysis to estimate the value and error of ν. Add one ν value corresponding to $L_{\min} = 80$, then do a jackknife analysis from $L_{\min} = 80$ to 144. Do this one by one, up to the analysis from $L_{\min} = 16$ to 144. Results are shown in Table 3.3.

Based on the values of $L_{\min}$ to estimate the value of ν (from 80 to 144), we find

$$\nu = 0.629\,912(86). \tag{3.6}$$

3.1.2 Finite-size scaling analysis to determine K_c

To estimate the critical coupling K_c, we have considered the location of zero of the fourth-order energy cumulant Q_4 and the peak location of following quantities:

- the logarithmic derivatives, $\partial \ln \langle |m|^i \rangle / \partial K$ for $i = 1, 2, 3, 4$;
- the magnetization cumulant derivatives, $\partial U_{2i} / \partial K$ for $i = 1, 2, 3$;
- the specific heat, C;
- the derivative of the modulus of the magnetization, $\partial \langle |m| \rangle / \partial K$;

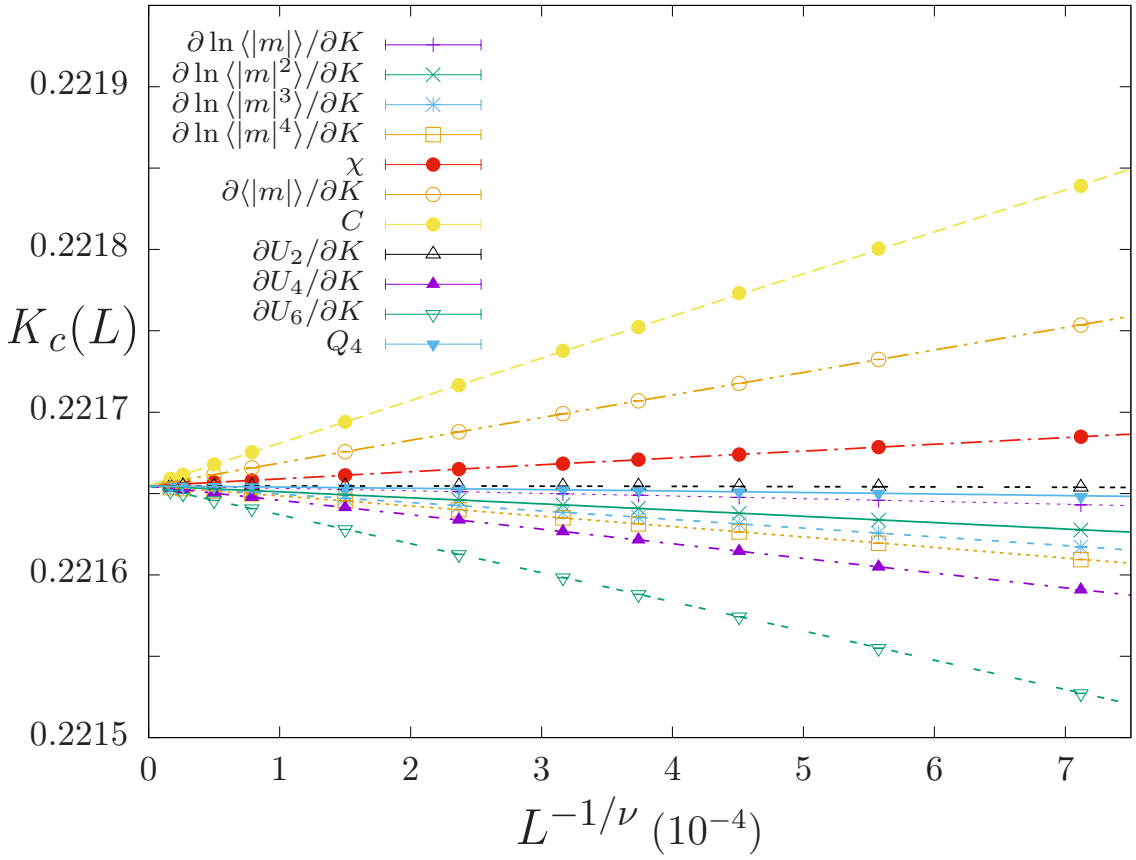

Figure 3.3: Size dependence of the finite-lattice effective critical temperatures estimated from $L = 96$ to 1024. (Error bars are smaller than the size of the mark for every system size.)

- the finite-lattice susceptibility, χ'.

Fig. 3.3 shows the finite-lattice effective critical temperatures estimated from $L = 96$ to 1024 as a function of lattice size. Error bars are smaller than the size of the mark for every system size.

First, an analysis with one correction term was performed to estimate the critical coupling K_c,

$$K_c(L) = K_c + A_0 L^{-1/\nu}(1 + A_1 L^{-\omega_1}), \tag{3.7}$$

Table 3.4: Results for the critical coupling K_c when only considering one correction term as a function of $L_{\min}$ with Eq. (3.7).

L_{min}	K_c
16	0.221 654 621 8(13)
24	0.221 654 623 9(16)
32	0.221 654 624 9(19)
48	0.221 654 623 4(27)
64	0.221 654 625 3(45)
80	0.221 654 626 1(62)
96	0.221 654 630 0(78)
112	0.221 654 630 2(69)
128	0.221 654 630 2(63)
144	0.221 654 628(13)
160	0.221 654 630 3(85)

where the critical exponent was fixed to be $\nu = 0.629\,912$, and the correction exponent ω_1 is a fitting parameter (unfixed). The χ^2 per degree of freedom is acceptable, except in the situation where $L_{\min} = 16$ for $\partial\langle|m|\rangle/\partial K$, the χ^2 pof is high (2.76).

By calculating the covariance matrix and doing the cross correlation analysis, K_c was estimated as shown in Table 3.4. The minimum lattice size $L_{\min}$ that is taken into account is eliminated one by one.

In Fig. 3.4, we observe that, the estimated value for the critical coupling K_c appears to be stable if $L_{min} \geq 96$, around 0.221 654 630.

With the help of the theoretical prediction, we have considered one fixed correction exponent $\omega_1 = 0.83$, two fixed exponents $\omega_1 = 0.83$, $\omega_2 = 4$, and three fixed exponents $\omega_1 = 0.83$, $\omega_2 = 4$, $\omega_\nu = 1.6$, to the fitting model Eq. (3.8)

$$K_c(L) = K_c + A_0 L^{-1/\nu}(1 + A_1 L^{-\omega_1} + A_2 L^{-\omega_2} + A_3 L^{-\omega_\nu}). \tag{3.8}$$

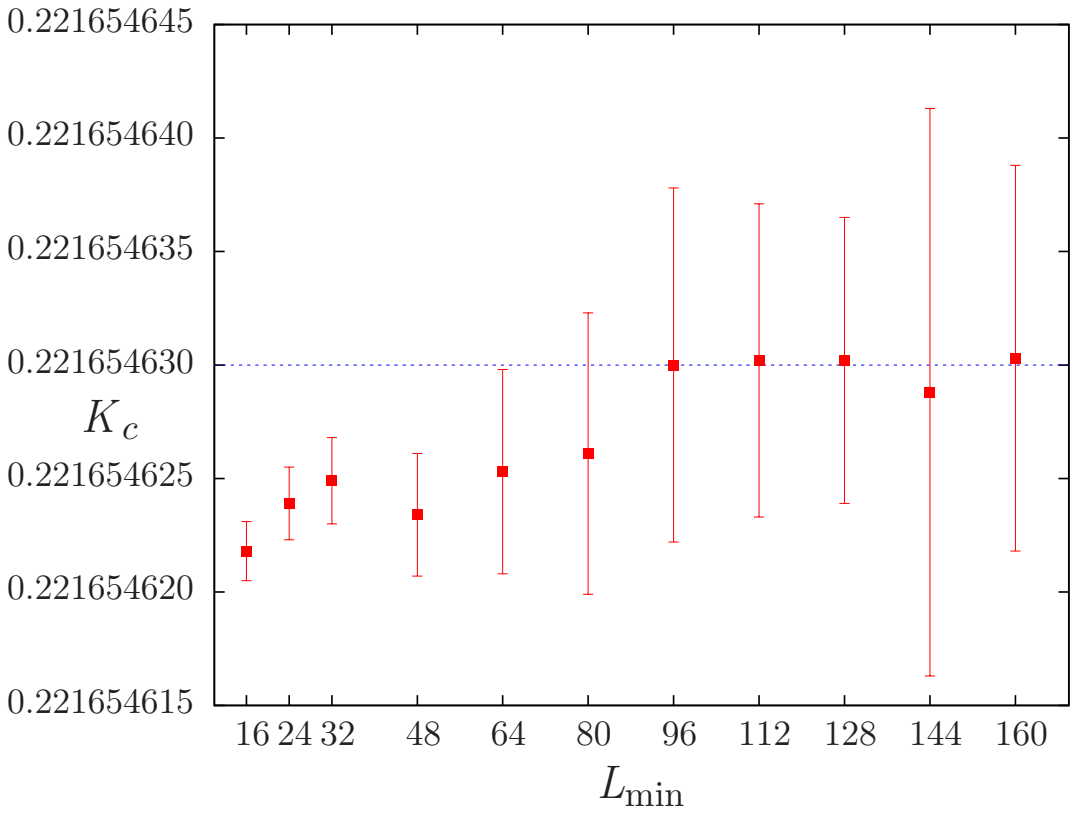

Figure 3.4: Results for the critical coupling K_c with only one correction term included in the fitting as a function of $L_{\min}$.

(Similar to the analysis to determine ν, seven different combinations of the three correction terms have been analysed and the results were rather insensitive to the choice of the model on the estimate for K_c. The best fit was obtained by using $\omega_1 = 0.83$, $\omega_2 = 4$ and $\omega_\nu = 1.6$.) The results for K_c are shown in Table 3.5.

In Fig. 3.5, when only one fixed confluent correction exponent ($\omega_1 = 0.83$) is included, there is a systematic decrease for the estimated value for the critical coupling K_c if $L_{\min} \leq 80$. The K_c value appears to be stable if $L_{\min} \geq 80$. The value for the χ^2 per dof is very high when $L_{\min}$ is small, which indicates that the quality of the fit is not good with one correction term when the lattice size is small ($L_{\min} = 16$, 24, 32). When considering two

Table 3.5: Fitted values for K_c with: (left column) one correction term (fixed exponent $\omega_1 = 0.83$); (center column) two correction terms (fixed exponents $\omega_1 = 0.83$, $\omega_2 = 4$; and (right column) three correction terms (fixed exponents $\omega_1 = 0.83$, $\omega_2 = 4$, $\omega_3 = 1.6$) as a function of $L_{\min}$.

$L_{\min}$	$K_c(\omega_1$ fixed)	$K_c(\omega_{1,2}$ fixed)	$K_c(\omega_{1,2,3}$ fixed)
16	0.221 654 656 2(10)	0.221 654 639 3(11)	0.221 654 625 7(21)
24	0.221 654 638 8(11)	0.221 654 630 8(12)	0.221 654 625 7(24)
32	0.221 654 634 3(11)	0.221 654 630 7(12)	0.221 654 625 3(32)
48	0.221 654 630 7(12)	0.221 654 630 5(12)	0.221 654 623 2(30)
64	0.221 654 628 4(13)	0.221 654 628 4(13)	0.221 654 623 4(60)
80	0.221 654 627 5(14)	0.221 654 627 5(15)	0.221 654 625 0(75)
96	0.221 654 626 0(17)	0.221 654 626 0(16)	0.221 654 627 9(97)
112	0.221 654 625 9(18)	0.221 654 626 0(18)	0.221 654 625 0(49)
128	0.221 654 625 8(21)	0.221 654 625 8(21)	0.221 654 626 3(48)
144	0.221 654 627 0(25)	0.221 654 627 0(25)	0.221 654 627 1(34)

fixed confluent correction exponents ($\omega_1 = 0.83$, $\omega_2 = 4$), the K_c value decreases as $L_{\min}$ increases if $L_{\min} = 80$. After that, the K_c value appears to be statistically fluctuating. Still, χ^2 per dof is high when $L_{\min}$ is small, which means that two correction terms are not enough for small lattice sizes ($L_{\min} = 16$, 24) to account for the finite-size effects. Also, the estimates for K_c with one and with two fixed correction exponents are highly consistent when $L_{\min} \geq 64$. This is because the second confluent correction term contributes little when $L_{\min}$ becomes large enough. Thus, these two analyses tend to generate similar results.

In addition, when three correction exponents are included in the analysis, two for confluent corrections ($\omega_1 = 0.83$, $\omega_2 = 4$) and one for non-linear scaling fields ($\omega_\nu = 1.6$), the χ^2 per dof for each quantity is decent except the following cases:

- χ^2 per dof = 2.52, if $L_{\min} = 144$ for $\partial \ln \langle |m| \rangle / \partial K$,
- χ^2 per dof = 2.41, if $L_{\min} = 144$ for $\partial \ln \langle |m|^2 \rangle / \partial K$,
- χ^2 per dof = 2.34, if $L_{\min} = 144$ for χ',

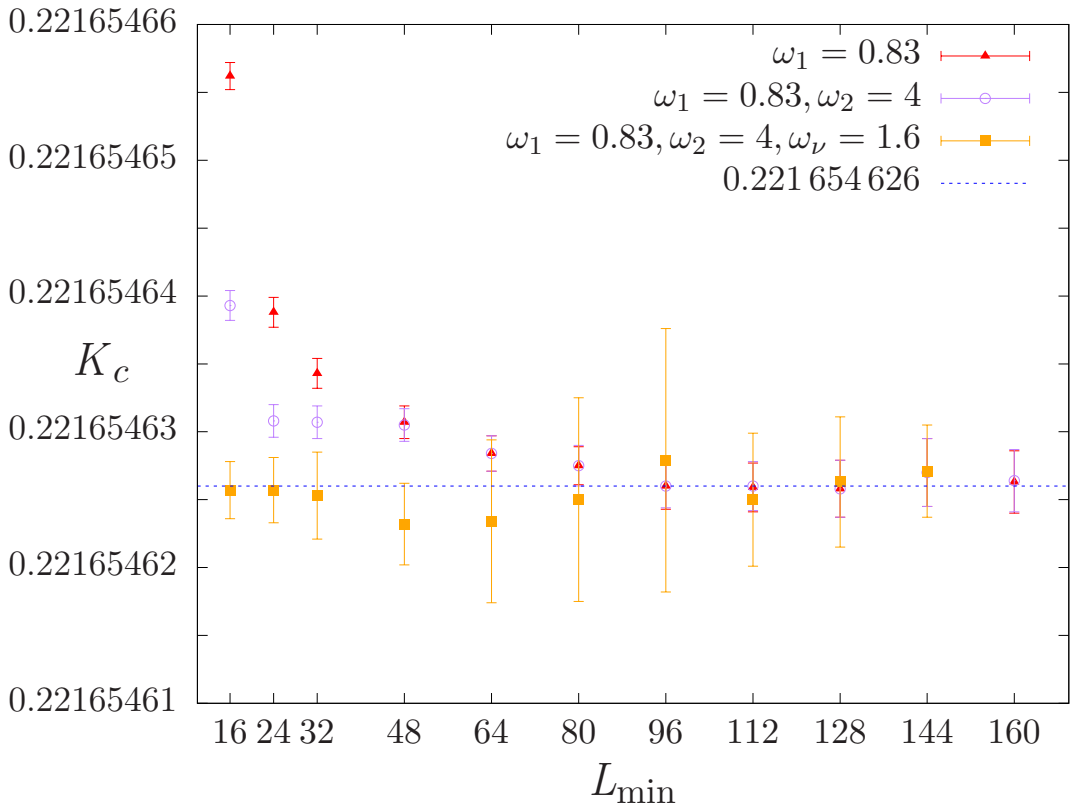

Figure 3.5: Results for the critical coupling K_c when considering one fixed correction exponent $\omega_1 = 0.83$, two fixed exponents $\omega_1 = 0.83$, $\omega_2 = 4$, and three fixed exponents $\omega_1 = 0.83$, $\omega_2 = 4$, $\omega_\nu = 1.6$ as a function of $L_{\min}$.

- χ^2 per dof $= 2.89$, if $L_{\min} = 144$ for $\partial U_4/\partial K$,
- χ^2 per dof $= 2.84$, if $L_{\min} = 144$ for $\partial U_6/\partial K$.

We argue that this is because of the lack of degrees of freedom when $L_{\min}$ is large.

The estimated value for the critical coupling K_c appears to be statistically fluctuating. The fluctuation of K_c when $L_{\min} \leq 80$ is larger than the one when $L_{\min} \geq 80$. Additionally, finite-size effects reduce for larger lattice sizes. Based on the average of K_c for $L_{\min} = 80$ to 144, we estimate $K_c = 0.221\,654\,626\,2$. Similarly, a jackknife analysis has been done on the estimates for the error bar of K_c which are obtained from the three correction terms analysis. Table 3.6 shows the results.

Table 3.6: Results for the critical coupling K_c from jackknife analysis on estimates for K_c that are from the three correction terms analysis with Eq. (3.8).

$L_{\min}$	K_c
16-144	0.221 654 625 5(42)
24-144	0.221 654 625 4(41)
32-144	0.221 654 625 4(41)
48-144	0.221 654 625 4(40)
64-144	0.221 654 625 8(33)
80-144	0.221 654 626 2(23)
96-144	0.221 654 626 6(18)

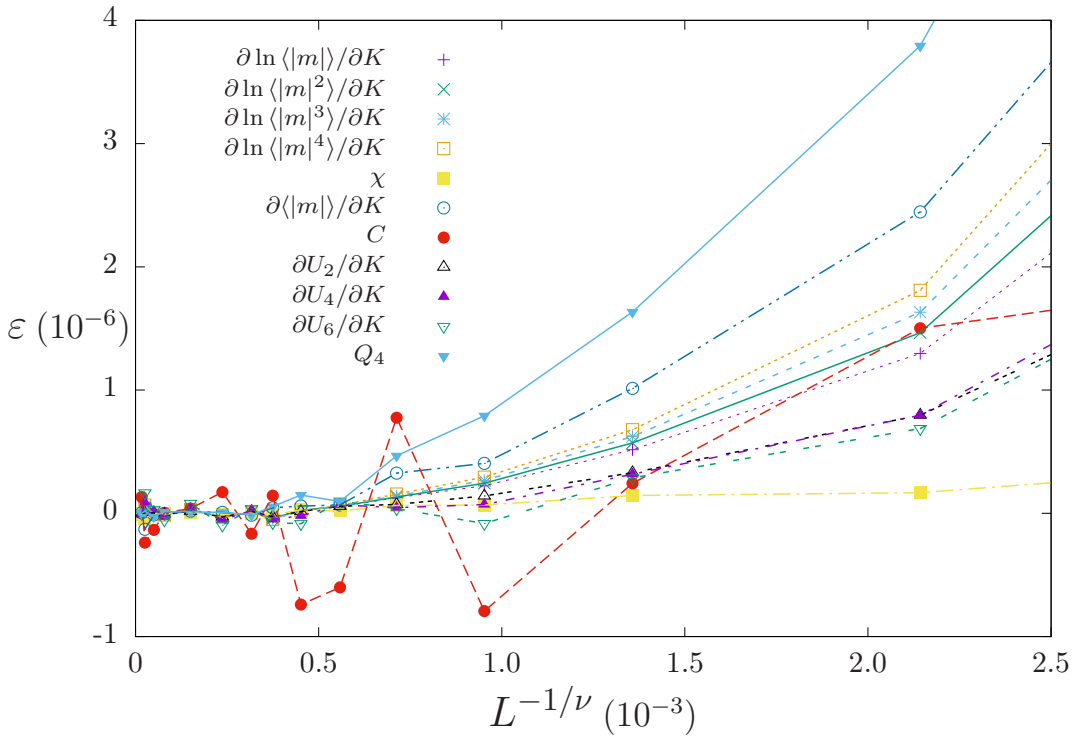

Figure 3.6: Size dependence of the residual difference between measured K_c and fitted values including one fixed correction term.

Based on values of $L_{\min}$ from 80 to 144, we estimate $K_c = 0.221\,654\,626\,2(23)$, whereas using $L_{\min} = 16$ to 144, the estimate for the critical coupling is, $K_c = 0.221\,654\,625\,5(42)$. Therefore, we conclude that from the finite-size scaling analysis, with conservative error bars, is

$$K_c = 0.221\,654\,626(5). \tag{3.9}$$

As seen in Fig. 3.6, effects of higher order correction terms are clearly visible.

3.1.3 Crossing technique of the 4th-order magnetization cumulant

As the lattice size $L \to \infty$, the fourth-order magnetization cumulant $U_4 \to 0$ for $K < K_c$ and $U_4 \to 2/3$ for $K > K_c$ [54]. For large enough lattice sizes, curves for U_4 cross as a function of inverse temperature at a "fixed point" U^*, and the location of the crossing "fixed point" is K_c. Because the lattices are not infinitely large, finite-size correction terms have to be taken into account, and not all curves cross at a common intersection point (as in Fig. 3.7). However, Fig. 3.7 gives us a preliminary estimate for K_c.

The locations of the cumulant crossings between two system sizes have been fitted to Eq. (2.21) with one correction term. All of the fitting parameters are unknown and allowed to vary independently (no fixed values for ν and ω). Table 3.7 shows the corresponding results, where $L_{\min}$ is the minimum lattice size taken into account.

In addition, the locations of the cumulant crossings have been fitted to Eq. (2.21) with two correction terms. Results are shown in Table 3.8.

For $L_{\min} \geq 80$, the calculation gives identical values for the two correction exponents. This is because we lack precision to include two correction terms for the crossing technique.

In Fig. 3.8, the critical coupling appears to be stable when $L_{\min} \geq 96$. By taking the average of K_c values for $L_{\min} \geq 96$, the value of K_c is estimated to be $0.221\,654\,628\,4$. A

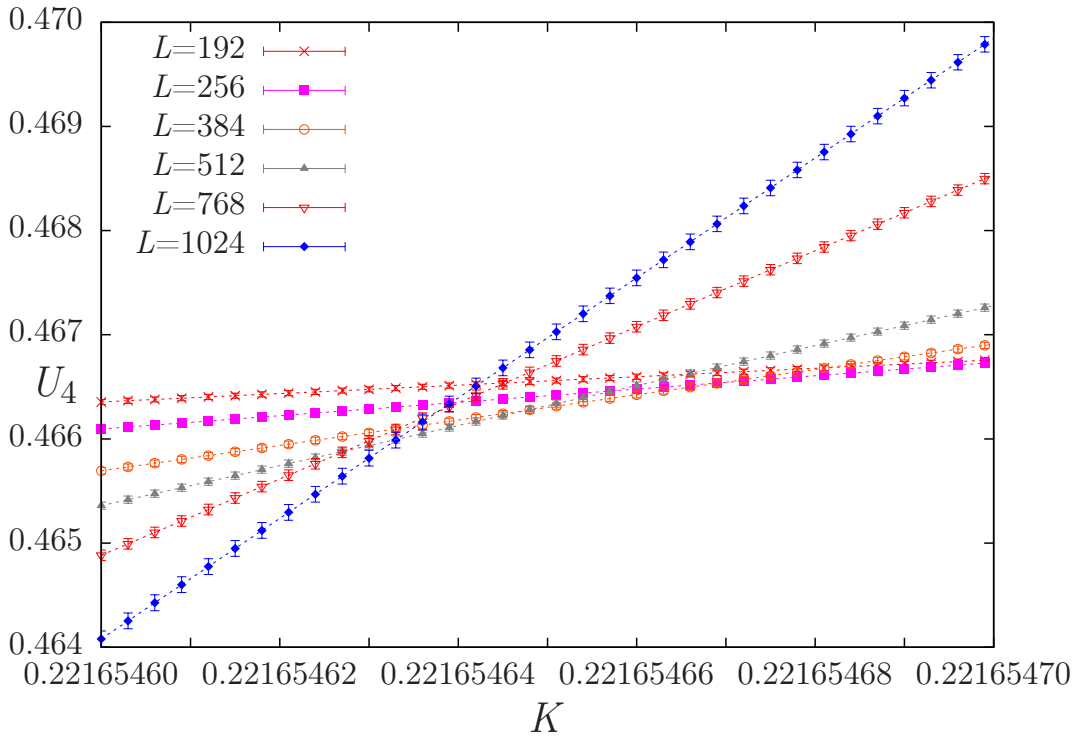

Figure 3.7: Inverse temperature K dependence of the fourth-order magnetization cumulant U_4 for $L \times L \times L$ Ising lattices.

Table 3.7: Results for the critical coupling K_c obtained using the cumulant crossing technique with one correction term.

$L_{\min}$	K_c	dof	χ^2 per dof
16	0.221 654 628 72(41)	131	1.64
24	0.221 654 626 85(50)	115	1.10
32	0.221 654 626 17(58)	100	1.06
48	0.221 654 624 63(75)	86	0.88
64	0.221 654 625 44(91)	73	0.89
80	0.221 654 626 3(11)	61	0.90
96	0.221 654 627 7(12)	50	0.84
112	0.221 654 628 0(15)	40	0.93
128	0.221 654 628 4(17)	31	1.04
144	0.221 654 627 8(22)	23	1.18
160	0.221 654 629 3(24)	16	1.29
192	0.221 654 629 5(33)	10	1.70

Table 3.8: Results for the critical coupling K_c by using cumulant crossing technique with two correction terms.

$L_{\min}$	K_c	dof	χ^2 per dof
16	0.221 654 624 83(95)	129	0.94
24	0.221 654 624 9(10)	113	0.96
32	0.221 654 624 50(80)	98	0.85
48	0.221 654 624 63(85)	84	0.90
64	0.221 654 625 4(10)	71	0.91

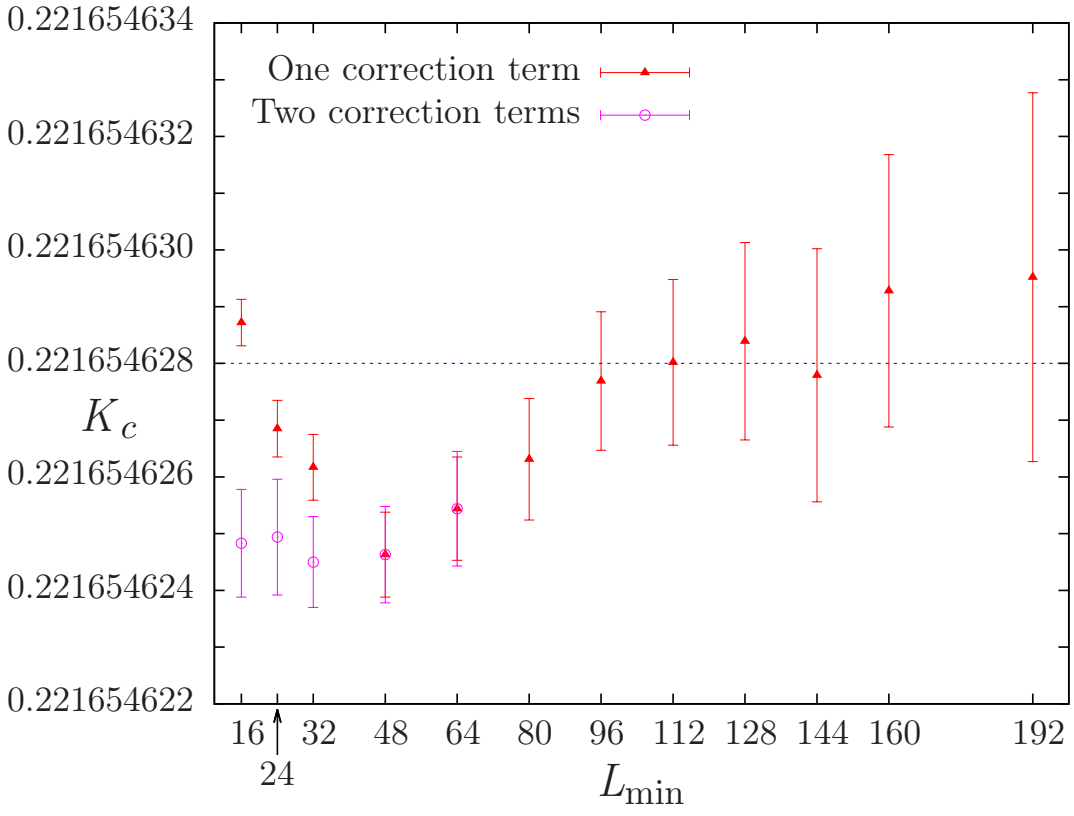

Figure 3.8: Results for the critical coupling K_c using cumulant crossings with one correction term and two correction terms as a function of the minimum size used in the fits $L_{\min}$.

Table 3.9: Results for the critical coupling K_c by using jackknife analysis on estimates for K_c that are from the cumulant crossing technique with one correction term analysis for different ranges shown.

$L_{\min}$	K_c
16-144	0.221 654 627 4(49)
24-144	0.221 654 627 3(47)
32-144	0.221 654 627 3(46)
48-144	0.221 654 627 5(45)
64-144	0.221 654 627 8(34)
80-144	0.221 654 628 1(24)
96-144	0.221 654 628 4(16)
112-144	0.221 654 628 6(14)
128-144	0.221 654 628 7(12)

jackknife analysis has been done on the estimates for the error bar of K_c which are from the one correction term analysis. Results are shown in Table 3.9.

Using results for $L_{\min}$ (96 to 192) we estimate

$$K_c = 0.221\,654\,628(2). \tag{3.10}$$

3.1.4 Alternative finite-size scaling analysis

In Sec. 3.1.1, a finite-size scaling analysis was performed based on the magnitude of quantities at the peak locations. Alternatively, critical exponents can be estimated by looking at quantities at the estimate for K_c (denoted $K_c^{est} = 0.221\,654\,626$, i.e. the estimated value for infinite critical coupling K_c).

$$X(K = K_c^{est}) = X_0 L^{\lambda}(1 + a_1 L^{-\omega_1} + \cdots), \tag{3.11}$$

where X is the quantity being applied to determine the critical exponent λ. As for the susceptibility and the specific heat Eq. (3.11) includes an analytic background term.

The critical exponent ν can be estimated from derivatives of magnetization cumulants and logarithmic derivatives of the magnetization at K_c^{est}. By including three fixed correction exponents to the fitting model, calculating the jackknife covariance matrix, and performing the cross correlation analysis, we find ν to be

$$\nu = 0.629\,93(10). \tag{3.12}$$

This result is consistent with $\nu = 0.629\,912(86)$, the value of ν estimated from Eq. (3.6).

By examining the scaling behavior of the susceptibility at K_c^{est}, we have found that $\gamma/\nu = 1.963\,90(45)$. Combining this value with our estimate for ν from Eq. (3.6), and assuming that exponent estimates for γ and ν are independent, we have determined the critical exponent γ of the magnetic susceptibility to be

$$\gamma = 1.237\,08(33). \tag{3.13}$$

Also, we performed an analysis of the susceptibility at constant U_4 as suggested by Hasenbusch [37]. Fixing $U_4 = 0.4655$ and including the higher order confluent corrections to scaling we found that $\gamma = 1.237\,01(28)$, a value that is almost identical to, and with only a slightly smaller error bar than $\gamma = 1.237\,08(33)$, the value obtained from finite-size scaling of the susceptibility.

Similarly, by considering the critical behavior of $|m|$ at K_c^{est}, we obtained $\beta/\nu = 0.518\,01(35)$, or

$$\beta = 0.326\,30(22). \tag{3.14}$$

Because of the large analytic background in the specific heat (see Eq. (2.14)), it was not possible to extract estimates of the exponent α with comparable precision to the other exponents evaluated here. For this reason, we have not quoted an estimated value.

3.2 Probability distribution $P(m)$ of the order parameter m

The probability distribution $P(m)$ of the order parameter m is a seminal quantity for studying the finite-size scaling of critical phenomena. It contains the information needed to calculate all order parameter related quantities such as the Binder cumulant $U_4 = 1 - \langle m^4 \rangle / (3 \langle m^2 \rangle^2)$, the susceptibility $\chi = K(\langle m^2 \rangle - \langle m \rangle^2)$, etc. Also, it can complement the use of critical exponents in determining the critical behavior of a universality class.

According to finite-size scaling theory [54, 55], and assuming hyperscaling and using L (linear dimension), m (order parameter), and ξ (correlation length) as variables, the probability distribution of the order parameter is described by the scaling ansatz,

$$P(m, L, \xi) = L^{\beta/\nu} \tilde{P}(mL^{\beta/\nu}, L/\xi), \tag{3.15}$$

where β is the order parameter exponent, ν is the correlation length exponent, and $\tilde{P}(mL^{\beta/\nu}, L/\xi)$ is the scaling function.

Fig. 3.9 shows the scaled probability distribution $P(m)L^{-\beta/\nu}$ as a function of $mL^{\beta/\nu}$ at the critical point $K_c = 0.221\,654\,626$ for finite lattice sizes ($L = 16$, 32, 96, and 256). Here, β and ν are critical exponents for infinite lattices, and $\beta/\nu = 0.518\,01(35)$ [2]. The peak values of the scaled $P(m)L^{-\beta/\nu}$ decreases as the lattice size L increases. Also, systematic deviations from scaling occur in the region of the tails of the distributions. In the thermodynamic limit ($L = \infty$), the probability distribution $P(m)$ should be universal up to a rescaling of m.

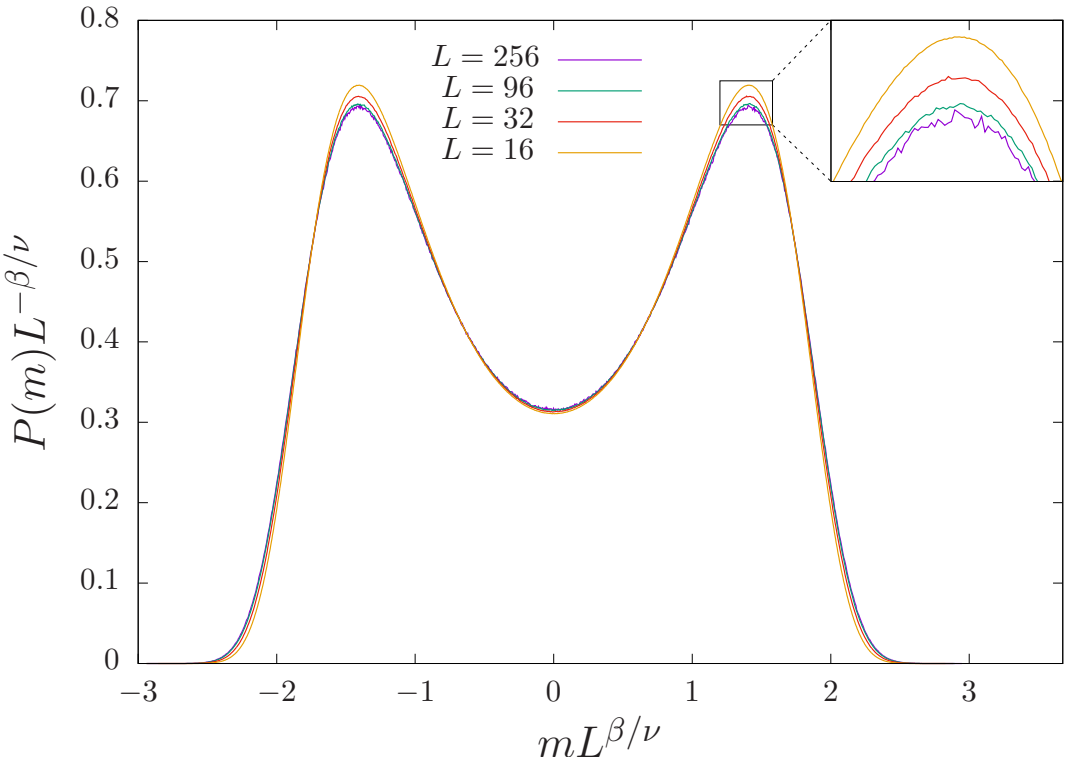

Figure 3.9: Scaled probability distribution $P(m)L^{-\beta/\nu}$ as a function of $mL^{\beta/\nu}$ at the critical point $K_c = 0.221\,654\,626$ [2].

Based on the estimate for the critical point in Sec. 3.1.2, data were reweighted to $K_c = 0.221\,654\,626$ by using histogram reweighting techniques [18, 19]. To obtain the probability distribution $P(m)$ at K_c, for each occurrence of the order parameter, the corresponding population of the bin of the histogram was incremented by $\exp((K_0 - K_c)E)$, where E is the total dimensionless energy of the system. The histogram was then normalized to determine $P(m)$.

3.2.1 Simple ansatz

First, we performed a nonlinear least-squares fit, where the reciprocals of the statistical errors were taken as the weighting factors to the loss function, with the "improved" ansatz

of Ref. [56],

$$P(m) = AL^{\beta/\nu} \exp\left\{ -\left[\left(\frac{mL^{\beta/\nu}}{m_0} \right)^2 - 1 \right]^2 \left[b \left(\frac{mL^{\beta/\nu}}{m_0} \right)^2 + c \right] \right\}, \tag{3.16}$$

where A, m_0, b, and c are unknown fitting parameters, and $\beta/\nu = 0.51801(35)$. Note that m_0 is a scale-invariant (but not universal) quantity.

Fig. 3.10 shows the difference between the Monte Carlo data and the fit corresponding to Eq. (3.16). It also illustrates the error bars for the Monte Carlo data. From Fig. 3.10 we observe that when the lattice size L is small, e.g. $L = 16$, a pattern in the difference between MC data and the fit is very clear. This means that the fitting ansatz, Eq. (3.16), does not perform well for small L to within the statistical uncertainty. For larger L (e.g. $L = 1024$), the difference between the distribution and the fit to the ansatz is of the same magnitude as the statistical error, so no systematic deviation is observed.

Table 3.10 shows the results of fitting the data to Eq. (3.16). We can tell that the quality of fit is not good when $L \leq 80$, as the value of the χ^2 per degree of freedom (p.o.f.) is large. It decreases for larger L, and the quality of fit becomes good for the largest lattice sizes.

Based on the variance of the fit parameters b and c of Eq. (3.16) for different lattice sizes, we have estimated their values and errors for $L = \infty$ as,

$$b = 0.1553(6), \quad c = 0.7783(4). \tag{3.17}$$

Ref. [56] determined the less precise values $b = 0.158(2)$ and $c = 0.776(2)$ which agree with our results within the error bars.

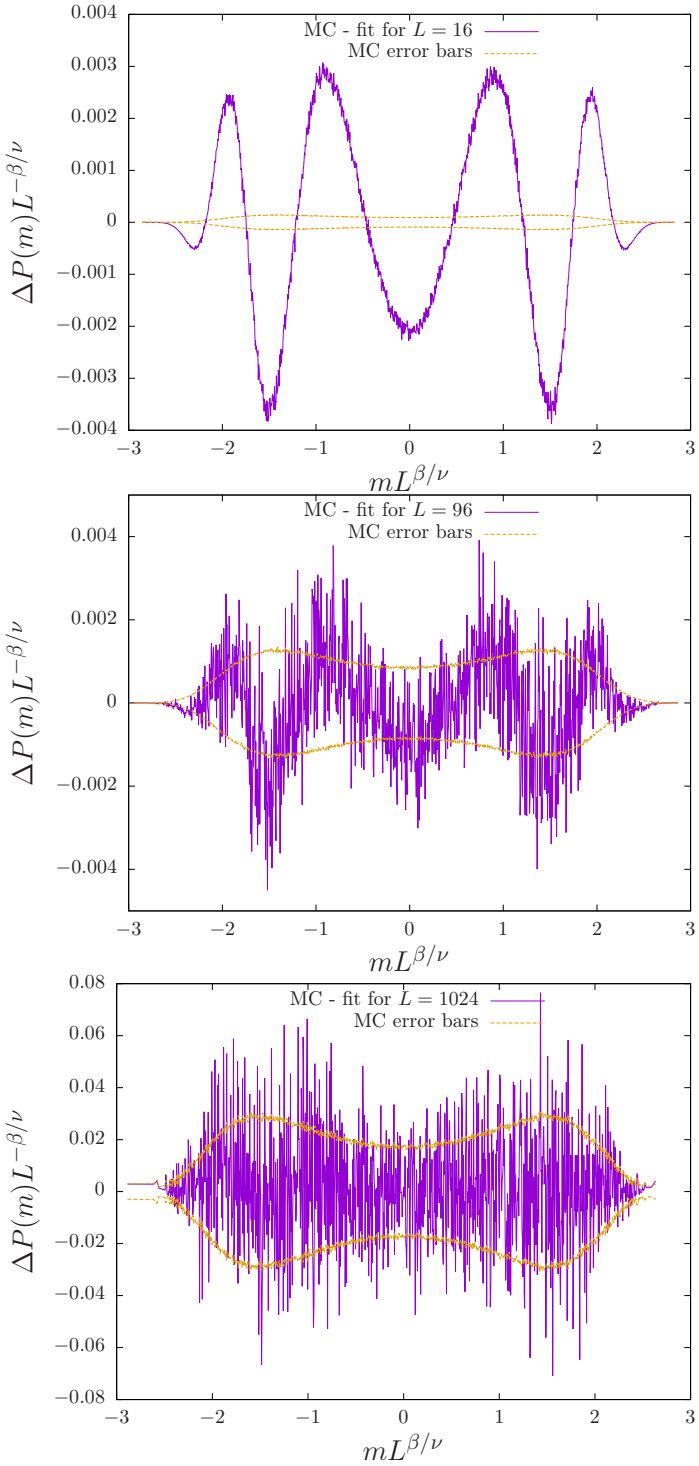

Figure 3.10: The purple (dark grey) line is the difference between the Monte Carlo data and the fit corresponding to Eq. (3.16), while the orange (light grey) line is the error bar for the Monte Carlo data (top: $L = 16$, middle: $L = 96$, bottom: $L = 1024$).

Table 3.10: The parameters m_0, b, and c for the probability distribution $P(m)$, fitted to the ansatz Eq. (3.16). The last column χ^2 per degree of freedom (dof) characterizes the quality of the fit.

L	m_0	b	c	χ^2 per dof
16	1.411 97 (26)	0.2408 (17)	0.836 86 (77)	381.82
24	1.411 12 (12)	0.209 24 (70)	0.819 38 (40)	70.96
32	1.410 761 (82)	0.195 20 (48)	0.810 45 (21)	24.87
48	1.410 437 (74)	0.181 97 (43)	0.800 87 (25)	6.98
64	1.410 440 (46)	0.176 01 (29)	0.796 07 (26)	3.70
80	1.410 351 (48)	0.172 20 (31)	0.793 03 (33)	2.23
96	1.410 345 (57)	0.169 77 (35)	0.791 04 (34)	1.74
112	1.410 250 (59)	0.167 85 (37)	0.789 39 (42)	1.47
128	1.410 362 (71)	0.166 74 (46)	0.788 09 (36)	1.32
144	1.410 153 (85)	0.165 37 (54)	0.786 93 (37)	1.24
160	1.410 217 (98)	0.164 62 (62)	0.786 39 (42)	1.18
192	1.410 189 (67)	0.163 36 (85)	0.784 99 (46)	1.12
256	1.410 281 (87)	0.1620 (11)	0.783 59 (47)	1.08
384	1.410 18 (11)	0.1560 (14)	0.781 98 (49)	1.04
512	1.410 33 (19)	0.1589 (16)	0.781 04 (71)	1.02
768	1.411 06 (48)	0.1575 (43)	0.781 68 (77)	1.02
1024	1.410 65 (66)	0.1544 (82)	0.780 76 (98)	1.01

3.2.2 Sophisticated ansatz

The systematic deviation observed for smaller system sizes led us to modify ansatz Eq. (3.16) by adding various forms of correction terms to see if a revised ansatz could fit the data well even for smaller lattices. We approximated $P(m)$ by using different forms, e.g. adding correction terms in the exponent, adding different correction terms in the pre-exponential factor ($|m|^\omega, |m|, |m|^2, ...$), and adding correction terms in both the exponent and the pre-exponent factor. We have found that the following "improved" ansatz gives a surprisingly

good approximation to $P(m)$ over quite a wide range of L and m:

$$P(m) = AL^{\beta/\nu} \exp\left\{ -\left[\left(\frac{mL^{\beta/\nu}}{m_0} \right)^2 - 1 \right]^2 \left[a \left(\frac{mL^{\beta/\nu}}{m_0} \right)^4 + b \left(\frac{mL^{\beta/\nu}}{m_0} \right)^2 + c \right] \right\}, \quad (3.18)$$

where A, m_0, a, b, and c are unknown fit parameters, and as before $\beta/\nu = 0.51801(35)$.

Fig. 3.11 is analogous to Fig. 3.10, but shows the difference between the Monte Carlo data and the fits to Eq. (3.18). Based on Fig. 3.11, one can see that even for $L = 16$ the residual discrepancy is comparable to the statistical error. By using Eq. (3.18) as the fitting function, the maximal difference between MC data and the fit for $L = 16$ is around 0.0004, which is 1/10 of that in Fig. 3.10 which used Eq. (3.16) as the fitting function. Thus, the quality of fitting to ansatz Eq. (3.18) is much higher than that of Eq. (3.16) for small L, and within the statistical errors, Eq. (3.18) performs much better than Eq. (3.16) as a fitting function.

Results for fitting to the functional form Eq. (3.18) are shown in Table 3.11. The values of the χ^2 per dof show that the quality of fit is good even for small lattice sizes. Generally speaking, the error bars for the fit parameters (m_0, a, b, and c) become larger as L increases. This is because the statistical errors of the raw data are greater for larger lattice sizes (see the dashed line in Fig. 3.11).

Fig. 3.12 shows the results of the fit parameters a, b, and c of the probability distribution $P(m)$, approximated by the ansatz Eq. (3.18). The horizontal axis is chosen to be $L^{-\omega}$, where $\omega = 0.8303(18)$ [4], so that the leading corrections to scaling are linearized [54]. There is an apparent deviation for $L = 768$ and $L = 1024$, but the error bars for those sizes are so large that their contributions to the fit are less significant. (There are many more "bins" in the histogram for very large L so there are fewer entries in each bin.) To within statistical errors, there are noticeable finite-size effects for a, b, and c. By doing extrapolations to the

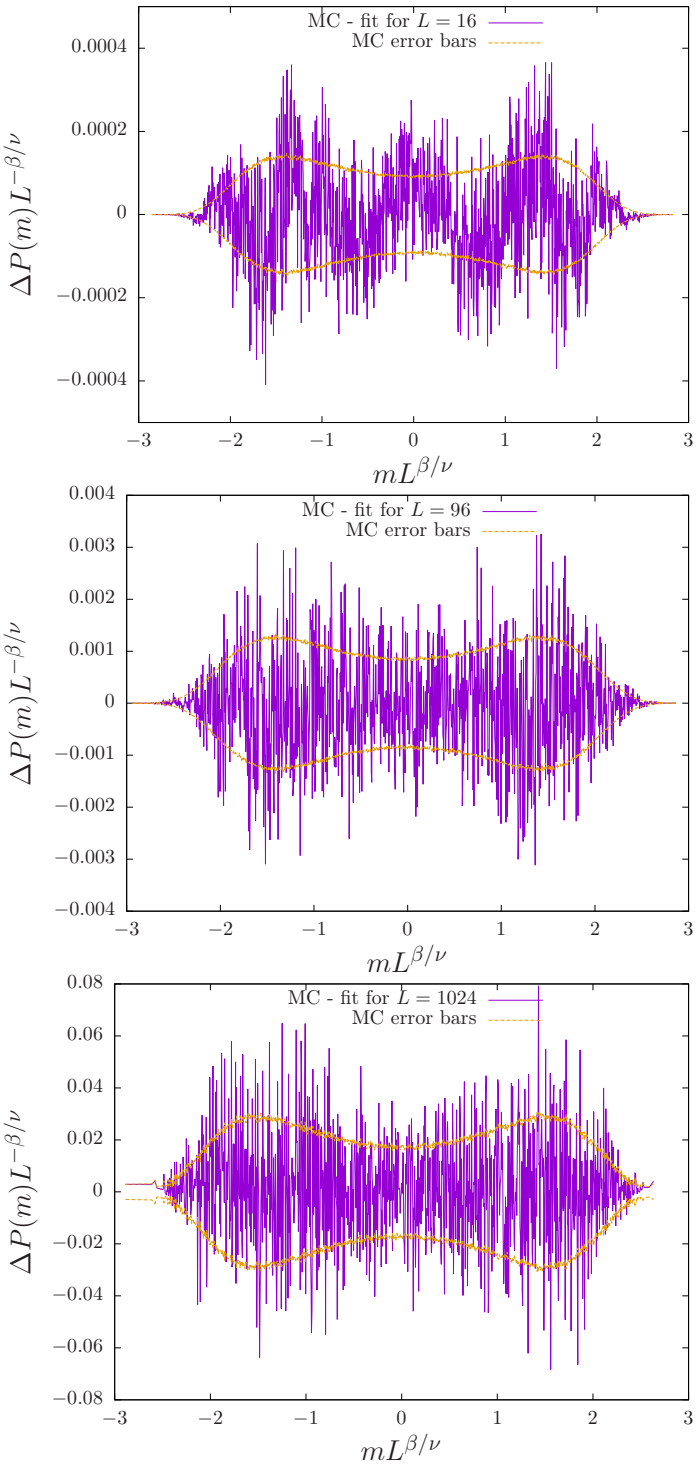

Figure 3.11: Analogous to Fig. 3.10, but the fit is corresponding to Eq. (3.18) (top: $L = 16$, middle: $L = 96$, bottom: $L = 1024$).

Table 3.11: The parameters m_0, a, b, and c for the probability distribution $P(m)$, fitted by the ansatz Eq. (3.18). The last column χ^2 per degree of freedom (dof) characterizes the quality of the fit.

L	m_0	a	b	c	χ^2 per dof
16	1.408 684 (19)	0.025 01 (21)	0.169 36 (31)	0.839 36 (33)	1.31
24	1.408 497 (27)	0.016 44 (15)	0.160 64 (23)	0.821 24 (36)	1.03
32	1.408 456 (44)	0.013 10 (14)	0.155 53 (12)	0.812 03 (26)	1.04
48	1.408 432 (61)	0.010 46 (15)	0.150 02 (24)	0.802 20 (27)	1.02
64	1.408 588 (49)	0.009 26 (21)	0.147 51 (29)	0.797 27 (31)	1.03
80	1.408 573 (53)	0.008 62 (25)	0.145 55 (40)	0.794 16 (39)	1.02
96	1.408 611 (73)	0.008 22 (27)	0.144 27 (54)	0.792 13 (45)	1.02
112	1.408 564 (70)	0.007 84 (28)	0.143 47 (75)	0.790 43 (51)	1.01
128	1.408 714 (64)	0.007 54 (36)	0.143 26 (61)	0.789 10 (48)	1.02
144	1.408 490 (82)	0.007 48 (45)	0.142 07 (76)	0.787 93 (55)	1.02
160	1.408 580 (92)	0.007 27 (56)	0.141 94 (93)	0.787 36 (48)	1.01
192	1.408 497 (91)	0.007 31 (52)	0.140 53 (99)	0.785 97 (42)	1.01
256	1.408 672 (95)	0.006 75 (65)	0.1409 (12)	0.784 48 (58)	1.01
384	1.408 489 (87)	0.006 57 (74)	0.1396 (20)	0.782 80 (89)	1.01
512	1.408 55 (12)	0.006 01 (98)	0.1404 (26)	0.7817 (15)	1.01
768	1.408 87 (20)	0.0047 (16)	0.1434 (59)	0.7821 (19)	1.01
1024	1.408 72 (29)	0.0036 (26)	0.1462 (91)	0.7806 (29)	1.01

thermodynamic limit, their values are estimated as follows,

$$a = 0.0050(6), \quad b = 0.137(1), \quad c = 0.7785(3). \tag{3.19}$$

Comparing the results of fitting to the two ansatzes, Eq. (3.16) and Eq. (3.18), one can see that the estimates for c from both fits agree with each other to within error bars. However, the value of b determined for Eq. (3.16) is larger than that for Eq. (3.18). We believe that this is a consequence of the correction term corresponding to b in Eq. (3.16) attempting to account for additional finite-size corrections which are addressed explicitly by the term corresponding to a in Eq. (3.18).

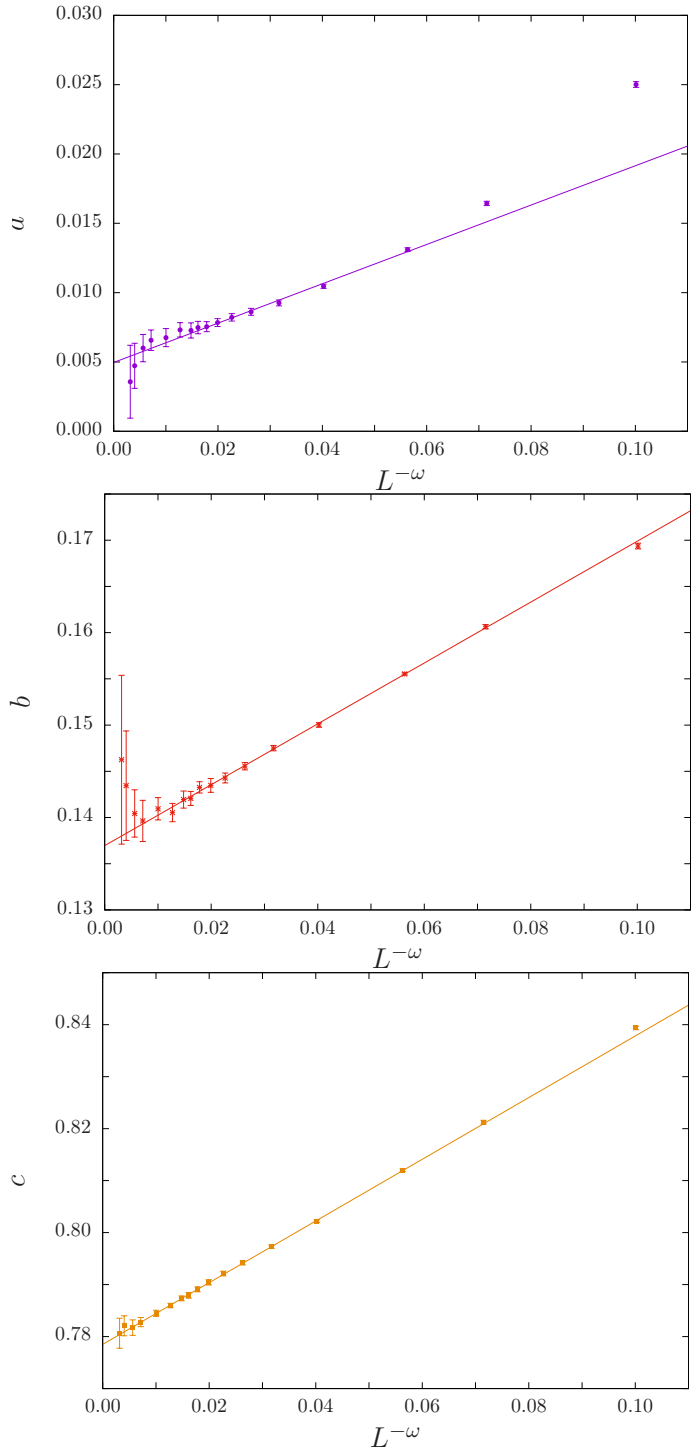

Figure 3.12: Variation of fitting parameters a, b, and c for ansatz Eq. (3.18) as functions of $L^{-\omega}$. The abscissa is chosen such that the leading corrections to scaling could be linearized [3], where $\omega = 0.8303(18)$ [4]. The solid lines show extrapolations to $L = \infty$ for $L \geq 32$.

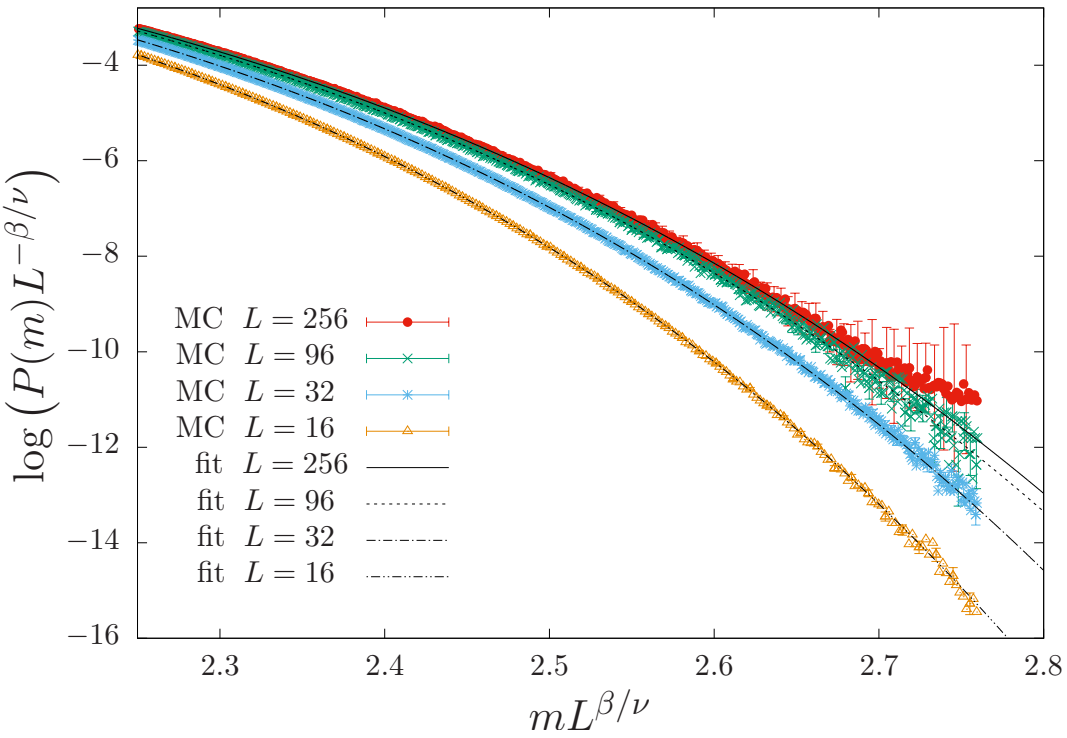

Figure 3.13: Tail probability distribution of the order parameter (average of the left and right tails) in the log scale, where $mL^{\beta/\nu} \geq 2.25$, for different lattice sizes L. The lines are the best fits with Eq. (3.18).

Overall, we have observed that the functional form Eq. (3.18) permits a high quality nonlinear least-squares fit to the $P(m)$ data. Although the quality of fit for Eq. (3.16) is reasonable for large lattice sizes, it is poor for small lattice sizes. The addition of a correction term (Eq. (3.18)) allows for a high-quality fit for $P(m)$ over a larger range of system sizes. We have observed a noticeable finite-size effect for the fit parameters a, b, and c, thus Eq. (3.18) is a high-resolution approximation expression for $P(m)$ in the thermodynamic limit.

3.2.3 Tail distribution

The tails of the order parameter probability distributions have relatively few entries and do not contribute substantially to the fits. Therefore, we examine them in a finer manner.

Fig. 3.13 shows the logarithm of the tail distributions, where $mL^{\beta/\nu} \geq 2.25$. The values of the MC data are the averages of the left and right tails. The solid lines are the best fits to Eq. (3.18). The tail data for $L = 256$ fluctuate too much to present clearly in the figure. Therefore, we applied a smoothing technique, where each data point is the mid-point of a linear fit to 10 consecutive points. The shape of the scaled probability distribution differs noticeably from the thermodynamic limit, as there are non-negligible corrections to scaling. The values of $P(m)$ are small at the tail region, and their statistical errors are relatively high, thus, data in the tails contribute less to the fit than those near the peaks. Although their contributions are less significant, Fig. 3.13 still indicates that the fit by Eq. (3.18) performs relatively well in the tail region, at least for $mL^{\beta/\nu} \leq 2.75$.

3.3 Self-consistency check

Inspired by a recent work [57], where the 3D percolation was studied by Monte Carlo simulations, the quoted error bar can be justified by observing the Monte Carlo data away from the critical point by 3 error bars. The underlying idea is that if the quoted error bar is reliable, the off-critical behavior would be noticeable in the Monte Carlo data at points away from the estimated value by a few times of the error bar.

Following is the cumulant's ansatz [3],

$$U_4(L) = U^*(1 + cL^{-\omega_1}), \tag{3.20}$$

where $U_4(L)$ is the fourth-order cumulant for system size L and U^* is the "fixed point".

To justify our quoted error bars for the crossing technique, $K_c = 0.221\,654\,628(2)$, we performed an analysis for the fourth-order magnetization cumulant at $K = 0.221\,654\,622$, $0.221\,654\,628$, and $0.221\,654\,634$ respectively in Fig. 3.14. The value of parameter c was

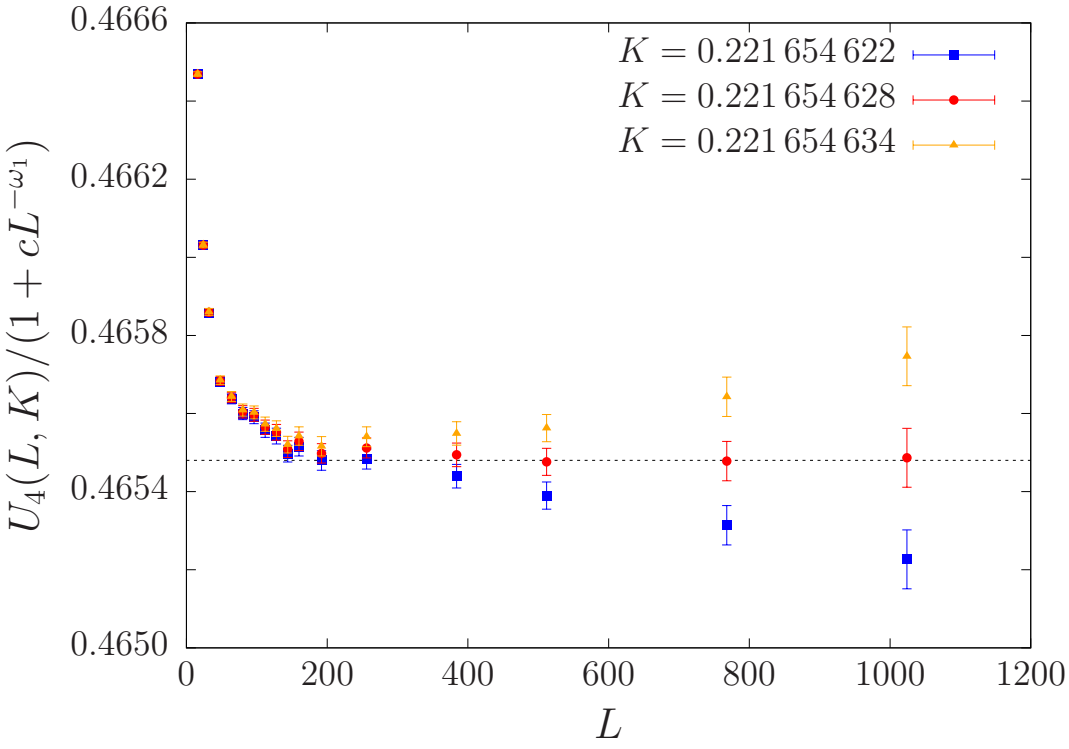

Figure 3.14: Plot of the fourth-order magnetization cumulant as a function of L for fixed K values. The value of c was estimated by doing a fit for U_4 by Eq. (3.20). The dashed line indicates our asymptotic value for U^*.

estimated by doing a fit for the cumulant by Eq. (3.20). It was generated at the estimated critical coupling, with a fixed correction exponent $\omega_1 = 0.83$, over the range of $L = 144$ to 1024. It can be seen that, the data at $K = 0.221\,654\,622$ and $K = 0.221\,654\,634$ begin to diverge as L increases, while the data at $K = 0.221\,654\,628$ converge to $U^* = 0.465\,48(5)$. Our estimate agrees with $0.465\,45(13)$ from Blöte et al [58], but higher than $0.465\,306(34)$ from Deng and Blöte [59].

Likewise, a plot of the derivative of the fourth-order magnetization cumulant is shown in Fig. 3.15. Based on the FSS estimate $K_c = 0.221\,654\,626(5)$ in Sec. 3.1.2, the data away from the estimated critical point by 3 error bars have a noticeable divergence.

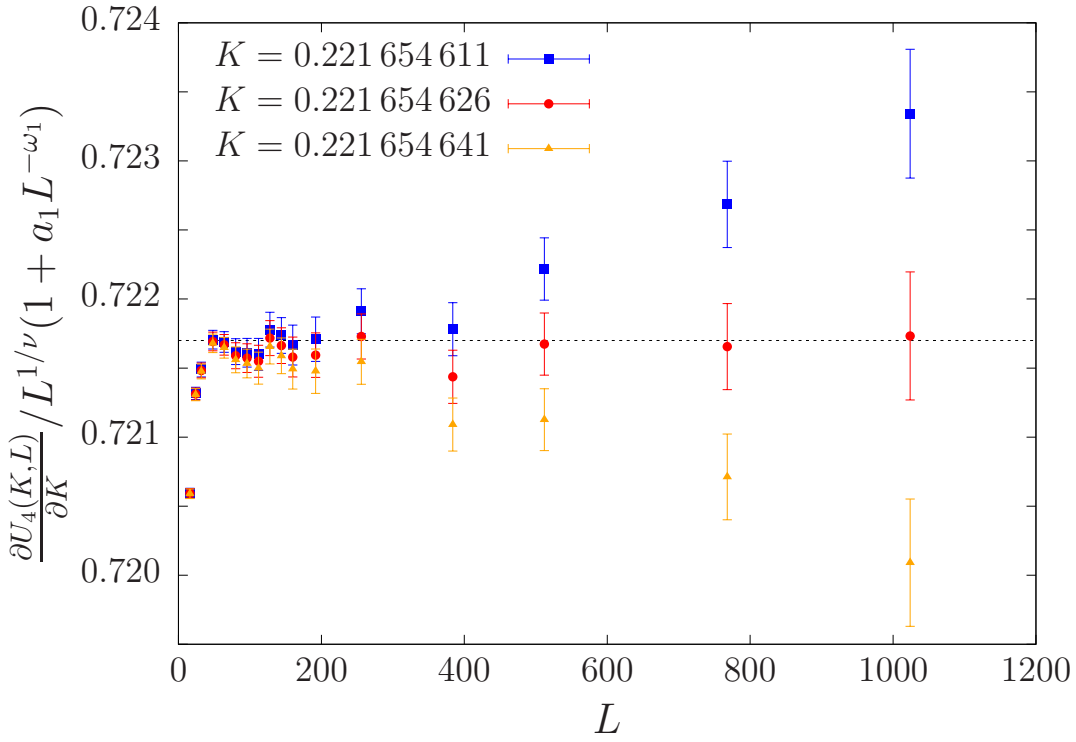

Figure 3.15: Plot of the derivative the 4th order magnetization cumulant as a function of L for fixed K values. The value of a_1 was estimated by doing a fit for $\partial U_4/\partial K$ by Eq. (3.11).

All in all, Fig. 3.14 and Fig. 3.15 indicate that our quoted error bars for K_c from the crossing technique and the FSS are reliable.

3.4 Discussion

The combination of an efficient cluster-flipping Wolff algorithm, histogram reweighting technique, a cross-correlation jackknife analysis, and high statistics data processing enables us to achieve the high resolution results presented in this work. Table 3.12 and Fig. 3.16 shows the comparison between estimates for K_c and ν with other high-resolution results from simulation and theory. In Fig. 3.16, the boxes represent the quoted error bars in both ν and K_c assuming independent errors.

Table 3.12: Comparison of our results for the critical coupling K_c and the critical exponents ν, γ with other recently obtained values. The number marked with * is not given by the reference directly, but is calculated by Fisher's scaling law $\gamma = \nu(2 - \eta)$. The error is calculated using simple error propagation, which assumes that ν and η are independent and uncorrelated.

[a] Special purpose computer.
[b] Monte Carlo study of the non-linear relaxation function.
[c] Conformal bootstrap

Reference	Method	K_c	ν	γ
Butera and Comi(2002) [31]	HT series	0.221 655(2)	0.629 9(2)	1.237 1(1)
Blöte et al.(1999) [58][a]	MC	0.221 654 59(10)	0.630 32(56)	1.237 2(13)*
Deng and Blöte(2003) [59]	MC	0.221 654 55(3)	0.630 20(12)	1.237 2(4)*
Ozeki and Ito(2007) [26][b]	MC NLR	0.221 654 7(5)	0.635(5)	1.255(18)*
Weigel and Janke(2010) [21]	MC	0.221 657 03(85)	0.630 0(17)	1.240 9(62)*
Hasenbusch(2010) [37]	MC	0.221 654 63(8)	0.630 02(10)	1.237 19(21)*
Kaupužs(2011) [38]	MC	0.221 654 604(18)		
Kos et al.(2016) [36][c]	CB		0.629 971(4)	1.237 075(8)*
Wang et al.(2014) [40]	tensor RG	0.221 654 555 5(5)		
Rosengren(1986) [33]	conjecture	$0.221\,658\,63\cdots$		
This work (no assumptions)	MC	0.221 654 630(7)	0.629 60(15)	1.236 41(45)
This work (constrained fits)	MC	0.221 654 626(5)	0.629 912(86)	1.237 08(33)
This work (U_4 crossings)	MC	0.221 654 628(2)		
This work (constant U_4)	MC			1.237 01(28)

Our estimate for the critical exponent of the correlation length $\nu = 0.629\,912(86)$ (in Sec. 3.1.1) is perfectly consistent (i.e. within error bars) with the recent conformal bootstrap result of Kos et al. [36], as well as that from an older work by El-Showk et al. [4]. In addition, our result agrees with the high-temperature result of Butera and Comi [31], Monte Carlo result of Deng and Blöte [59], and nonequilibrium relaxation Monte Carlo result of Ozeki and Ito [26]. Also, our result agrees well with the Monte Carlo result of Hasenbusch [37] but is lower than that of Weigel and Janke [21]; however, within the respective error bars there is agreement although we have substantially higher precision than either of these pre-

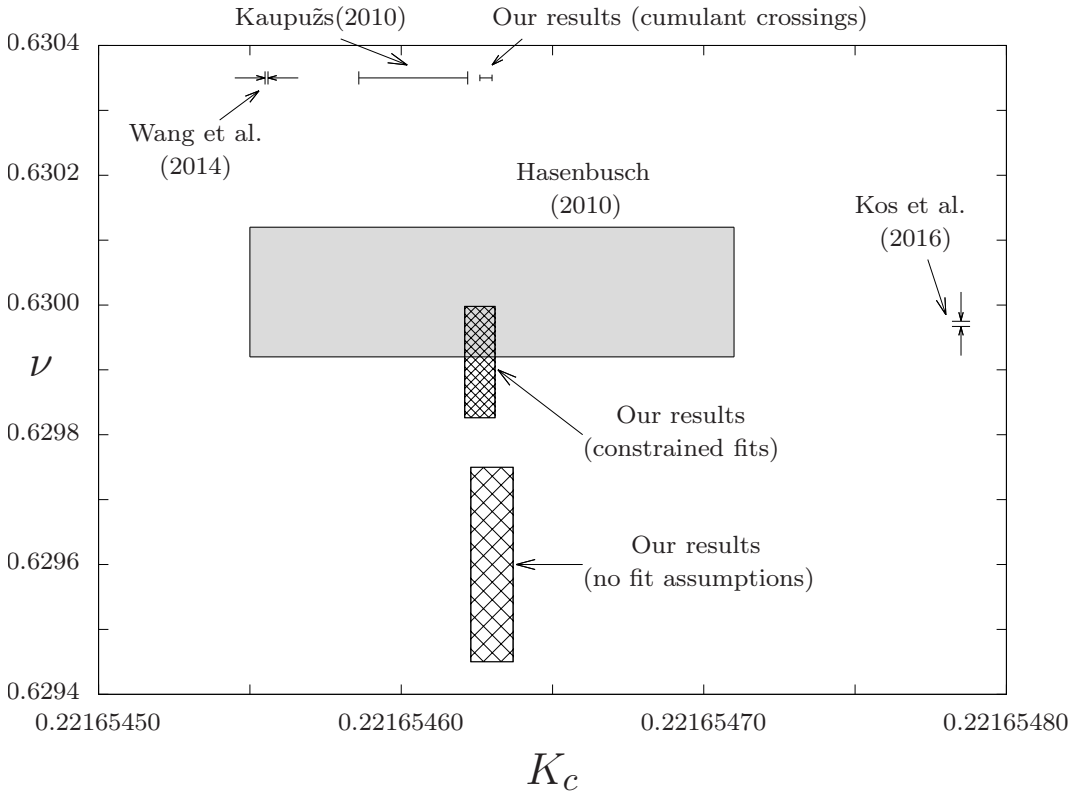

Figure 3.16: Recent high-resolution estimates for K_c and ν obtained using different methods.

vious studies. Our system sizes and statistics are substantially greater than those used by Weigel and Janke, and Hasenbusch examined the behavior of the ratio of partition functions Z_a/Z_p, and the second moment correlation length over the linear lattice size ξ_2/L so the methodologies are not identical. Our estimate for K_c differs from that obtained by Kaupužs et al [38] using a parallel Wolff algorithm by an amount that barely agrees to within the error bars. Somewhat perplexingly, they were able to fit their data to *two* rather different values of ν, so no comparison of critical exponents is possible. The recent tensor renormalization group result for K_c [40] does not agree with our result; in fact the difference is many times the respective error bars.

To place these results in perspective, it is interesting to note that as far back as 1982 Gaunt's high temperature series expansions [60] gave the estimate $K_c = 0.221\,66(1)$ and in 1983 Adler [61] estimated $0.221\,655 < K_c < 0.221\,656$ with confluent corrections included in the analysis.

Neither Rosengren's "exact conjecture" nor Zhang's so-called "exact" solution agree with our numerical values, thus adding further evidence to the already strong arguments that neither are, in fact, correct.

In Sec. 3.1.4, we have estimated the critical exponents by using an alternative finite-size scaling analysis. The critical exponent of the correlation length is estimated to be $\nu = 0.629\,93(10)$, which is consistent with our estimate in Sec. 3.1.1. While our final estimate is slightly lower than the best alternative values, there is agreement to within the error bars. Also, our estimate $\gamma = 1.237\,08(33)$ is consistent with the conformal bootstrap estimates given by Kos et al. [36], El-Showk et al. [4], and slightly smaller than the Monte Carlo estimates by Deng and Blöte [59], Hasenbusch [37], and Weigel and Janke [21]; but, once again, there is overlap within the respective error bars.

Chapter 4

Models and methods for a first-order transition where a continuous symmetry is broken

4.1 Three-dimensional anisotropic Heisenberg model

There has been a great interest in the XXZ Heisenberg antiferromagnetic model in an external field for many years [5, 62–66]. The Hamiltonian of this model is given by,

$$\mathcal{H} = J \sum_{\langle i,j \rangle} [\Delta(S_{ix}S_{jx} + S_{iy}S_{jy}) + S_{iz}S_{jz}] - H \sum_{i} S_{iz}, \tag{4.1}$$

where the classical spins $\mathbf{S}_i$ are unit vectors with components (S_{ix}, S_{iy}, S_{iz}) on sites i of a simple cubic lattice with linear size L, and $J > 0$ is the exchange coupling between nearest-neighbor pairs of spins. Δ is the uniaxial exchange anisotropy, which we set to $\Delta = 0.8$ in this work. (A recent high-resolution study about the 3D XXZ Heisenberg antiferromagnet was implemented with $\Delta = 0.8$.) An external magnetic field H is applied along the z-axis, which

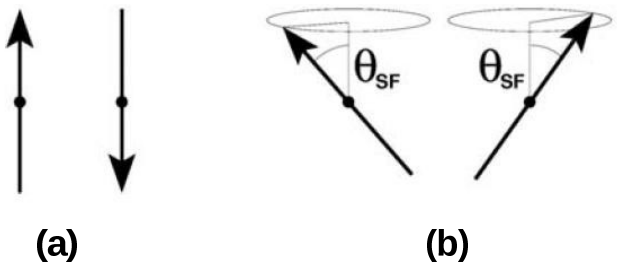

Figure 4.1: Spin configurations for different phases in the XXZ Heisenberg model in an external field. Illustrated are spin configurations of the two sublattices in the (a) antiferromagnetic (AF); and (b) spin-flop (SF) phases. θ_{SF} is the angle that the spins make with respect to the applied field.

is the easy axis of the model. The first summation is over all $\langle i, j \rangle$ pairs of nearest-neighbor sites and the second summation is over all $N = L^3$ spins on the lattice.

The phase diagram has been studied by various methods for many years, e.g. renormalization group [67] and mean field theory [68]. We now believe that an antiferromagnetic (AF) phase exists at low temperature and low field, where the nearest-neighboring spins point in opposite directions along the axis given by the anisotropy (as shown in Fig. 4.1(a)); a spin-flop (SF) phase exists at low T and higher H, in which the spins are tilted with continuous rotational symmetry about the field direction (see Fig. 4.1(b)). In addition, a paramagnetic (P) phase with no long range order exists at high T and/or at high H.

4.2 Related work and remaining questions for the 3D XXZ Heisenberg antiferromagnet

Finite-size scaling at both first-order and second-order transitions between phases with discrete numbers of states is now relatively well established and extremely successful at describing phase transition behavior in the thermodynamic limit from Monte Carlo data produced

for finite-size systems [1, 11, 13, 69–72]. The simplest case of a first-order transition, namely the first-order, field driven transition in the 2-dimensional Ising model below its critical point, was studied using Monte Carlo simulations by Binder and Landau [70]; and to a good approximation the probability distribution of the order parameter at the first-order transition could be described by the sum of the Gaussians representing the two coexisting states in the finite system. For the temperature driven first-order transition in the q-state Potts model a similar theoretical development could be used, but a factor of "q" needed to be included in the Gaussian representing the q-fold degenerate ordered state [71]. Monte Carlo simulations of the $q = 10$ Potts model on $L \times L$ lattices verified this finite-size behavior [72].

As for the first-order phase transition where a continuous symmetry is broken, there are neither theoretical predictions nor good data from simulations regarding the finite-size behavior. A "fruit fly" model is thus necessary to help provide an understanding of this case, and we consider the uniaxially anisotropic, three-dimensional ($3D$) Heisenberg antiferromagnet in an external field, H, is exactly such a candidate model. Substantial interest has been shown to this model for a number of decades, mostly are about the phase diagram and ordered structures clarifications and the nature of the multicritical point identification [5, 62–65, 73–77].

Both the SF-to-P and the AF-to-P phase transitions are of second-order. They belong to the XY and the Ising universality classes, respectively. However, the phase transition between the AF and SF phases is of the first-order. The point $T = T_b$ where the three phases meet was determined to be a bicritical point in the three-dimensional (3D) Heisenberg universality class. Fig. 4.2 shows the corresponding phase diagram in the neighboring area of the bicritical point. In earlier work, the spin-flop boundary for the anisotropic Heisenberg antiferromagnet in an applied field was located rather precisely [5, 65], thus this model is actually a fertile testing ground for the study of finite-size effects at a first-order transition where a continuous symmetry is broken.

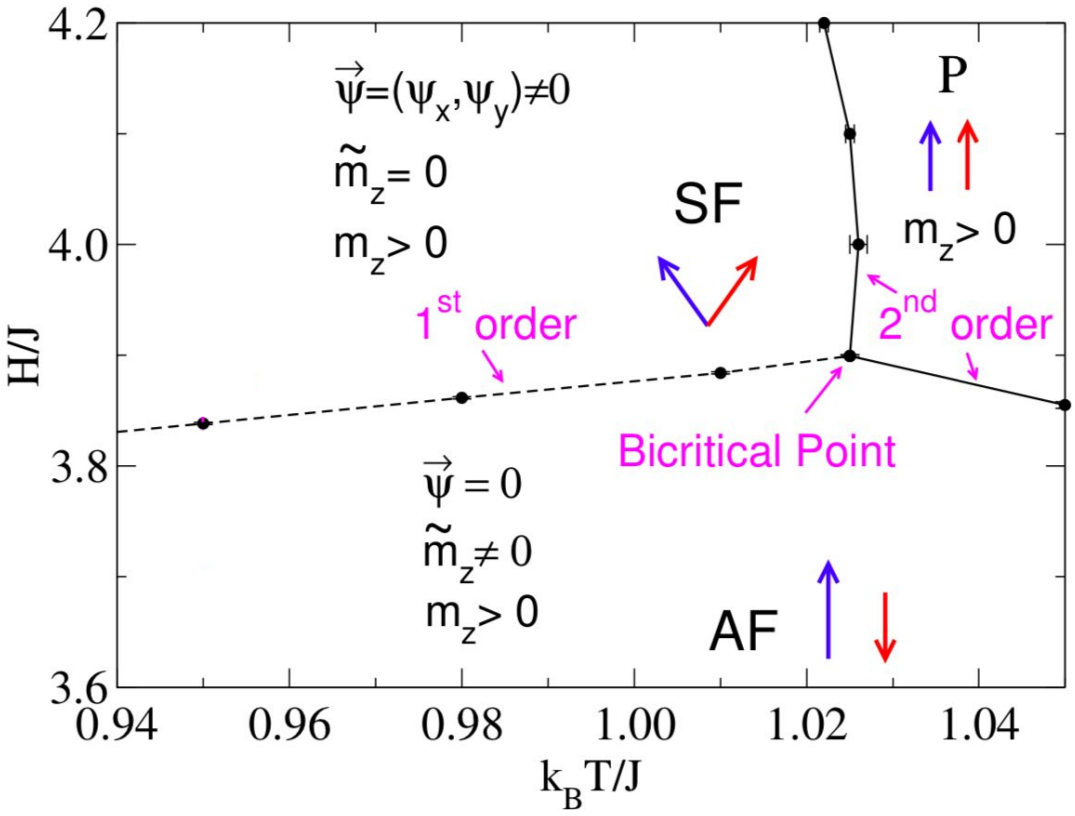

Figure 4.2: Phase diagram for the 3D anisotropic Heisenberg model in an applied magnetic field, H, near the bicritical point [5]. Both the temperature, T, (k_B is Boltzmann's constant) and the external field are normalized by the exchange constant J. The order parameter for the antiferromagnetic phase is $\tilde{m}_z$ and for the spin-flop phase is $\vec{\psi}$. The z-component of the uniform magnetization is m_z.

The phase diagram near the bicritical point in the temperature T and field H plane is shown in Fig. 4.2, where the meeting point of the three phase transition lines is estimated to be at $k_B T_b/J = 1.025 \pm 0.0025$ and $H_b/J = 3.89 \pm 0.01$ [5, 65]. Note that here we are not concerned with the phase boundaries near the bicritical point but rather shall study the finite-size effects associated with the first-order transition from the AF phase to the SF phase at $T = 0.95J/k_B$, $T = 0.80J/k_B$, and $T = 0.60J/k_B$ at a transition field H^t.

4.3 Sampling methods

For $T = 0.95J/k_B$ two different Monte Carlo methods were used to carry out the simulations, where simple cubic lattices with even values of L and periodic boundary conditions were considered. Simulations for $L \leq 60$ were first performed using a standard Metropolis algorithm [15] with the R1279 shift register random number generator [1]. Runs of length 3×10^7 MCS were performed for all lattice sizes and the number of independent runs ranged from 10 for $L = 30$ to 1035 for $L = 60$. For $L = 60$ Metropolis sampling had great difficulty tunneling between the two states on opposite sides of the spin-flop transitions. Therefore, to ensure that the sampling was truly ergodic for $L = 60$, $L = 80$ and $L = 100$, we implemented multicanonical sampling [17]. Multicanonical simulations were then performed for the entire range of sizes so that results could be compared with those from Metropolis sampling. The multicanonical sampling probability was determined iteratively for each L until the multicanonical probability density $P_{muca}(E)$ of the energy is "flat" enough, see Fig. 4.3. Then runs of length 10^7 MCS were carried out. To determine averages and error bars a total of 100 independent runs were made for $L = 30$ and the number increased with increasing size until 900 independent runs were used for $L = 100$. For smaller lattices, there was agreement between the data generated using the two different sampling methods and the results could be combined for the analysis. For the multicanonical runs the Mersenne Twister random number generator was used [1]. For $T = 0.80J/k_B$ and $T = 0.60J/k_B$, similar multicanonical simulations mentioned above were applied to generate data for $L = 10$ up to $L = 50$ and $L = 10$ up to $L = 40$ respectively.

Histogram reweighting techniques [18] were applied to extract thermodynamic quantities for fields near the values used in the simulations. For the largest lattices, comparisons were made between runs made at adjacent field values and reweighted results to ensure that we were not reweighting beyond the reliable range of fields.

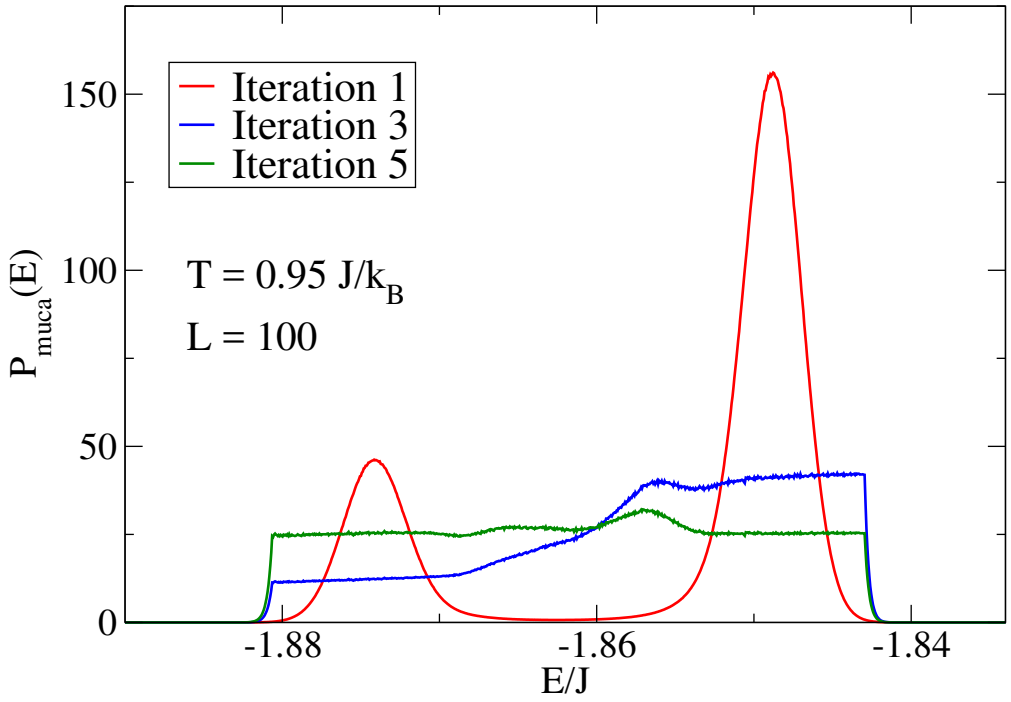

Figure 4.3: Multicanonical probability density $P_{muca}(E)$ of the energy with different iterations for $L = 100$ at $T = 0.95 J/k_B$.

4.4 Theory and quantities to be analyzed

4.4.1 General relations and order parameters

For small enough fields, $H < H^t(T)$, and low temperatures, T, the anisotropic Heisenberg antiferromagnet exhibits Neél-type two-sublattice order on the simple cubic (or other bipartite three-dimensional) lattices. This order is described by the staggered magnetization (with the two interpenetrating sublattices of the $L \times L \times L$ lattice denoted by indices 1 and 2)

$$\tilde{m}_z = \frac{1}{L^3}\Big(\sum_{i\in 1} S_{iz} - \sum_{i\in 2} S_{iz}\Big) \ . \tag{4.2}$$

For $H > 0$ we also expect to have a non-zero uniform magnetization m_z (per spin)

$$m_z = \frac{1}{L^3}\Big(\sum_{i\in 1} S_{iz} + \sum_{i\in 2} S_{iz}\Big) \ . \tag{4.3}$$

At the transition field, $H = H^t(T)$, there is a first-order phase transition to the "spin-flop" phase described by a two-component order parameter involving the transverse spin components

$$\psi_\alpha = \frac{1}{L^3}\Big(\sum_{i\in 1} S_{i\alpha} - \sum_{i\in 2} S_{i\alpha}\Big) \ , \quad \alpha = (x, y) \ . \tag{4.4}$$

Both ψ_x, ψ_y are equivalent and form the components of a vector order parameter $\vec{\psi}$ with XY symmetry. Fig. 4.2 shows the phase diagram near the bicritical point T_b, and Fig. 4.4 describes the schematic variation of the free energy with the magnetic field H (for simplicity, the temperature dependence of $H^t(T)$ is suppressed in Fig. 4.4) along with its derivative $m_{z,\infty} = \langle m_z \rangle_{T,L\to\infty}$ as well as the order parameter $\psi_\infty = \sqrt{\langle \psi_x^2 + \psi_y^2 \rangle_{T,L\to\infty}}$. Henceforth, a subscript "∞" means that we are referring to properties in the thermodynamic limit. Note that the variable $m_{z,\infty}$ is the thermodynamically conjugate variable to the magnetic field, with F being the Gibbs free energy per spin [78],

$$m_{z,\infty} = -(\partial F/\partial H)_T \ . \tag{4.5}$$

Defining the transition field in the thermodynamic limit as H^t, we note that $m_{z,\infty}$ at H^t must jump from $m_{z,\infty}^{AF}$ in the antiferromagnetic phase to a larger value $m_{z,\infty}^{SF}$ in the spin-flop phase. At the transition field the free energies of the two phases are equal, $F = F_t$, and the free energy differences (per spin) in the two phases relative to this value are, to leading order

$$\Delta F_{AF} = (H^t - H) m_{z,\infty}^{AF} \ , \quad H \le H^t \ , \tag{4.6}$$

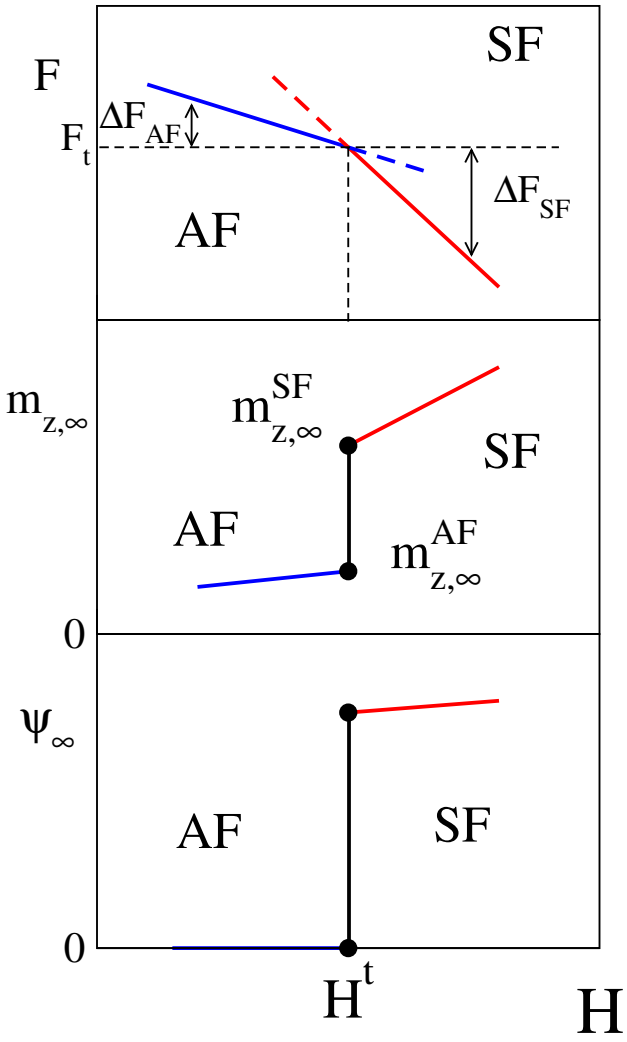

Figure 4.4: Schematic variation of thermodynamic quantities with field H for $T < T_b$: (top) Free energy $F(T, H)$. The absolute magnitude of the free energy differences ΔF_{AF}, ΔF_{SF} in the antiferromagnetic (AF) and spin-flop (SF) phases are relative to the free energy (per spin) at the transition (F_t). Near the transition field H^t these free energy differences vary linearly with H; (middle) Magnetization $m_{z,\infty}$ along the field direction. At H^t a jump occurs from $m^{AF}_{z,\infty}$ (in the thermodynamic limit, $L \to \infty$) in the AF phase to $m^{SF}_{z,\infty}$ in the SF phase. Near H^t the variation of $m_{z,\infty}$ with H is linear; (bottom) Absolute value of the order parameter of the SF phase, ψ_∞. Since the AF-SF transition is first-order, ψ_∞ jumps discontinuously from zero to a non-zero value when $H = H^t$.

$$\Delta F_{SF} = (H^t - H) m_{z,\infty}^{SF} \ , \quad H \geq H^t \ . \tag{4.7}$$

The total free energy difference between phases then becomes (continuing both phases into their metastable region and ignoring the inequalities in Eqs. (4.6), (4.7))

$$\begin{aligned} \Delta F \equiv \Delta F_{SF} - \Delta F_{AF} &= (H - H^t)(m_{z,\infty}^{AF} - m_{z,\infty}^{SF}) \\ &= -(H - H^t)\Delta m, \end{aligned} \tag{4.8}$$

where we have introduced $\Delta m = (m_{z,\infty}^{SF} - m_{z,\infty}^{AF})$ to represent the jump in the magnetization m_z in the thermodynamic limit at the transition (see Fig. 4.4). Note that $\Delta F > 0$ for $H < H^t$ since $m_{z,\infty}^{AF} < m_{z,\infty}^{SF}$.

We can use Eqs. (4.6) - (4.8) to construct the statistical weights of the two phases in a large, but finite, system in a field $H \approx H^t$. The most naive assumption would be $a_{AF} \propto \exp(-\Delta F_{AF} L^3/k_B T)$, $a_{SF} \propto \exp(-\Delta F_{SF} L^3/k_B T)$. However, this assumption, using a common normalization factor, disregards the difference in degeneracy of the two phases. While the AF phase is two-fold degenerate ($n = 1$, one-component order parameter), in the SF phase a continuous (XY-model like) symmetry is broken ($n = 2$, two-component order parameter). How this difference enters in the weights is not obvious, unlike in the simpler case of the thermally driven q-state Potts model [79] with Hamiltonian

$$\mathcal{H} = -J \sum_{\langle i,j \rangle} \sigma_i \sigma_j, \tag{4.9}$$

where $\sigma_i = 1, 2, ..., q$ and a bond is formed between nearest neighbors only if they are in the same state. In the q-state Potts model, the high-temperature phase is non-degenerate and the low-temperature phase is simply q-fold degenerate. There, an extra factor q appears in the weight of the low-temperature phase multiplying the Boltzmann factor. It is unclear (at least to us) what this factor q must be when dealing with a continuous symmetry.

Thus, we introduce an analogous factor q *phenomenologically* to account for the difference in degeneracy between the phases at the coexistence point in the thermodynamic limit ($H = H^t$). As we shall see, in full analogy with the Potts model, this factor leads to shifts of characteristic finite-size induced features (e.g. position of the maximum of the magnetic susceptibility or specific heat, minimum of the various cumulants, etc.). Observing these features in the simulations should provide numerical estimates for this degeneracy factor q for the present problem. In the next subsection we shall advance a hypothesis for the value of q.

We now postulate the "equal weight rule" [71] for the statistical weights of the two phases, i.e. $a_{AF} = \mathcal{N}\exp(-\Delta F_{AF}L^3/k_BT)$ and $a_{SF} = \mathcal{N}q\exp(-\Delta F_{SF}L^3/k_BT)$, with a normalization factor $\mathcal{N}$. Requiring $a_{AF} + a_{SF} = 1$ yields

$$a_{AF} = \exp(\Delta F L^3/k_BT)/[q + \exp(\Delta F L^3/k_BT)] \ , \tag{4.10}$$

$$a_{SF} = q/[q + \exp(\Delta F L^3/k_BT)] \ , \tag{4.11}$$

as expected.

Formally, the factor q can be absorbed by redefining the weights as $a_{AF} = \exp(\Delta F' L^3/k_BT)/[1 + \exp(\Delta F' L^3/k_BT)]$, $a_{SF} = 1/[1 + \exp(\Delta F' L^3/k_BT)]$, with $\Delta F' = \Delta F - (k_BT/L^3)\ln q$. This shows that finite-size induced shifts of characteristic features scaling as $(k_BT/L^3)\ln q$ will occur.

4.4.2 Order parameter distribution at the transition in the thermodynamic limit

Before going further, we use the transition between the disordered and ordered states for the q-state Potts model to provide some insight about the effective degeneracy factor for the

AF to SF transition in the anisotropic Heisenberg model. For the q-state Potts model in the thermodynamic limit exactly at the transition temperature, the probability distribution of the order parameter $P(\vec{\psi})$ is simply the sum of $q+1$ weighted delta functions,

$$P(\vec{\psi}) = \delta(\vec{\psi}) + \sum_{k=1}^{q} \delta(\vec{\psi} - \vec{\psi}_k), \tag{4.12}$$

where the $\vec{\psi}_k$ are the discrete values of the order parameter in the ordered phase [80]. The first term on the right hand side of Eq. (4.12) represents the disordered phase and the second term represents the (degenerate) ordered phase. In the current case a similar expression holds except that the $\vec{\psi}$ are continuous. We, therefore, conjecture that

$$P(\tilde{m}_z, \psi) = [\delta(\tilde{m}_z - \tilde{m}_{z,\infty}) + \delta(\tilde{m}_z + \tilde{m}_{z,\infty})]\delta(\psi) + \int_0^{2\pi} \delta(\tilde{m}_z)\delta(\psi - \psi_\infty)d\phi, \tag{4.13}$$

where the order parameter $\vec{\psi}$ is written in terms of the magnitude ψ and angle ϕ in the (ψ_x, ψ_y) plane, and we have integrated over ϕ. The index "∞" indicates that the thermodynamic limit was taken first and then $H \to H^t$. Since there is no dependence upon ϕ, the integral gives 2π. Integration over $\tilde{m}_z$ then yields

$$P(\psi) = 2\delta(\psi) + 2\pi\delta(\psi - \psi_\infty) \ , \tag{4.14}$$

or the relative weight of the two phases is simply π!

Eq. (4.13) merely indicates that in the thermodynamic limit and for $H = H^t$, we have phase coexistence between pure AF phases ($\tilde{m}_z = \pm\tilde{m}_{z,\infty}$, $\vec{\psi} = 0$) and pure SF phases ($\vec{\psi} = (\psi_\infty, \phi)$, in polar coordinates in the (ψ_x, ψ_y)-plane, and $\tilde{m}_z = 0$). The distribution of the order parameters is simply characterized by the appropriate Dirac delta-functions. Making contact with formulation of Eqs. (4.10), (4.11), where the relative weights of the two phases at H^t was denoted by the phenomenological parameter q, we find that the joint

(unnormalized) distribution of the order parameters $\tilde{m}_z$, $\psi = |\vec{\psi}|$ becomes

$$P_\infty(\tilde{m}_z, \psi) = [\delta(\tilde{m}_z - \tilde{m}_{z,\infty}) + \delta(\tilde{m}_z + \tilde{m}_{z,\infty})]\delta(\psi) + 2q\delta(\tilde{m}_z)\delta(\psi - \psi_\infty) \ . \tag{4.15}$$

The normalization constant for this distribution is

$$\mathcal{N}_\infty = \int_{-1}^{+1} d\tilde{m}_z \int_{0^-}^{1} d\psi P_\infty(\tilde{m}_z, \psi) = 2 + 2q \ . \tag{4.16}$$

From Eqs. (4.15), (4.16) we can easily obtain the moments and cumulants of both order parameters (the notation $\langle \cdots \rangle_\infty$ means that an average over both phases at the transition point in the thermodynamic limit is taken)

$$\langle |\vec{\psi}| \rangle_\infty = \psi_\infty q/(1+q) \ , \tag{4.17}$$

$$\langle \psi^2 \rangle_\infty = \psi_\infty^2 q/(1+q) \ , \tag{4.18}$$

$$\langle \psi^4 \rangle_\infty = \psi_\infty^4 q/(1+q) \ , \tag{4.19}$$

$$\langle |\tilde{m}_z| \rangle_\infty = \tilde{m}_{z,\infty}/(1+q) \ , \tag{4.20}$$

$$\langle \tilde{m}_z^2 \rangle_\infty = \tilde{m}_{z,\infty}^2/(1+q) \ , \tag{4.21}$$

$$\langle \tilde{m}_z^4 \rangle_\infty = \tilde{m}_{z,\infty}^4/(1+q) \ . \tag{4.22}$$

Hence, the fourth-order cumulants simply become

$$U_\infty^{xy} \equiv 1 - \langle \psi^4 \rangle_\infty / [3\langle \psi^2 \rangle_\infty^2] = 1 - \frac{1+q}{3q} \ , \tag{4.23}$$

and

$$U_\infty^{z} \equiv 1 - \langle \tilde{m}_z^4 \rangle_\infty / [3\langle \tilde{m}_z^2 \rangle_\infty^2] = (2-q)/3 \ . \tag{4.24}$$

Of course, these results do not invoke the assumption of Gaussian distributions of the order parameters for finite L {see Eqs. (4.25), (4.29), (4.30) or a similar assumption for $P_L(\tilde{m}_z)$ that will be used below}. Thus, Eqs. (4.17)-(4.24) are not affected in any way by deviations from Gaussian distributions in the wings of the actual distributions for finite L.

Eqs. (4.17)-(4.24) permit stringent tests of this theory by simulations using the following recipe: Suppose an accurate estimate of H^t is known from suitable finite-size extrapolation (e.g. using Eq. (4.28); other choices will be given below). Then, a very large system can be simulated (for which no transitions between the pure phases occur for very long runs) right at $H = H^t$, once starting in the AF phase and once starting in the SF phase, to obtain very accurate estimates of $\tilde{m}_{z,\infty}$ and of ψ_∞. From the distributions of the order parameters in these pure phases, accurate estimates of the staggered susceptibilities $\tilde{\chi}_{xy}^{AF}$, $\tilde{\chi}_{xy}^{SF}$, $\tilde{\chi}_{zz}^{AF}$, and $\tilde{\chi}_{zz}^{SF}$, can also be extracted. Extrapolations of the estimates for $\langle|\vec{\psi}|\rangle_L$, $\langle|\tilde{m}_z|\rangle_L$, $\langle\psi^2\rangle_L$, $\langle\tilde{m}_z^2\rangle_L$, U_L^{xy} and U_L^z at $H = H^t$ towards $L = \infty$ should provide estimates for the factors $q/(1+q)$ and $1/(1+q)$ in Eqs. (4.17), (4.20) as well as the cumulants, Eqs. (4.23), (4.24).

Eqs. (4.17) - (4.24) also define (almost) universal intersection points when we study analogous averages for finite L as a function of the field H. $\langle|\vec{\psi}|\rangle_L$, $\langle|\tilde{m}_z|\rangle_L$, $\langle\psi^2\rangle_L$, $\langle\tilde{m}_z^2\rangle_L$, U_L^{xy} and U_L^z are all analytic functions of H, saturating for $|\Delta F|L^3/k_BT >> 1$. For the cumulants these saturation values are trivial, e.g. $U^z(H < H^t) = 1$, $U^z(H > H^t) = 0$. But we will show later that they will agree with Eqs. (4.17) - (4.24), up to corrections of order $L^{-\frac{3}{2}}$ or L^{-3} for $|\Delta F|L^3/k_BT = 0$. Unlike second-order transitions for which only cumulants, e.g. U_L^{xy} and U_L^z, have unique intersection points at the transition, for this first-order transition both the individual moments and the cumulants exhibit this feature of common intersection points at $H = H^t$.

4.4.3 Two-gaussian approximation for the magnetization distribution

While Eqs. (4.17)-(4.24) describe the behavior of the system when we first set $H = H^t$ and then take the limit $L \to \infty$, it is also of great interest to explore the leading corrections to the limiting behavior when L is large but finite.

Following general considerations of statistical physics [81], in pure phases, for large but finite size systems, we expect Gaussian distributions for the densities of extensive thermodynamic variables rather than δ-functions. A simple case to consider is the uniform magnetization for which Gaussian distributions for the (scalar) quantity m_z in the two phases would give a distribution,

$$P_L(m_z) \propto \frac{a_{AF}}{\sqrt{\chi_{zz}^{AF}}} \exp\Big\{ - \frac{[m_z - (m_{z,\infty}^{AF} + \chi_{zz}^{AF}\Delta H)]^2}{2k_B T \chi_{zz}^{AF}/L^3} \Big\} + \frac{a_{SF}}{\sqrt{\chi_{zz}^{SF}}} \exp\Big\{ - \frac{[m_z - (m_{z,\infty}^{SF} + \chi_{zz}^{SF}\Delta H)]^2}{2k_B T \chi_{zz}^{SF}/L^3} \Big\} \ , \tag{4.25}$$

where

$$\Delta H \equiv H - H^t, \tag{4.26}$$

χ_{zz}^{AF}, χ_{zz}^{SF} are the susceptibilities at $H = H^t$ in the two phases, and a_{AF}, a_{SF} are the statistical weights of the two phases at $H = H^t$.

Invoking the analogy of these equations to the case of the Potts model energy distribution [cf. Eq. (IV.21) in Ref. [1]], we conclude that the susceptibility peak should scale as

$$\chi_{zz}^{\max} \approx \frac{\chi_{zz}^{AF} + \chi_{zz}^{SF}}{2} + \frac{(\Delta m)^2 L^3}{4k_B T} \tag{4.27}$$

in analogy to the specific heat of the Potts model. Note that the location of this maximal magnetization fluctuation (i.e. susceptibility of the z-component of the uniform magnetiza-

tion) occurs when the two weights are equal, i.e. $a_{AF} = a_{SF} = 1/2$. This condition readily yields $q \exp(-\Delta F L^3/k_B T) = 1$, i.e. $\Delta F/k_B T = \ln q/L^3$, or

$$(H^{\max} - H^t)/k_B T = -[\Delta m L^3]^{-1} \ln q \ . \tag{4.28}$$

Since $m^{AF}_{z,\infty} < m^{SF}_{z,\infty}$, the position of the susceptibility maximum relative to the transition point must shift to smaller fields, $H^{\max} < H^t$, and scale with size like L^{-3}.

The susceptibility at the transition point H^t is smaller by a factor $4q/(1+q)^2$ than $\chi^{\max}_{zz}$ for $L \to \infty$.

One important caveat, however, is that for the weight for the low temperature phase of the Potts model, the factor q reflecting the degeneracy of the ordered phase is known. In contrast, here the value of a similar factor representing the difference in degeneracies of the spin-flop and antiferromagnetic phases is *unknown* unless we rely on the hypothesis of Eq. (4.14) that $q = \pi$.

4.4.4 SF phase order parameter distribution

We next consider the distribution of the SF order parameter $\vec{\psi}$. For $H < H^t$, i.e. in the AF phase, there is simply a Gaussian distribution about zero since the transverse spin component is disordered,

$$P^{AF}_L(\vec{\psi}) = \mathcal{N} \exp\Big(- \frac{\vec{\psi}^{\,2}}{2 k_B T \tilde{\chi}^{AF}_{xy}/L^3} \Big) \ , \tag{4.29}$$

where we introduced the notation $\tilde{\chi}_{\alpha\beta}$ for the tensor of staggered susceptibilities, and $\tilde{\chi}^{AF}_{xy}$ stands for the xy-components of the staggered susceptibility in the AF phase.

The order parameter distribution in the SF phase is more interesting,

$$P^{SF}_L(\vec{\psi}) = \mathcal{N} \exp\Big[- \frac{(\vec{\psi}^{\,2} - \psi^2_\infty)^2}{8 \psi^2_\infty k_B T \tilde{\chi}^{SF}_{xy}/L^3} \Big] \ , \tag{4.30}$$

where now $\tilde{\chi}_{xy}^{SF}$ denotes the xy-component of the staggered susceptibility in the spin-flop phase. Note that a 4th order polynomial in $\vec{\psi}$ is needed in the argument of the exponential function in Eq. (4.30) to bring out the circular symmetry in the (ψ_x, ψ_y)-plane correctly. Near the peak ($|\vec{\psi}| \approx \psi_\infty$) the argument of the exponential reduces to the expected quadratic form, i.e. $-(\psi - \psi_\infty)^2/(2k_BT\tilde{\chi}_{xy}^{SF}/L^3)$.

In the vicinity of the transition field, H^t, we now make the standard superposition approximation,

$$\langle\psi^2\rangle_L = a_{AF}\langle\psi^2\rangle_{AF} + (1 - a_{AF})\langle\psi^2\rangle_{SF}, \tag{4.31}$$

$$\langle\psi^4\rangle_L = a_{AF}\langle\psi^4\rangle_{AF} + (1 - a_{AF})\langle\psi^4\rangle_{SF}, \tag{4.32}$$

where

$$a_{AF} = 1/[1 + q\exp(\mathcal{Z})] \ , \tag{4.33}$$

where we have written $\mathcal{Z} = -\Delta F L^3/k_BT$, and the moments $\langle\cdots\rangle_{AF}$, $\langle\cdots\rangle_{SF}$ refer to the order parameter distributions in the "pure" AF and SF phases respectively.

Of course, we could repeat the calculation of Eqs. (4.15)-(4.24) for finite L, replacing the delta functions by the appropriate Gaussian distributions, e.g. Eqs. (4.29) and (4.30).

From the general result for the fourth-order cumulant, we immediately conclude that for H^t, U_L^{xy} differs from $U^*{=}U_\infty^{xy}$ only by corrections of order L^{-3} and

$$U_L^{xy}\ |_{H^t} = 1 - \frac{1+q}{3q}\Big[1 + (\frac{4k_BT\tilde{\chi}_{xy}^{SF}}{\psi_\infty^2} - \frac{4k_BT\tilde{\chi}_{xy}^{AF}}{q\psi_\infty^2})\frac{1}{L^3}\Big] \ . \tag{4.34}$$

If we use the value $q = \pi$, we find that $U_\infty^{xy} \approx 0.56056$.

Taking the derivative of the expression for the cumulant to find the minimum, and writing $Y{=}q\exp(\mathcal{Z})$, we find the location of the minimum is given by $Y_{\min} \approx 2k_BT\tilde{\chi}_{xy}^{AF}/((\psi_\infty)^2L^3)$.

Hence

$$H_{\min} = H^t - \frac{k_B T[\ln q - \ln Y_{\min}]}{\Delta m L^3} \quad . \tag{4.35}$$

Thus, the shift in the location of the minimum scales as L^{-3}, but the leading term is actually $\ln L/L^3$. At the minimum, the value of U_L^{xy} is

$$U_{L,\min}^{xy} \approx const - \frac{\psi_\infty^2 L^3}{24 k_B T \tilde{\chi}_{xy}^{AF}}, \tag{4.36}$$

which means that $U_{L,\min}^{xy}$ approaches $-\infty$ proportional to $-L^3$ as L approaches infinity.

In addition, Eq. (4.29) can be used to evaluate the 4th-order cumulant in the following way. The normalization factor $\mathcal{N}$ is given by,

$$\begin{aligned} \mathcal{N}^{-1} &= 2\pi \int_0^\infty \psi d\psi \exp(-\psi^2 L^3/(2k_B T \tilde{\chi}_{xy}^{AF})) \\ &= 2k_B T \pi \tilde{\chi}_{xy}^{AF}/L^3 \quad . \end{aligned} \tag{4.37}$$

This factor $\mathcal{N}$ is only applicable for the order parameter moments of a "pure" AF phase and has nothing to do with the normalization factor used to derive Eq. (4.10). The second moment is simply

$$\langle \psi^2 \rangle_{AF} = 2k_B T \tilde{\chi}_{xy}^{AF}/L^3 \tag{4.38}$$

and the fourth moment

$$\langle \psi^4 \rangle_{AF} = 2(2k_B T \tilde{\chi}_{xy}^{AF}/L^3)^2 \quad . \tag{4.39}$$

Hence

$$U_L^{AF} = 1 - \langle \psi^4 \rangle_{AF}/[3\langle \psi^2 \rangle_{AF}^2] = 1/3. \tag{4.40}$$

Note that for a two-component order parameter, a different normalization of U_L would be required for a Gaussian distribution to yield zero in the disordered phase.

In order to obtain the moments of the order parameter of the SF phase using Eq. (4.30), we have to compute the integrals

$$\langle\psi^2\rangle_{SF} = 2\pi\mathcal{N}\int_0^\infty \psi d\psi\, \psi^2 \exp\Big[-\frac{(\psi^2-\psi_\infty^2)^2 L^3}{8\psi_\infty^2 k_B T\tilde{\chi}_{xy}^{SF}}\Big] \ , \tag{4.41}$$

$$\langle\psi^4\rangle_{SF} = 2\pi\mathcal{N}\int_0^\infty \psi d\psi\psi^4 \exp\Big[-\frac{(\psi^2-\psi_\infty^2)^2 L^3}{8\psi_\infty^2 k_B T\tilde{\chi}_{xy}^{SF}}\Big] \ , \tag{4.42}$$

where the normalization factor $\mathcal{N}$ is given by

$$\begin{aligned}\mathcal{N}^{-1} &= 2\pi\int_0^\infty \psi d\psi \exp\Big[-\frac{(\psi^2-\psi_\infty^2)^2 L^3}{8\psi_\infty^2 k_B T\tilde{\chi}_{xy}^{SF}}\Big] \\ &= 2\psi_\infty\pi\sqrt{2\pi k_B T\tilde{\chi}_{xy}^{SF}}L^{-3/2} \ .\end{aligned} \tag{4.43}$$

Similarly, writing $\psi^2 = x$, we conclude

$$\langle\psi^2\rangle_{SF} = \pi\mathcal{N}\int_0^\infty dx x \ \exp\Big[-\frac{(x-\psi_\infty^2)^2 L^3}{8\psi_\infty^2 k_B T\tilde{\chi}_{xy}^{SF}}\Big] \approx \psi_\infty^2 \tag{4.44}$$

with negligibly small correction. However, a non-trivial correction term arises in the fourth moment,

$$\begin{aligned}\langle\psi^4\rangle_{SF} &= \pi\mathcal{N}\int_0^\infty dx x^2 \ \exp\Big[-\frac{x^2-2x\psi_\infty^2+\psi_\infty^4}{8\psi_\infty^2 k_B T\tilde{\chi}_{xy}^{SF}/L^3}\Big] \\ &\approx \psi_\infty^4 + 4\psi_\infty^2 k_B T\tilde{\chi}_{xy}^{SF}/L^3 \ .\end{aligned} \tag{4.45}$$

The ratio U_L in the ordered SF phase hence becomes

$$U_L^{SF} = 1 - \langle\psi^4\rangle_{SF}/(3\langle\psi^2\rangle_{SF}^2) = \frac{2}{3} - \frac{4k_B T\tilde{\chi}_{xy}^{SF}}{3L^3\psi_\infty^2} \ . \tag{4.46}$$

Invoking the superposition approximation of Eq. (4.31)-(4.33) we find that the 4th-order cumulant for the SF order parameter then becomes

$$U_L^{xy} = 1 - \frac{[1+q\exp(\mathcal{Z})][q\exp(\mathcal{Z})[1+4k_BT\tilde{\chi}_{xy}^{SF}/(\psi_\infty^2 L^3)]+2(2k_BT\tilde{\chi}_{xy}^{AF}/(\psi_\infty^2 L^3))^2]}{3[q\exp(\mathcal{Z})+2k_BT\tilde{\chi}_{xy}^{AF}/(\psi_\infty^2 L^3)]^2} \ . \tag{4.47}$$

The weighted averages of the order parameter moment in the AF and SF phases becomes

$$\langle|\vec{\psi}|\rangle_L = \left\{\psi_\infty\left[1-k_BT\tilde{\chi}_{xy}^{SF}/(2L^3\psi_\infty^2)\right]q\exp(\mathcal{Z})+\sqrt{\pi k_BT\tilde{\chi}_{xy}^{AF}/(2L^3)}\right\}\Big/[1+q\exp(\mathcal{Z})] \ . \tag{4.48}$$

4.4.5 AF phase order parameter distribution

The AF order parameter distribution for this one-component order parameter in the AF phase is a double Gaussian, analogous to Eq. (4.25),

$$\begin{aligned} P_L^{AF}(\tilde{m}_z) \propto & \exp\left[-(\tilde{m}_z-\tilde{m}_{z,\infty})^2L^3/(2k_BT\tilde{\chi}_{zz}^{AF})\right] \\ & +\exp\left[-(\tilde{m}_z+\tilde{m}_{z,\infty})^2L^3/(2k_BT\tilde{\chi}_{zz}^{AF})\right], \end{aligned} \tag{4.49}$$

whereas in the SF phase it is given by a single Gaussian

$$P_L^{SF}(\tilde{m}_z) = \sqrt{L^3/(2\pi k_BT\tilde{\chi}_{zz}^{SF})}\exp\Big[-\tilde{m}_z^2L^3/(2k_BT\tilde{\chi}_{zz}^{SF})\Big]. \tag{4.50}$$

From these distribution and superposition approximations analogous to Eqs. (4.31) - (4.33), it is straightforward to calculate the various moments of the staggered magnetization and the cumulant. Then, at the transition, the fixed point value of the cumulant is

$$U_L^z\,|_{H^t} = \frac{2-q}{3}+\frac{1+q}{3}\Big[\frac{2qk_BT\tilde{\chi}_{zz}^{SF}}{\tilde{m}_{z,\infty}^2}-4\frac{k_BT\tilde{\chi}_{zz}^{AF}}{\tilde{m}_{z,\infty}^2}\Big]\frac{1}{L^3} \ . \tag{4.51}$$

This means that, as expected, the asymptotic value of the cumulant coincides with the result from the treatment using delta function distributions. Again the correction to this result is small, of order L^{-3}; and choosing $q = \pi$, we find the fixed point value of the cumulant is $U_*^z \approx -0.38$.

Using Eqs. (4.49) and (4.50) we can straightforwardly obtain the second and fourth moments $\langle \tilde{m}_z^2 \rangle, \langle \tilde{m}_z^4 \rangle$ in both phases and apply a superposition approximation. The resulting cumulant is

$$U_L^z = 1 - \frac{[1 + q\exp(\mathcal{Z})]}{3} \frac{1 + \frac{6k_BT\tilde{\chi}_{zz}^{AF}}{\tilde{m}_{z,\infty}^2 L^3} + \frac{3(k_BT\tilde{\chi}_{zz}^{AF})^2}{(\tilde{m}_{z,\infty}^2 L^3)^2} + \frac{3q\exp(\mathcal{Z})(k_BT\tilde{\chi}_{zz}^{SF})^2}{(\tilde{m}_{z,\infty}^2 L^3)^2)}}{[1 + k_BT\tilde{\chi}_{zz}^{AF}/(\tilde{m}_{z,\infty}^2 L^3) + q\exp(\mathcal{Z})k_BT\tilde{\chi}_{zz}^{SF}/(\tilde{m}_{z,\infty}^2 L^3)]^2} \quad . \tag{4.52}$$

The weighted averages of the order parameter moment in the AF and SF phases becomes

$$\langle |\tilde{m}_z| \rangle_L = \frac{\tilde{m}_{z,\infty}}{[1 + q\exp(\mathcal{Z})]} + \frac{q\exp(\mathcal{Z})\sqrt{2k_BT\tilde{\chi}_{zz}^{SF}/(\pi L^3)}}{[1 + q\exp(\mathcal{Z})]} \quad . \tag{4.53}$$

4.4.6 Maximum slope of the cumulant and cumulant crossings

We have shown that the cumulant at $H = H^t$ is of order unity but reaches a deep minimum (of order $-L^3$ for $L \to \infty$) at a point where $H^t - H \propto L^{-3}$ (on the AF side of the spin-flop transition when the cumulant of the SF-order parameter is considered). In order to achieve a variation of order L^{+3} in an interval of order L^{-3}, the maximum slope of the cumulant in the interval between the minimum and the crossing point must then be of order L^6. On the other hand, we can easily show that the slope of the cumulant right at $H = H^t$ still is only of order L^3, namely

$$k_BT \left. \frac{dU_L^{xy}}{dH} \right|_{H^t} = \frac{1}{3q} \Delta m L^3 \quad . \tag{4.54}$$

Thus, significant curvature should appear in the plot of U_L^{xy} vs. H near H^t, since the slope first increases from zero at the cumulant minimum to a value of order L^6 and then decreases

to a value of order L^3 at $H = H^t$. The location of the intersection point, which corresponds to a cumulant value of order unity, hence must be very close to H^t ($|H^{\rm cross} - H^t| \propto L^{-6}$) also. On a scale of $H - H^t$ of order L^{-3} (the regime over which the variable $\mathcal{Z}$ exhibits a significant variation) differences in cumulant intersections of order L^{-6} are completely negligible. Consequently, the spread of the cumulant intersections is very small, although in a strict sense there is no unique cumulant crossing point. Two cumulants for linear dimensions L and $L' = L + \delta$ that differ slightly ($\delta \approx 0$) can be shown to cross for $H^{\rm cross}$ given by

$$\frac{H^{\rm cross} - H^t}{k_B T} \Delta m = \frac{1+q}{q} \Big[4 k_B T \tilde{\chi}^{AF}_{xy} / \psi^2_\infty - 4 q k_B T \tilde{\chi}^{SF}_{xy} / \psi^2_\infty \Big] L^{-6} \ . \tag{4.55}$$

This equation is derived by a Taylor expansion of $U_{L+\delta}$ simultaneously in the small variables $H - H^t$ and δ / L. This result verifies the above argument that the scale for the shift of the cumulant crossing is negligibly small in comparison with that for the shift of the cumulant minimum. The shift of the intersection point thus scales as the square of the inverse volume, while the regime over which the transition is spread out is given by

$$\Delta \mathcal{Z} = 1 \ , \quad \Delta H / k_B T = 1 / [\Delta m L^3] \ . \tag{4.56}$$

The situation is analogous to the case of the (temperature driven) transition in the Potts model, cf. Vollmayr *et al.* [82]. As in the latter case, and unlike the simple, field driven first-order transition of an Ising ferromagnet below T_c, there is no "equal height rule" of the order parameter distribution at the transition. Eqs. (4.29), (4.37) show that the peak height at $\vec{\psi} = 0$ scales proportional to the volume, L^3, while the height of the "rim" $|\vec{\psi}| = \psi_\infty$ only scales like the square root of the volume, $L^{3/2}$, cf. Eqs. (13), (14), and (23) of Vollmayr *et al.* [82].

Useful information can be readily extracted about the mean square order parameter $\langle \psi^2 \rangle$ as a function of the field H near the transition field H^t.

The superposition approximation (Eqs. (4.31), (4.32)) readily shows that $\langle\psi^2\rangle$ is described by a simple scaling function of $\mathcal{Z}$, namely

$$\langle\psi^2\rangle/\psi_\infty^2 = [b + q\exp(\mathcal{Z})]/[1 + q\exp(\mathcal{Z})], \tag{4.57}$$

where we have introduced the abbreviation

$$b = (2k_BT\tilde{\chi}_{xy}^{AF})/(\psi_\infty^2 L^3) \ . \tag{4.58}$$

Note that the quantities ψ_∞, $\tilde{\chi}_{xy}^{AF}$ (and Δm which is needed to convert the scale of $H - H^t$ to $\mathcal{Z}$) can be estimated directly from simulations. For runs of modest length for very large systems precisely at $H = H^t$, transitions between the phases can be avoided due to metastability. Starting in the AF and SF states respectively will permit measurements in the pure phases. (H^t is already known with high precision). For the correct choice of q, all choices of (sufficiently large) L should then lead to perfect collapse on a master curve, Eq. (4.57), that is explicitly predicted.

The value of the order parameter at the location of the maximum slope is

$$\langle\psi^2\rangle = \frac{1}{2}\psi_\infty^2 + \frac{k_BT\tilde{\chi}_{xy}^{AF}}{\psi_\infty^2 L^3}, \tag{4.59}$$

which is *independent* of the value of "q". Since ψ_∞ and $\tilde{\chi}_{xy}^{AF}$ can be measured independently, we have a non-trivial test of the double Gaussian approximation. The value of the slope at the transition field $H = H^t$ is

$$\left.\frac{d\langle\psi^2\rangle}{d(H/k_BT)}\right|_{H^t} = \Delta m L^3 \frac{q}{(1+q)^2}(1 - \frac{2k_BT\tilde{\chi}_{xy}^{AF}}{\psi_\infty^2 L^3})\psi_\infty^2 \ . \tag{4.60}$$

We also note that for $H = H^t$, i.e. $\mathcal{Z} = 0$, Eq. (4.57) predicts $\langle\psi^2\rangle/\psi_\infty^2 = (b+q)/(1+q) \approx q/(1+q)$, as expected from Eq. (4.18). When $\langle\psi^2\rangle/\psi_\infty^2$ is plotted vs H, all curves for large L will intersect for $H = H^t$ at this value.

4.4.7 Staggered susceptibility maxima

In the absence of symmetry breaking staggered fields, the staggered susceptibility components $\tilde{\chi}'_{zz}$ and $\tilde{\chi}'_{xy}$, referring to the z-component $\tilde{m}_z$ and the xy-components $\vec{\psi}$ of the staggered magnetization, are defined as follows

$$k_B T \tilde{\chi}'_{zz} = L^3(\langle \tilde{m}_z^2 \rangle_L - \langle |\tilde{m}_z| \rangle_L^2) \ , \tag{4.61}$$

$$k_B T \tilde{\chi}'_{xy} = L^3(\langle \psi^2 \rangle_L - \langle |\vec{\psi}| \rangle_L^2) \ . \tag{4.62}$$

Note that Eq.(4.61) yields the usual staggered susceptibility in the AF phase, and Eq. (4.62) in the SF phase. Of course, in the phases where no spontaneous order exists, we simply have from the standard fluctuation relations

$$k_B T \tilde{\chi}_{zz} = L^3 \langle \tilde{m}_z^2 \rangle_L \ , \quad SF \,\text{phase} \ , \tag{4.63}$$

$$k_B T \tilde{\chi}_{xy} = L^3 \langle \psi^2 \rangle_L \ , \quad AF \,\text{phase} \ . \tag{4.64}$$

It is well known that a unique expression for the staggered susceptibility in both phases would require consideration of the limit of an applied staggered field (conjugate to the appropriate order parameter) approaching zero after the thermodynamic limit had been taken. This, however, would be quite inconvenient within the context of simulations.

As already discussed above, the moments $\langle \cdots \rangle_L$ are computed from the corresponding moments $\langle \cdots \rangle_{AF}$, $\langle \cdots \rangle_{SF}$ in the pure phases, taking an average with the corresponding

weights a_{AF}, $1-a_{AF}$. For the second moments, this has already been considered above; here we supply the results for the first moments. For the AF phase we find

$$\langle|\tilde{m}_z|\rangle_{AF} \approx \tilde{m}_{z,\infty} \ , \quad \langle\tilde{m}_z^2\rangle_{AF} \approx \tilde{m}_{z,\infty}^2 + k_B T \tilde{\chi}_{zz}^{AF}/L^3 \ , \tag{4.65}$$

which together with Eq. (4.61) yields the correct result $\tilde{\chi}'_{zz} = \tilde{\chi}_{zz}^{AF}$ in the AF phase. For the SF phase we find

$$\langle|\vec{\tilde{\psi}}|\rangle_{SF} \approx \psi_\infty(1 - k_B T \tilde{\chi}_{xy}^{SF}/(2L^3\psi_\infty^2)) \ , \quad \langle\psi^2\rangle_{SF} \approx \psi_\infty^2 \ . \tag{4.66}$$

From Eqs. (4.31), (4.38), (4.44), (4.53), (4.48), (4.49), and (4.50), it is straightforward to obtain the expressions for the staggered susceptibilities $k_B T\tilde{\chi}'_{zz}$, $k_B T\tilde{\chi}'_{xy}$ defined in Eqs. (4.61), (4.62). These expressions show nicely that in the AF phase, i.e. for $\mathcal{Z} \to -\infty$

$$\tilde{\chi}_{zz}^{\prime AF} = \tilde{\chi}_{zz}^{AF} \ , \quad \tilde{\chi}_{xy}^{\prime AF} = 2\tilde{\chi}_{xy}^{AF}\Big(1 - \frac{\pi}{4}\Big) \ . \tag{4.67}$$

Recall that the AF phase plays the role of the disordered phase for the SF order. Likewise,

$$\tilde{\chi}_{zz}^{\prime SF} = \tilde{\chi}_{zz}^{SF}\Big(1 - \frac{2}{\pi}\Big) \ , \quad \tilde{\chi}_{xy}^{\prime SF} = \tilde{\chi}_{xy}^{SF} \ , \tag{4.68}$$

since here the SF phase plays the role of the disordered phase for AF order.

Locating the staggered susceptibility maximum and estimating its height is also an interesting task. Using the abbreviation $q\exp(\mathcal{Z}) = Y$, we find from $d(\langle\tilde{m}_z^2\rangle - \langle|\tilde{m}_z|\rangle^2)/dY = 0$ that the maximum occurs for

$$Y \approx 1 + \left[\frac{2k_B T\tilde{\chi}_{zz}^{SF}}{L^3}\Big(1 - \frac{2}{\pi}\Big) - \frac{2k_B T\tilde{\chi}_{zz}^{AF}}{L^3}\right] \Big/ \left(\tilde{m}_{z,\infty}^2 - 2\sqrt{\frac{2k_B T\tilde{\chi}_{zz}^{SF}}{\pi L^3}}\right) \approx 1 \ , \tag{4.69}$$

and its height is

$$k_B T \tilde{\chi}_{zz}^{',\max} \cong \frac{L^3 \tilde{m}_{z,\infty}^2}{4} \left(1 - 2\sqrt{\frac{2 k_B T \tilde{\chi}_{zz}^{SF}}{\pi L^3 \tilde{m}_{z,\infty}^2}} \right) \quad . \tag{4.70}$$

This means that the leading correction is reduced by a factor of order $L^{-3/2}$. We also note that exactly at $H = H^t$ (i.e., $Y = q$), $\tilde{\chi}'_{zz}/\tilde{\chi}^{',\max}_{zz} = 4q/(1+q)^2 \approx 0.733$ (if we assume $q = \pi$). Estimation of this ratio offers yet another route to test the value of q.

The scaling function for $\tilde{\chi}^{'}_{xy}$ is given by

$$k_B T \tilde{\chi}^{'}_{xy} = L^3 (AY^2 + BY + C)/(1+Y)^2, \tag{4.71}$$

where the expressions A, B, C are given (to the necessary order in inverse powers of L) by

$$A = k_B T \tilde{\chi}_{xy}^{SF}/L^3, \tag{4.72}$$

$$B = \psi_\infty^2 - 2\psi_\infty \sqrt{\pi k_B T \tilde{\chi}_{xy}^{AF}/(2L^3)}, \tag{4.73}$$

$$C = 2 k_B T \tilde{\chi}_{xy}^{AF} (1 - \pi/4)/L^3. \tag{4.74}$$

So from this expression one can see clearly the "switching" between the two susceptiblities of the "background" phases, which result from this expression when $Y = 0$ or $Y = \infty$, respectively, while

$$Y = Y_{\max} = (B - 2C)/(B - 2A) \approx 1 + (2A - 2C)/B \tag{4.75}$$

yields the susceptibility maximum.

Thus, to leading order all susceptibility maxima occur at the same location, namely for

$$\mathcal{Z} = \mathcal{Z}_{\max} = -\ln q \quad , \quad H^{\max} = H^t + \frac{k_B T \ln q}{\Delta m L^3} \quad , \tag{4.76}$$

but higher order corrections (of order L^{-6}) differ. In both cases, the maximum staggered susceptibility also varies proportional to L^3 but has a $L^{-3/2}$ correction,

$$k_B T \tilde{\chi}'^{,\max}_{xy} \cong L^3 \psi_\infty^2 \frac{1}{4}\Big(1 - \sqrt{2\pi k_B T \tilde{\chi}^{AF}_{xy}/(\psi_\infty^2 L^3)}\Big) \ , \tag{4.77}$$

and $\tilde{\chi}'^{,\max}_{zz}$ is given by Eq. (4.70). Here, too, $\tilde{\chi}'_{xy}$ for $H = H^t$ is smaller than $\tilde{\chi}'^{,\max}_{xy}$ by the same factor $4q/(1+q)^2$ as quoted above.

We now turn to the divergence of the susceptibility $\tilde{\chi}^{SF}_{xy}$ as $L \to \infty$: Fisher and Privman [83] predicted for isotropic, n-component magnets that $k_B T \tilde{\chi}_{xy} = \langle \psi^2 \rangle L^3 = L^3 \psi_\infty^2/n +$ const $L^2(n-1)/(n+2)$ while Chen and Landau [84] predicted $\langle \psi^2 \rangle L^3 = L^3 \psi_\infty^2/n +$ const $L^2(n-1)/n$ (for $n = 3$). Thus, the leading correction is of order $1/L$ (rather than L^{-3}, as found in Eq. (4.66)). Fisher and Privman predict that $L^3(\langle \psi^2 \rangle - \langle |\vec{\psi}| \rangle^2)$ varies proportional to $(n-1)L$ rather than being the finite constant obtained here. It would be interesting to test these predictions (based on spin wave theory) using suitable numerical results for the present model, but this is a task that must be left for future work.

4.5 Limitations of the phenomenological theory

At this point, we comment on an important distinction between the order parameter cumulant intersection for first-order transitions and for second-order transitions. At second-order transitions, for $L \to \infty$ corrections to scaling can be ignored and the cumulant is a regular function of the variable $\mathcal{Z} = tL^{1/\nu}$, ν being the correlation length critical exponent and t being the reduced distance from the transition point. The slope of the cumulant dU_L/dt at the transition point hence is of the same order as the inverse shift $L^{-1/\nu}$ of the susceptibility maximum.

The L^{-3} correction to Eqs. (4.34), (4.51) is simply a "correction to finite-size scaling" for first-order transitions, analogous to those that appear in finite-size scaling at second-order transitions. However, in the latter case these corrections involve a second, non-trivial exponent (different from $1/\nu$), while here the inverse volume L^{-3} is the only variable that leads to correction terms in the finite-size scaling description. Since the resolution of the numerical data is insufficient to quantitatively resolve any of these correction term effects, they shall not be discussed further. We also note that further terms are expected due to corrections to the Gaussian approximation for the probability distribution, e.g. the result $U_L^{AF} = 1/3$ for the cumulant of the XY-order parameter in the AF phase is also expected to have a $1/L^3$ correction (related to higher order correlation functions) which has been ignored here but seems rather relevant numerically. In addition, corrections of order $\exp(-L/\xi)$, where ξ is the appropriate correlation length of the AF and/or SF order, have been ignored. These become important, however, if H^t is sufficiently close to the bicritical point.

There is another, rather different limitation to our phenomenological treatment: The superposition approximation, Eqs. (4.31) and (4.32), which assumes that the total order parameter distribution $P_L(\psi_x, \psi_y)$ is a superposition of Gaussians for the AF phase (centered at $\psi_x = 0$, $\psi_y = 0$) and of the ordered phase (centered at $\psi_x^2 + \psi_y^2 = \psi_\infty^2$) with appropriate weights, is not accurate away from the peaks of the distribution. The same applies for the distribution of the order parameter $P(\tilde{m}_z)$ for the AF phase. In the latter case, the problem is well understood: far from the transition ($H \ll H^t$) the distribution $P(\tilde{m}_z)$ near $\tilde{m}_z = 0$ is dominated by "slab configurations" where a domain with $\tilde{m}_z = -\tilde{m}_z^{\rm spont}$ is separated by two domain walls ("antiphase domain boundaries") from domains with $\tilde{m}_z = +\tilde{m}_z^{\rm spont}$ (where $\tilde{m}_z^{\rm spont}$ is the value of the order parameter where $P(\tilde{m}_z)$ has its peak). Thus, $P(\tilde{m}_z)$ is not controlled by a Boltzmann factor containing the volume L^3, but rather by the surface area L^2,

$$P(\tilde{m}_z \approx 0) \propto \exp(-2L^2 f_{\rm int}/k_B T) \ , \tag{4.78}$$

with $f_{\rm int}$ the interfacial excess free energy per unit area (interfacial tension). This "slab configuration" with two planar interfaces is compatible with the periodic boundary conditions, of course.

For a two-component order parameter, the "antiphase domain boundaries" are spread out over the entire volume, and the "phase" of the order parameter gradually rotates from zero to 2π as the system is traversed. Thus, for $H \gg H^t$, we have

$$P(\psi_x \approx 0,\, \psi_y \approx 0) \propto \exp(-2L\Gamma/k_BT), \tag{4.79}$$

where Γ is essentially the "helicity modulus" [85]. For H near H^t, however, mixed phase configurations will occur with states $m_z \approx m_z^{AF}$, $\tilde{m}_z \approx \pm\tilde{m}_{z,\infty}$, $\psi \approx 0$ coexisting with states $m_z \approx m_z^{SF}$, $\tilde{m}_z \approx 0$, $|\vec{\psi}| \approx \psi_\infty$ with comparable weights. Such mixed phases require more complex "interfaces" in which the order parameters "interpolate" between their coexisting phase values. The generalization of Eqs. (4.78) and (4.79) is unknown.

Chapter 5

Results: spin-flop transition in the 3D XXZ Heisenberg antiferromagnet

5.1 Transition field H^t

The simulations were performed below the bicritical point T_b at fixed temperature $T = 0.95J/k_B$, $T = 0.80J/k_B$ and $T = 0.60J/k_B$, and we varied the external field H in order to determine the phase transition from AF to SF. When not shown, error bars in the figures showing our results are smaller than the size of the symbols.

The probability densities of the energy E per site are shown at the transition field H_L^t for different lattice sizes L in Fig. 5.1. For each size we chose the finite-size transition field to be located at the point at which the (symmetric) peaks in the probability density for the energy were of equal heights.

As for $T = 0.95J/k_B$ (Fig. 5.1(a)), while the dip between the peaks was rather shallow for $L = 40$, it rapidly became quite deep for increasing values of L in agreement with the predictions of Binder [86] and Lee and Kosterlitz [87] for a first-order transition.

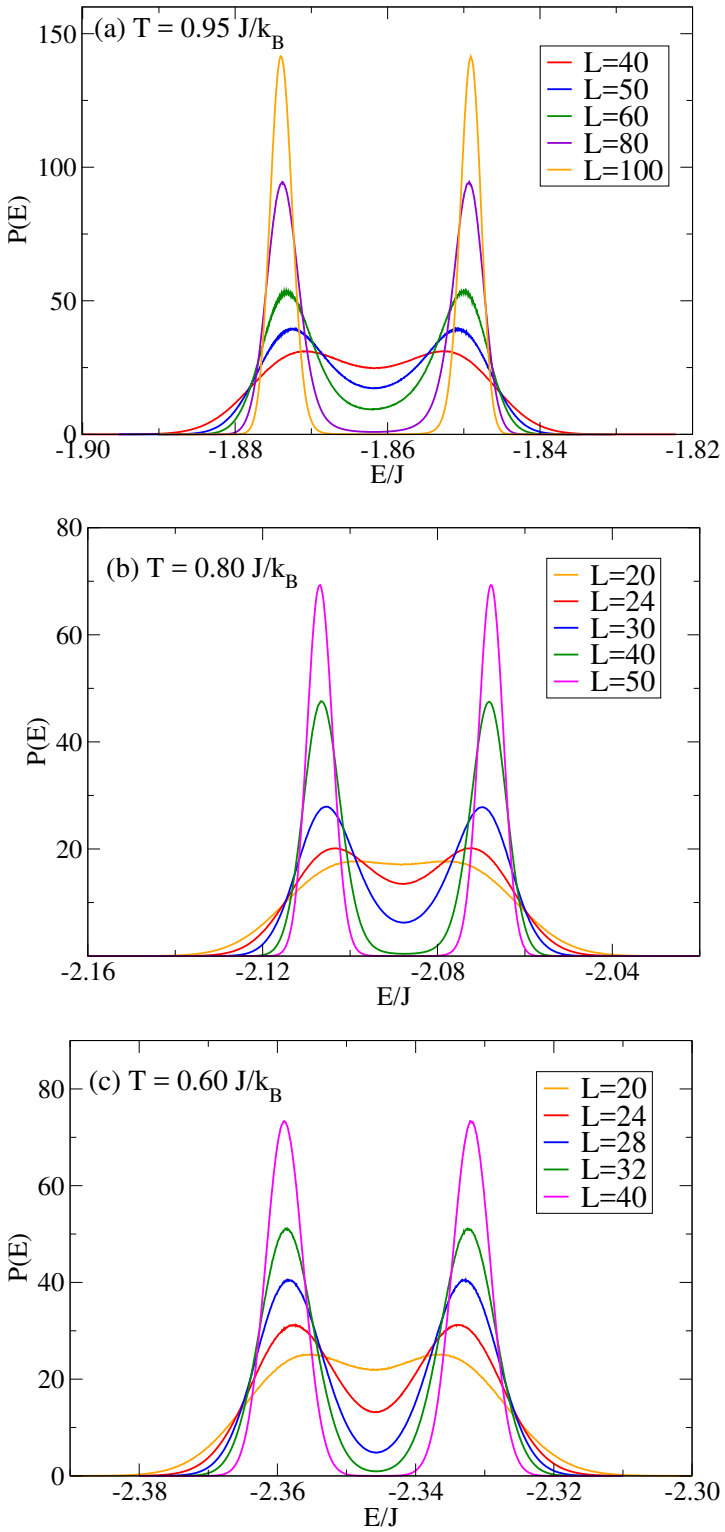

Figure 5.1: Probability density of the energy at the transition field H_L^t for different lattice sizes L at (a) $T = 0.95J/k_B$, (b) $T = 0.80J/k_B$, (c) $T = 0.60J/k_B$.

For smaller values of L the probability density was almost flat, and the resultant thermodynamic properties showed such substantial finite-size rounding that it was not possible to extract useful information about the asymptotic behavior. For this reason, we shall not show raw data for $L < 40$ for $T = 0.95J/k_B$ in the figures that follow. Similarly, Fig. 5.1(b) and Fig. 5.1(c) show a double-peak graph of the probability density of the energy at $T = 0.80J/k_B$ and $T = 0.60J/k_B$, but data for $L < 20$ are not shown for both figures.

The probability densities of the z-component for the magnetization m_z per site at $T = 0.95J/k_B$ are shown at the transition field for different lattice sizes L in Fig. 5.2(a). For each size we chose the finite-size transition field to be located at the same point at which the (symmetric) peaks in the probability distribution for the energy were of equal heights. These data show that the distributions of m_z contain two clear, asymmetric peaks of different heights; moreover, these data cannot be described solely by the sum of two Gaussians. Recall that the minimum between the two peaks represents phase coexistence inside the simulation box with one slab in a state $|\tilde{m}_z| \approx \tilde{m}_{z,\infty}, \psi = 0$ and the other slab having $|\tilde{m}_z| \approx 0, |\vec{\psi}| = \psi_\infty$ with the two slabs separated by a complex interface connected by the periodic boundary conditions. If we "separate" the distributions into two peaks by choosing the minimum probability as the separation point, we can measure the "weight" of each peak by numerically integrating the probability under each peak. To a high degree of precision, the peaks for each of the lattices sizes, L, then have equal weights. Likewise, Fig. 5.2(b) shows the probability density of the z-component for the magnetization m_z per site at $T = 0.80J/k_B$.

The values of the transition field for each lattice size, L, as determined by the equal heights of the two peaks in the probability densities for the energy, are plotted in Fig. 5.3. Fig. 5.3(a) describes the case for $T = 0.95J/k_B$. It shows very nicely that the variation is linear with L^{-3} for $L \geq 40$. The estimated transition field in the thermodynamic limit is $H^t/J = 3.83830(5)$. Also shown are the positions of the minima of the 4th-order cumulant of the energy. These agree almost perfectly with the values extracted from the locations of the

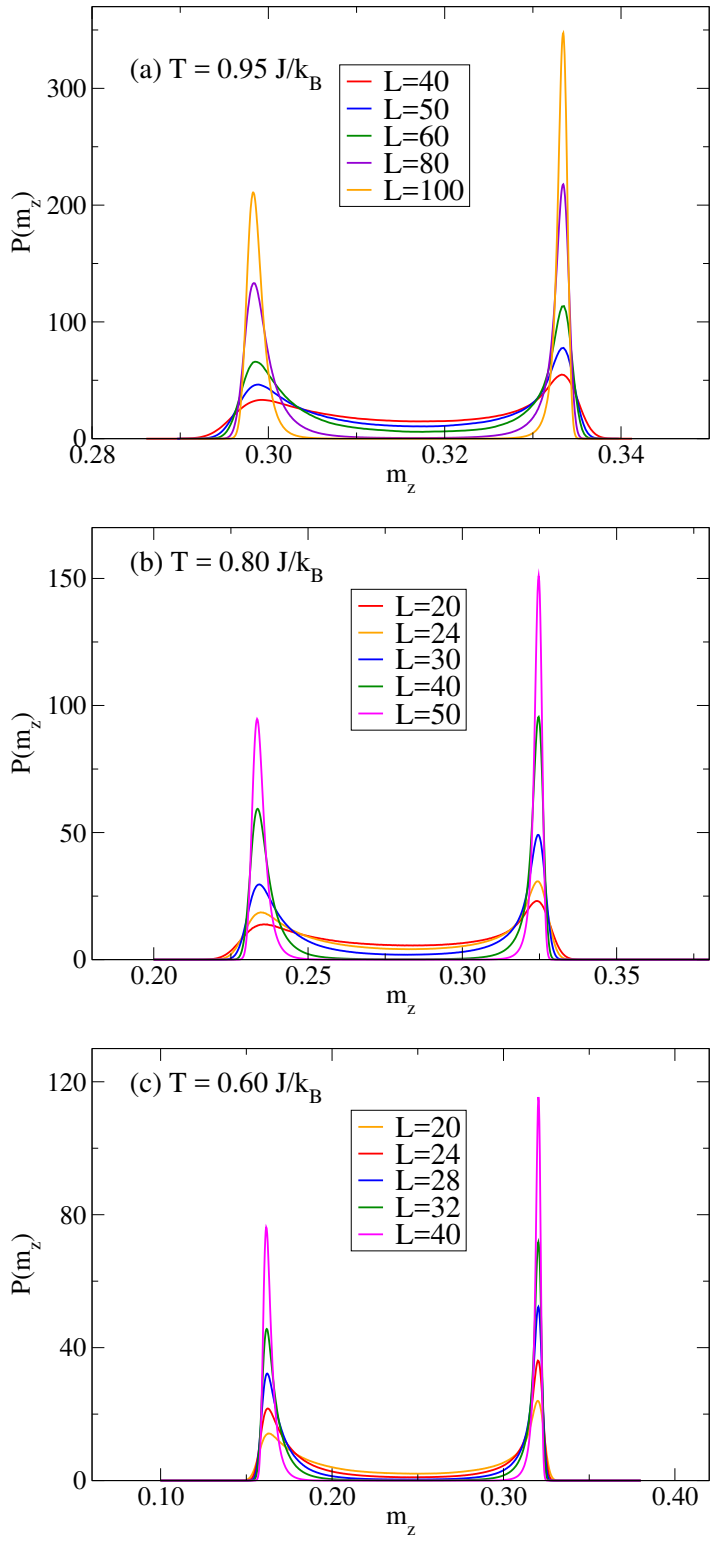

Figure 5.2: Probability density of the z-component of the magnetization at the transition field H_L^t for different lattice sizes L. (a) $T = 0.95J/k_B$, (b) $T = 0.80J/k_B$, (c) $T = 0.60J/k_B$.

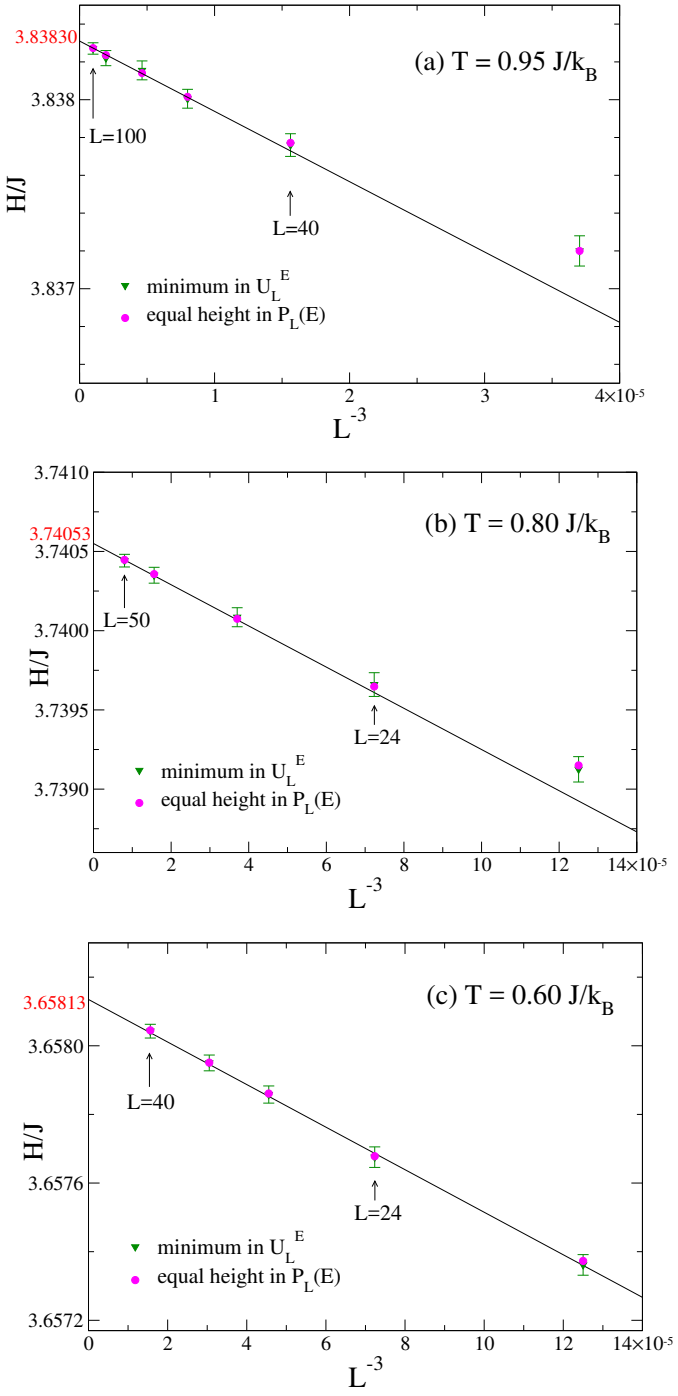

Figure 5.3: Extrapolation of the locations of the transition fields determined from the "equal height" rule for peaks in the probability distribution of the energy and from the minimum of the 4th order cumulant of the energy vs the inverse volume of the system. (a) $T = 0.95J/k_B$, (b) $T = 0.80J/k_B$, (c) $T = 0.60J/k_B$.

peaks in the probability distributions. Likewise, Fig. 5.3(b) corresponds to $T = 0.80J/k_B$, and the transition field in the thermodynamic limit is estimated $H^t/J = 3.74053(6)$, by performing an extrapolation to $L = \infty$ for $L \geq 30$. Fig. 5.3(c) is for $T = 0.60J/k_B$. Extrapolating to $L = \infty$ for $L \geq 24$, the transition field is $H^t/J = 3.65813(5)$.

From the extrapolation of the peak positions of $P_L(m_z)$ (and of the values of the first moments $\int dm_z m_z P_L(m_z)$ for each peak) we can estimate $m_{z,\infty}^{AF}$ and $m_{z,\infty}^{SF}$ and hence obtain the difference $\Delta m = m_{z,\infty}^{SF} - m_{z,\infty}^{AF} \approx 0.0352(4)$ for $T = 0.95J/k_B$, $\Delta m \approx 0.092(1)$ for $T = 0.80J/k_B$, and $\Delta m \approx 0.159(1)$ for $T = 0.60J/k_B$. Since the factor $\Delta m L^3$ exceeds $k_B T/J$ by a factor from about 10^3 to 1.8×10^4 when L varies from $L = 30$ to $L = 80$ at $T = 0.95J/k_B$, it is plausible that H^t can be located with excellent precision, as shown in Figs. 5.3 and 5.4. The fact that all extrapolations, using both quantities from the AF phase and from the SF phase, yield the same transition field H^t to very good precision, reinforces the conclusion of Ref. [5] that there is a direct first-order transition between the two phases with no intervening biconical phase.

The variation of the positions of the peaks in the susceptibilities of the uniform magnetization as well as both the z-component of the staggered magnetization and of the SF-order parameter for $T = 0.95J/k_B$, $T = 0.80J/k_B$ and $T = 0.60J/k_B$ are shown in Fig. 5.4. As for $T = 0.95J/k_B$, excluding the values for $L = 30, 40$ as probably being outside the asymptotic region, we fitted the remaining values to obtain an asymptotic value. The positions of all three susceptibilities extrapolate with L^{-3} to a value of $H^t/J = 3.83830(8)$. This is in perfect agreement with the result of the extrapolations presented in Fig. 5.3(a). Using the slope of the susceptibility for m_z and Eq. (4.28) we estimate an effective value $q \approx 3.7$ which is slightly larger than the estimate of π as suggested in Sec. 4.4.2.

For $T = 0.80J/k_B$, extrapolations have been done for $L \geq 30$. And the estimated value for the transition field in the thermodynamic limit is $H^t/J = 3.74054(9)$. A similar estimation for the degeneracy factor is $q \approx 3.6$.

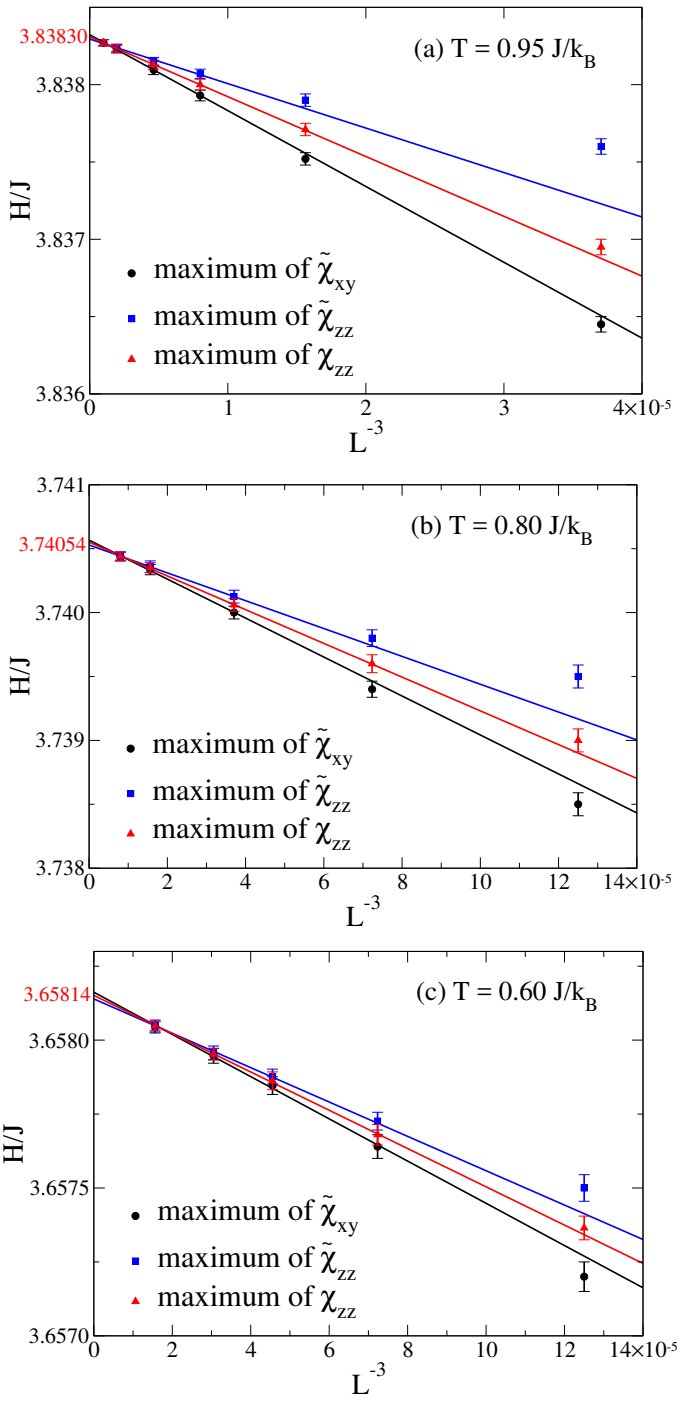

Figure 5.4: Size dependence of the finite-size lattice transition field H_L^t determined from the locations of the maxima of multiple susceptibilities vs L^{-3}. (a) For $T = 0.95J/k_B$, lattice sizes are from $L = 30$ to $L = 100$. The solid lines show extrapolations to $L = \infty$ for $L \geq 50$. (b) For $T = 0.80J/k_B$, lattice sizes are from $L = 20$ to $L = 50$. The solid lines show extrapolations to $L = \infty$ for $L \geq 30$. (c) For $T = 0.60J/k_B$, lattice sizes are from $L = 20$ to $L = 40$. The solid lines show extrapolations to $L = \infty$ for $L \geq 24$.

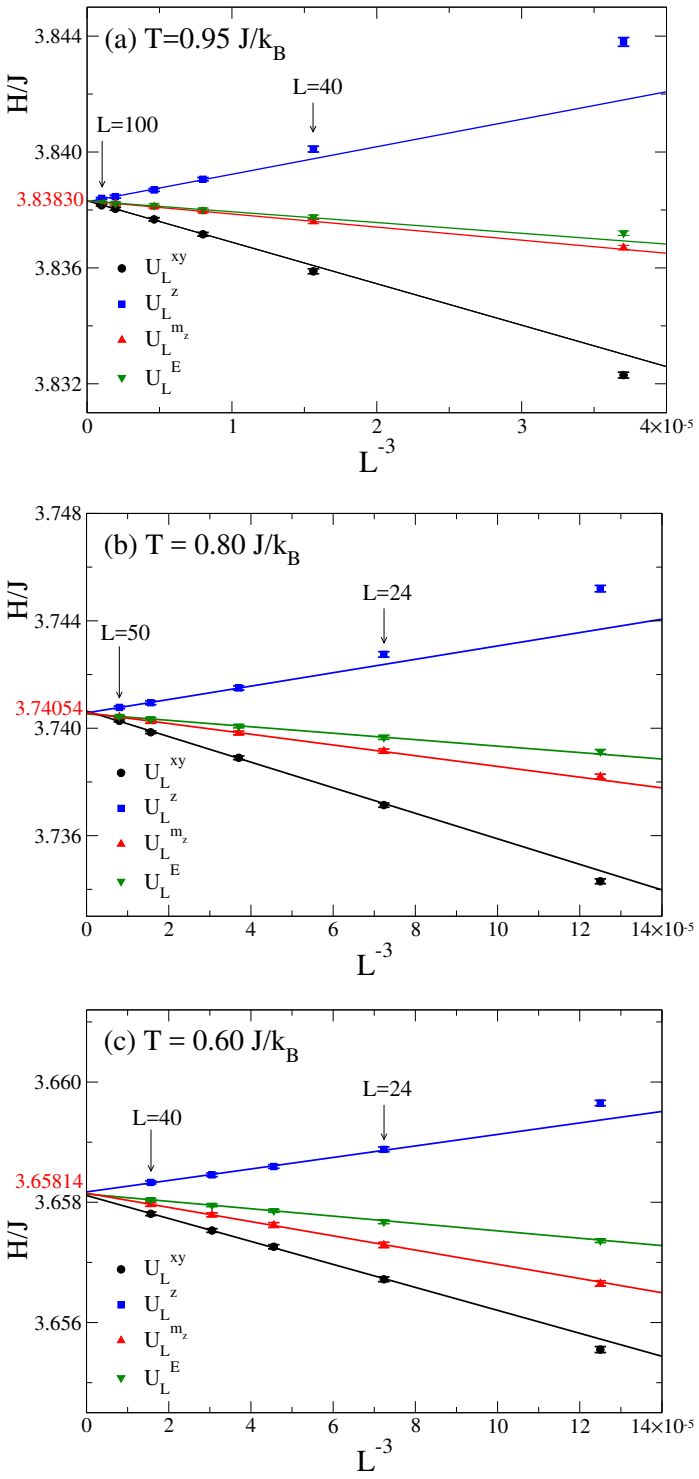

Figure 5.5: Variation of the minima in the 4th order cumulants of the AF and SF order parameters, the energy E and the uniform magnetization m_z for different lattice sizes. (a) $T = 0.95J/k_B$, (b) $T = 0.80J/k_B$, (c) $T = 0.60J/k_B$.

At $T = 0.60J/k_B$, by performing extrapolations to $L = \infty$ for $L \geq 24$, the transition field in the thermodynamic limit is $H^t/J = 3.65814(7)$. The estimated degeneracy factor is $q \approx 3.7$.

The locations of the minima for the cumulants of both order parameters as well as those of the energy and the uniform magnetization m_z extrapolated to the thermodynamic limit are also shown in Fig. 5.5 vs the inverse volume, L^{-3}. (The variation of multiple cumulants will be discussed in Sec. 5.2.) Based on Fig. 5.5(a) for $T = 0.95J/k_B$, the observed variation with lattice size agrees with the predictions of our simple double Gaussian theory and, again, we find a common intersection point of $H^t/J = 3.83830(7)$. The asymptotic size regime, however, appears to begin only for $L \geq 40$. The observation that the depth of the minima decreases very strongly with increasing L is compatible with a scaling as $\approx -L^3$ as observed in the Potts model [82]. A similar figure for $T = 0.80J/k_B$ is shown in Fig. 5.5(b), where extrapolations are for data $L \geq 30$. The transition field at $L = \infty$ is estimated to be $H^t/J = 3.74054(8)$. At $T = 0.60J/k_B$ (Fig. 5.5(c)), by performing extrapolations for data $L \geq 24$, the transition field in the thermodynamic limit is $H^t/J = 3.65814(7)$.

By using the Clausius-Clapeyron relation, the slope dH^t/dT of the coexistence curve in the H-T phase diagram is given by [6],

$$dH^t/dT = \Delta E/(T\Delta m), \tag{5.1}$$

where ΔE is the latent heat and Δm is the uniform magnetization change of the phase transition. Table 5.1 shows the estimates of the slope dH^t/dT at different temperature ($T = 0.95J/k_B$, $0.80J/k_B$, $0.60J/k_B$) by using the Clausius-Clapeyron relation. As T decreases, ΔE first increases then decreases, while Δm monotonically increases. With Eq. (5.1), the estimated slope dH^t/dT monotonically decreases as T decreases.

Table 5.1: Estimates for the latent heat ΔE, the uniform magnetization change of the phase transition Δm, and the slope dH^t/dT of the coexistence curve in the H-T phase diagram by using the Clausius-Clapeyron relation and the one by using a B-spline interpolation at different temperature ($T = 0.95J/k_B$, $0.80J/k_B$, $0.60J/k_B$).

$T/(J/k_B)$	ΔE	Δm	dH^t/dT (Eq. (5.1))	dH^t/dT (interpolation)
0.95	0.0250(7)	0.0352(4)	0.75(2)	0.78(3)
0.80	0.039(1)	0.092(1)	0.53(2)	0.54(2)
0.60	0.0271(8)	0.159(1)	0.28(1)	0.29(2)

At $T = 0$, the transition field between SF and AF is $H^t/J = 3.6$ [62]. By applying a B-spline interpolation, we can also estimate the slope dH^t/dT, as shown in Table 5.1. The values of slope dH^t/dT from the Clausius-Clapeyron relation and those from the interpolation agree with each other. Fig. 5.6 shows the H-T phase diagram for the 3D anisotropic Heisenberg model in an external field, where the dashed curve is a B-spline interpolation.

5.2 Fourth-order cumulants

The behavior of the fourth-order cumulant of the z-component of the magnetization, m_z, seen in Fig. 5.7, shows a clear minimum for each lattice size which sharpens and moves towards larger fields as the lattice size increases at $T = 0.95J/k_B$, $T = 0.80J/k_B$ and $T = 0.60J/k_B$. With increasing L the value of the minimum decreases.

The fourth-order cumulant of the energy, seen in Fig. 5.8 also shows a single minimum that sharpens and moves slowly towards higher fields and becomes deeper as the lattice size increases.

In Figs. 5.9 - 5.11 we show the variation of the fourth-order cumulant of the z-component of the order parameter with field at $T = 0.95J/k_B$, $T = 0.80J/k_B$, and $T = 0.60J/k_B$

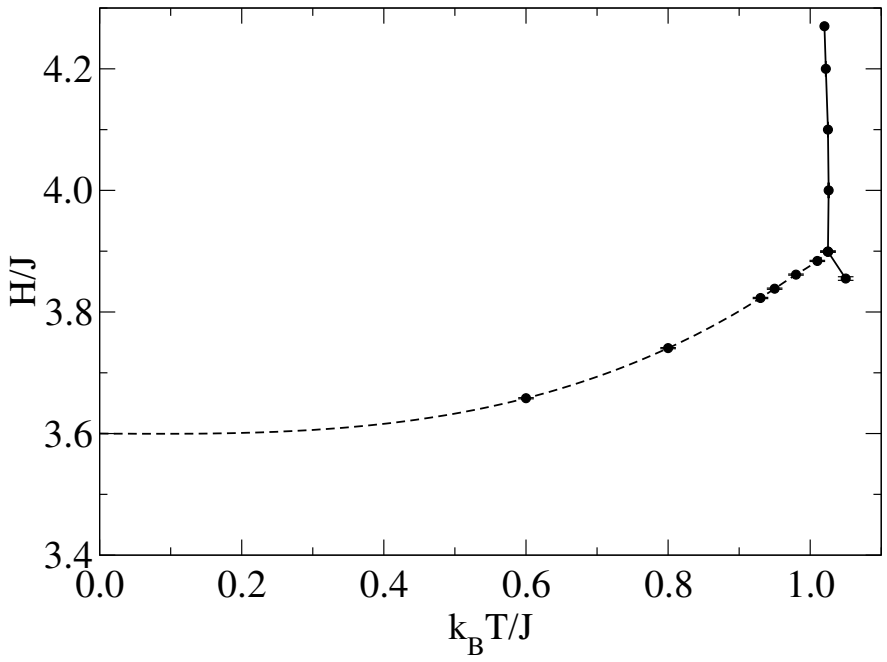

Figure 5.6: Phase diagram for the 3D anisotropic Heisenberg model in an external field, where the dashed curve is a B-spline interpolation.

respectively. As the lattice size increases the crossing points move systematically towards slightly larger fields and the values of the cumulant at the crossing points decrease. In fact, the reduction in the value of U_L^z at the crossing seems to accelerate and there is no indication of convergence for the range of lattice sizes studied so from these data alone we cannot tell if the prediction from our simple phenomenological theory is verified. However, in Sec. 5.4 we give a tentative interpretation of this behavior in terms of crossover behavior between critical behavior dominated by the bicritical point (prevailing for small L) towards first-order finite-size behavior.

Data for the fourth-order cumulant of the xy-component of the order parameter at $T = 0.95J/k_B$, $T = 0.80J/k_B$, and $T = 0.60J/k_B$ respectively, shown in Fig. 5.12 - 5.14, reveal similar behavior except that the minimum occurs at fields lower than the field of the crossing point and moves towards higher fields as the size increases. As for three temperatures, the

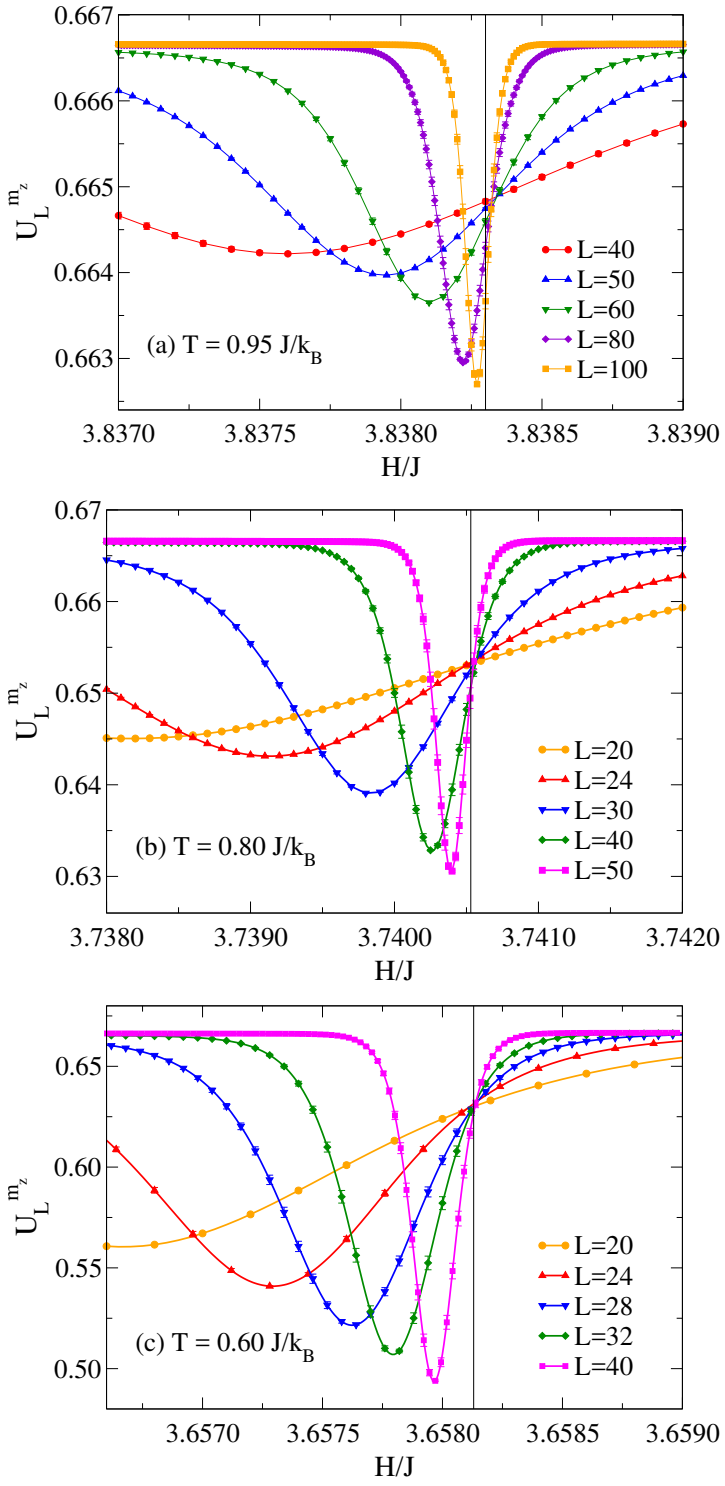

Figure 5.7: Variation of the fourth-order cumulant of the z-component of the magnetization vs H for different lattice sizes. The vertical line shows the asymptotic H^t. (a) $T = 0.95J/k_B$, (b) $T = 0.80J/k_B$, (c) $T = 0.60J/k_B$.

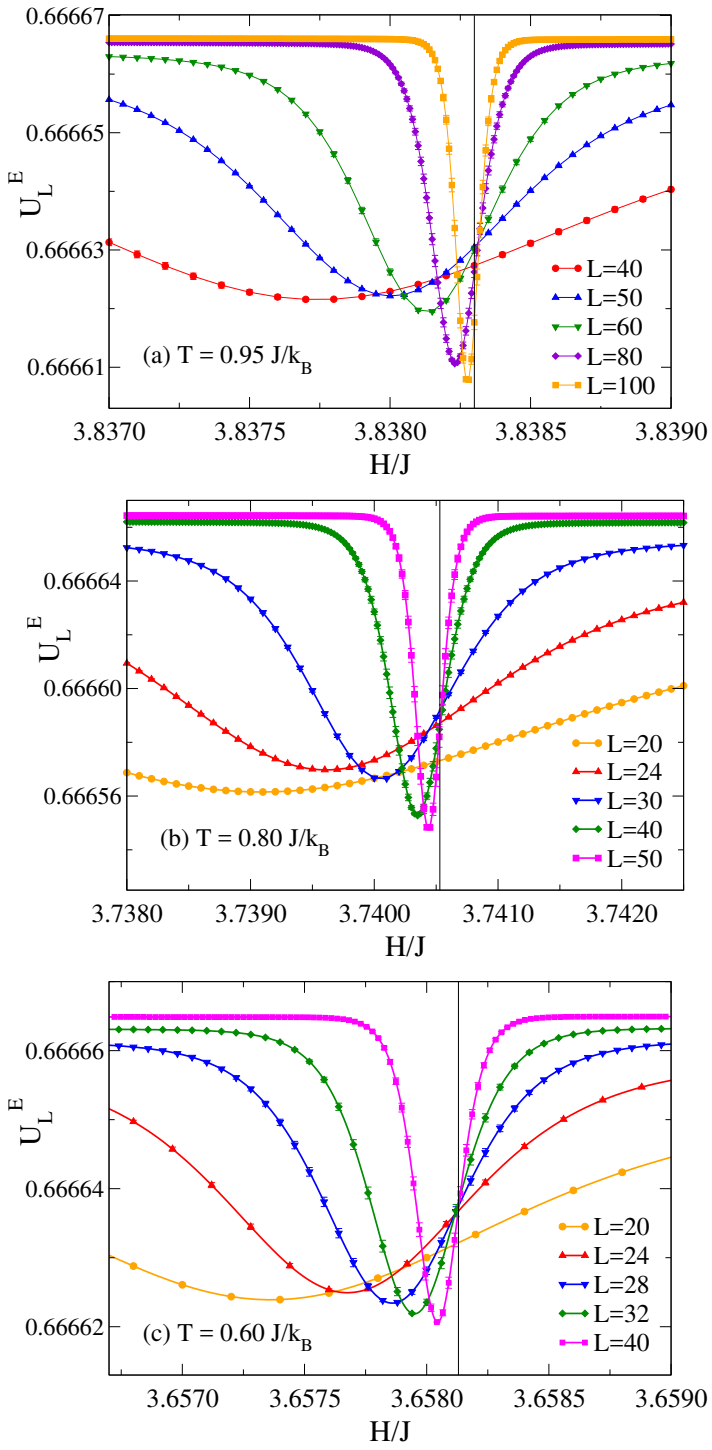

Figure 5.8: Variations of the fourth-order cumulant of the energy for different lattice sizes vs applied field H. (a) $T = 0.95J/k_B$, (b) $T = 0.80J/k_B$, (c) $T = 0.60J/k_B$.

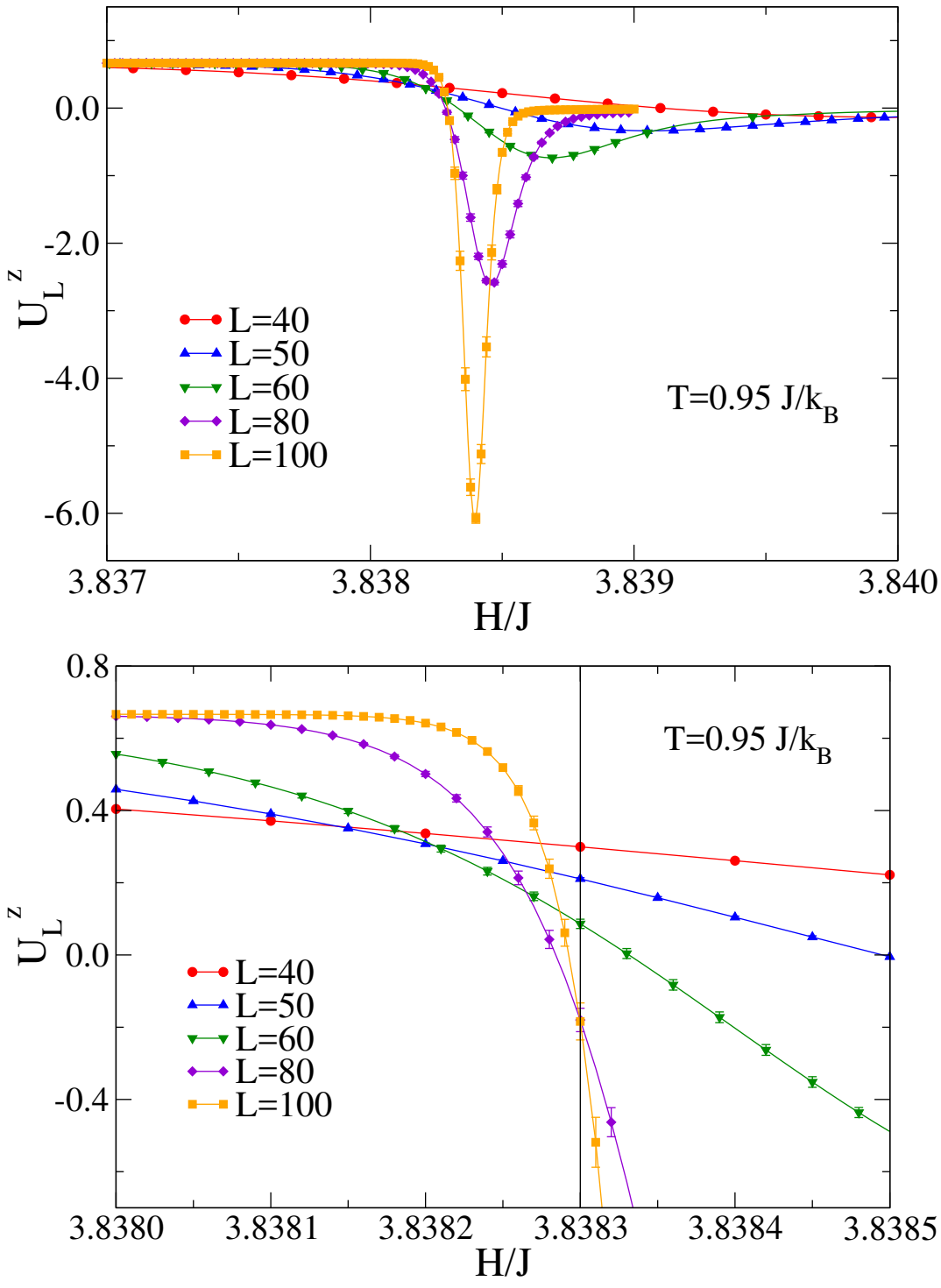

Figure 5.9: Top: Variation of the fourth-order cumulant of the AF order parameter vs magnetic field for different lattice sizes at $T = 0.95J/k_B$. Bottom: Same as above but on a finer scale.

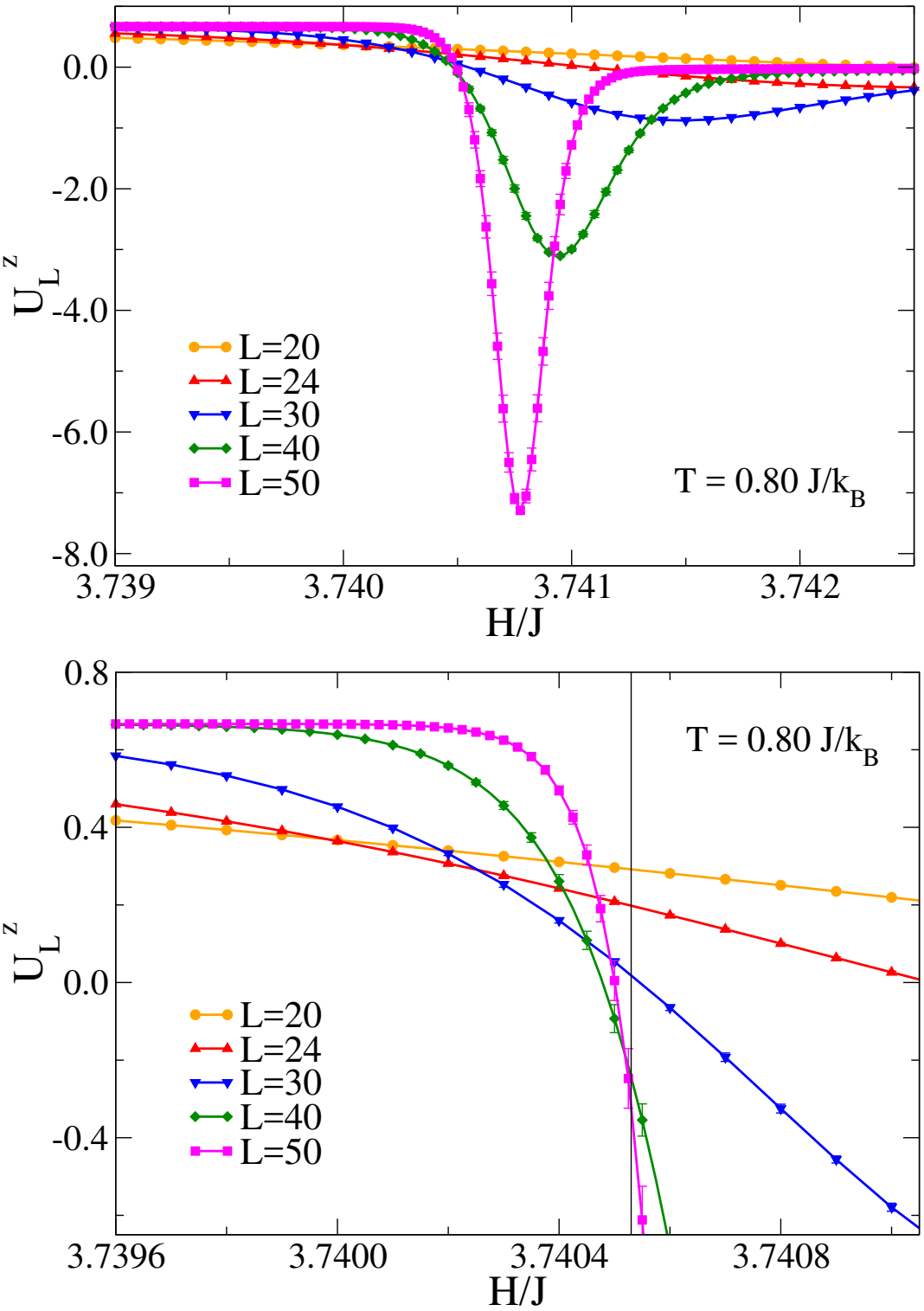

Figure 5.10: Top: Variation of the fourth-order cumulant of the AF order parameter vs magnetic field for different lattice sizes at $T = 0.80J/k_B$. Bottom: Same as above but on a finer scale.

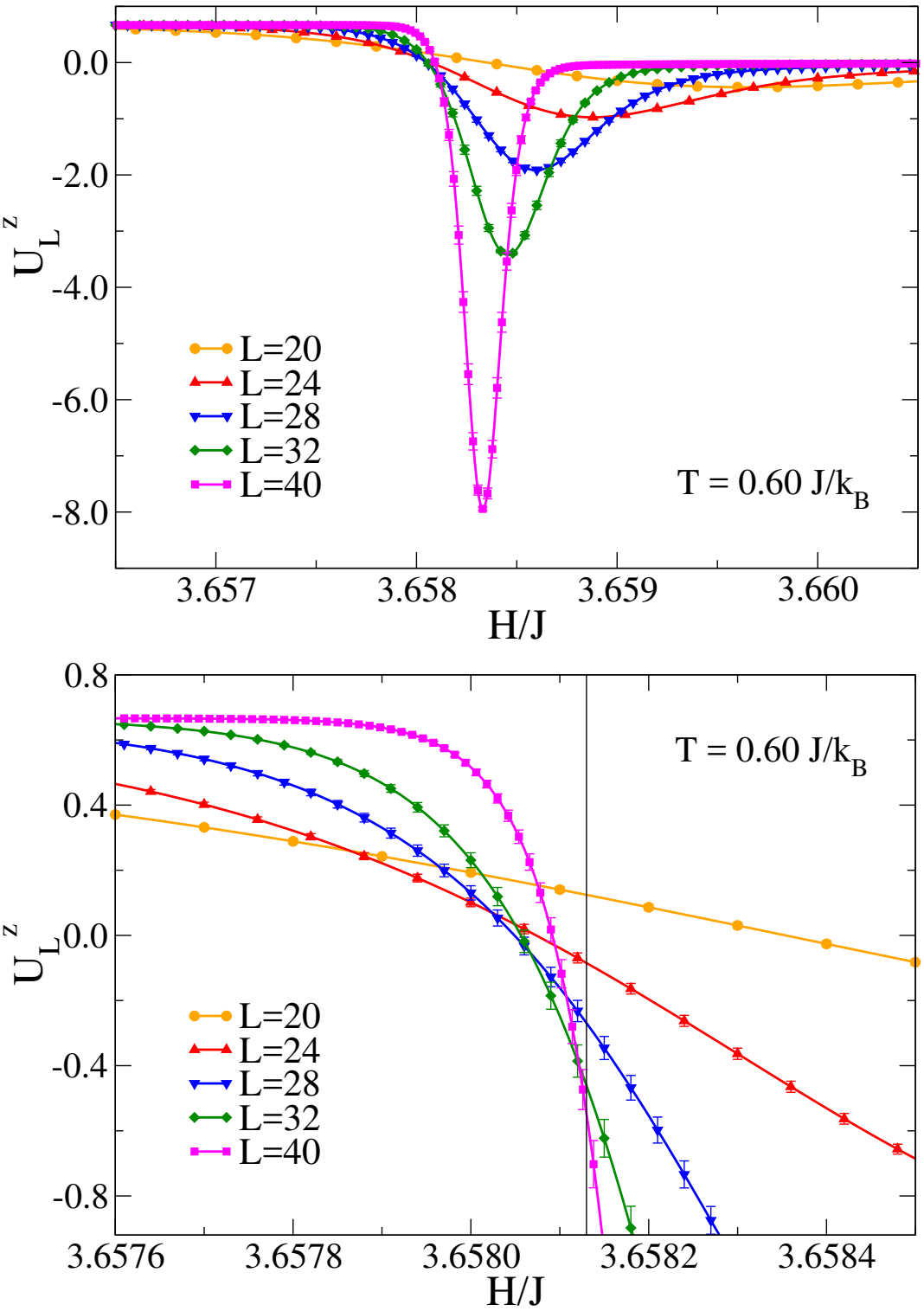

Figure 5.11: Top: Variation of the fourth-order cumulant of the AF order parameter vs magnetic field for different lattice sizes at $T = 0.60J/k_B$. Bottom: Same as above but on a finer scale.

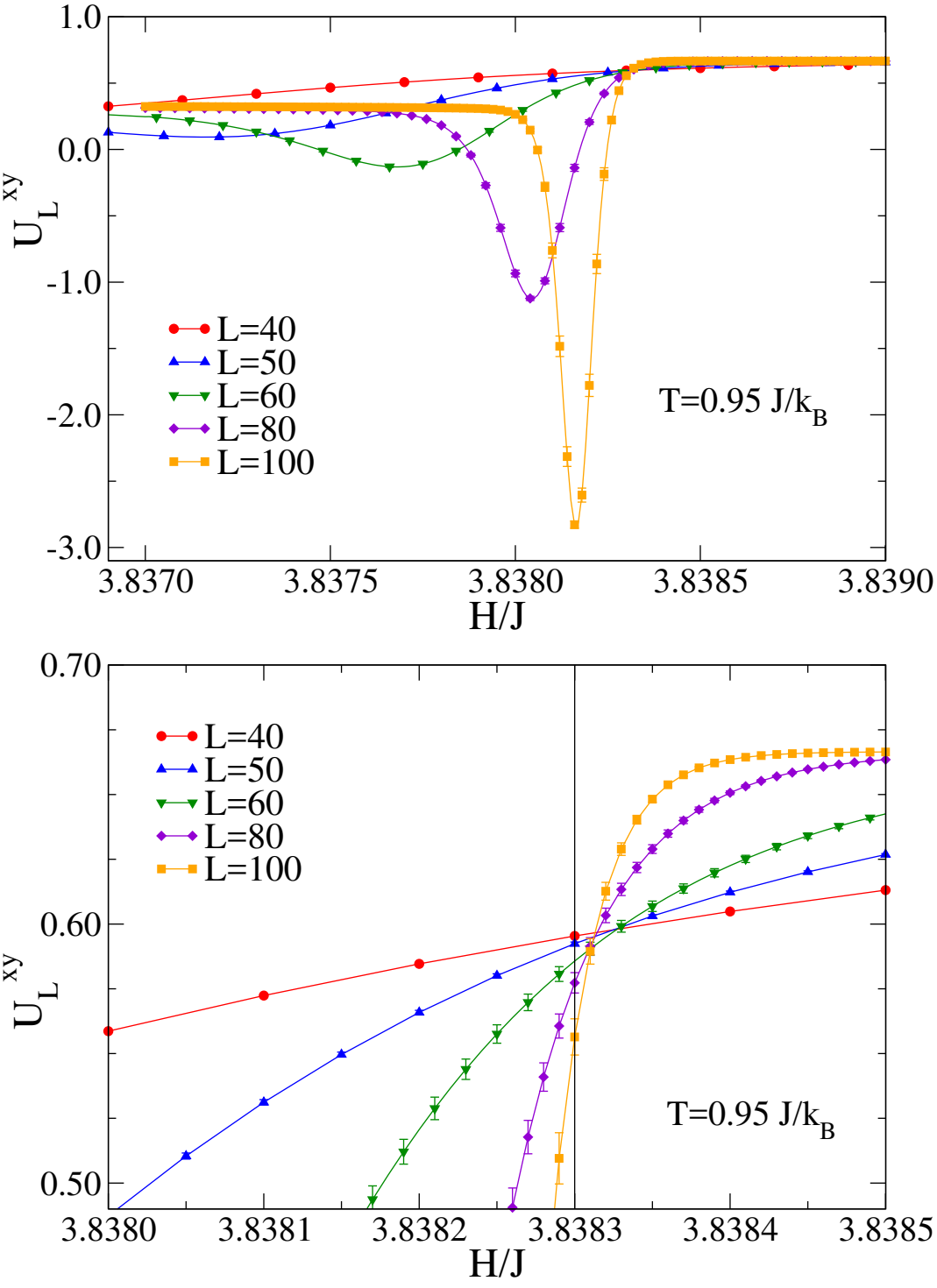

Figure 5.12: Top: Variation of the fourth-order cumulant of the SF order parameter vs magnetic field for different lattice sizes at $T = 0.95J/k_B$. Bottom: Same as above but on a finer scale.

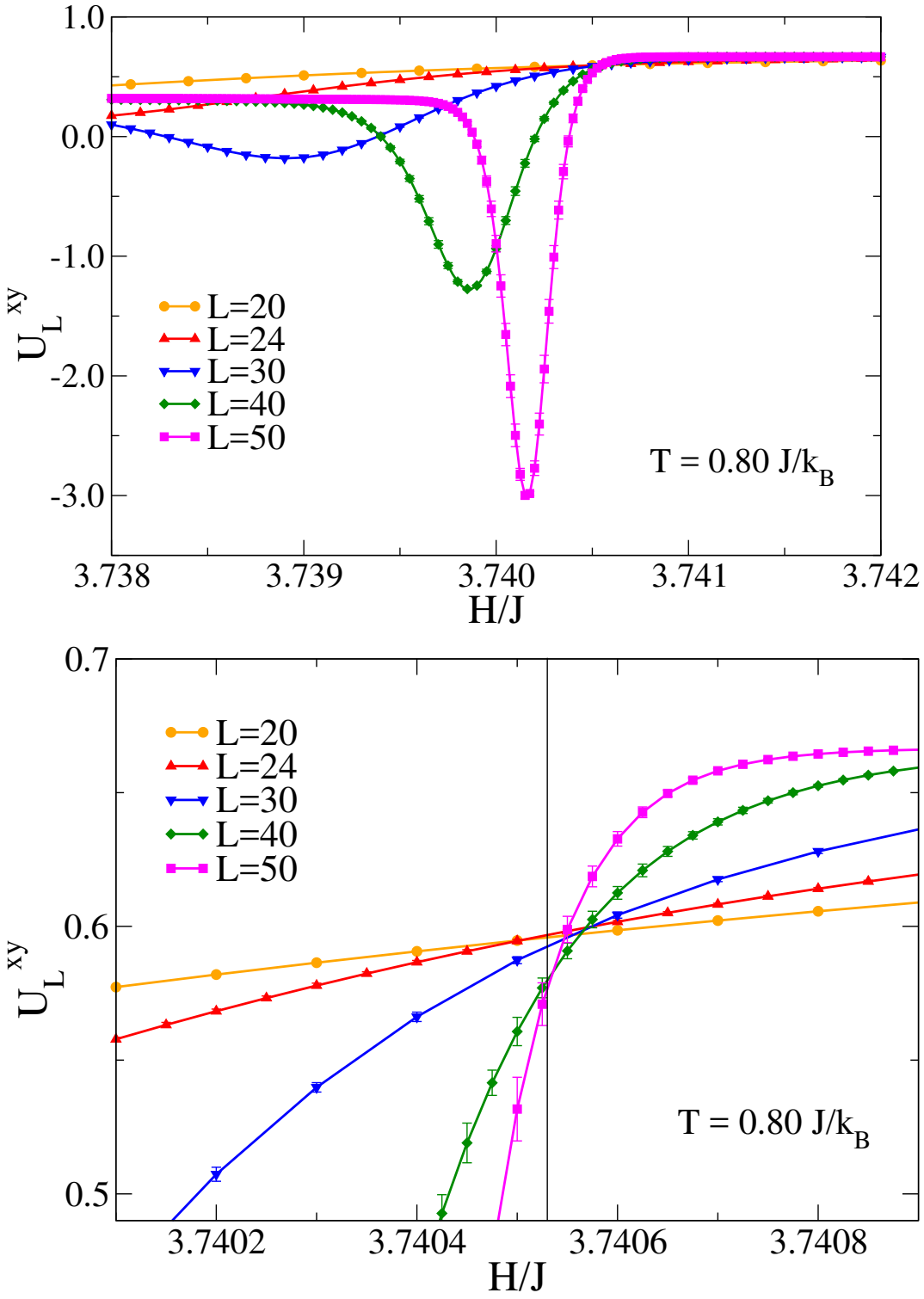

Figure 5.13: Top: Variation of the fourth-order cumulant of the SF order parameter vs magnetic field for different lattice sizes at $T = 0.80J/k_B$. Bottom: Same as above but on a finer scale.

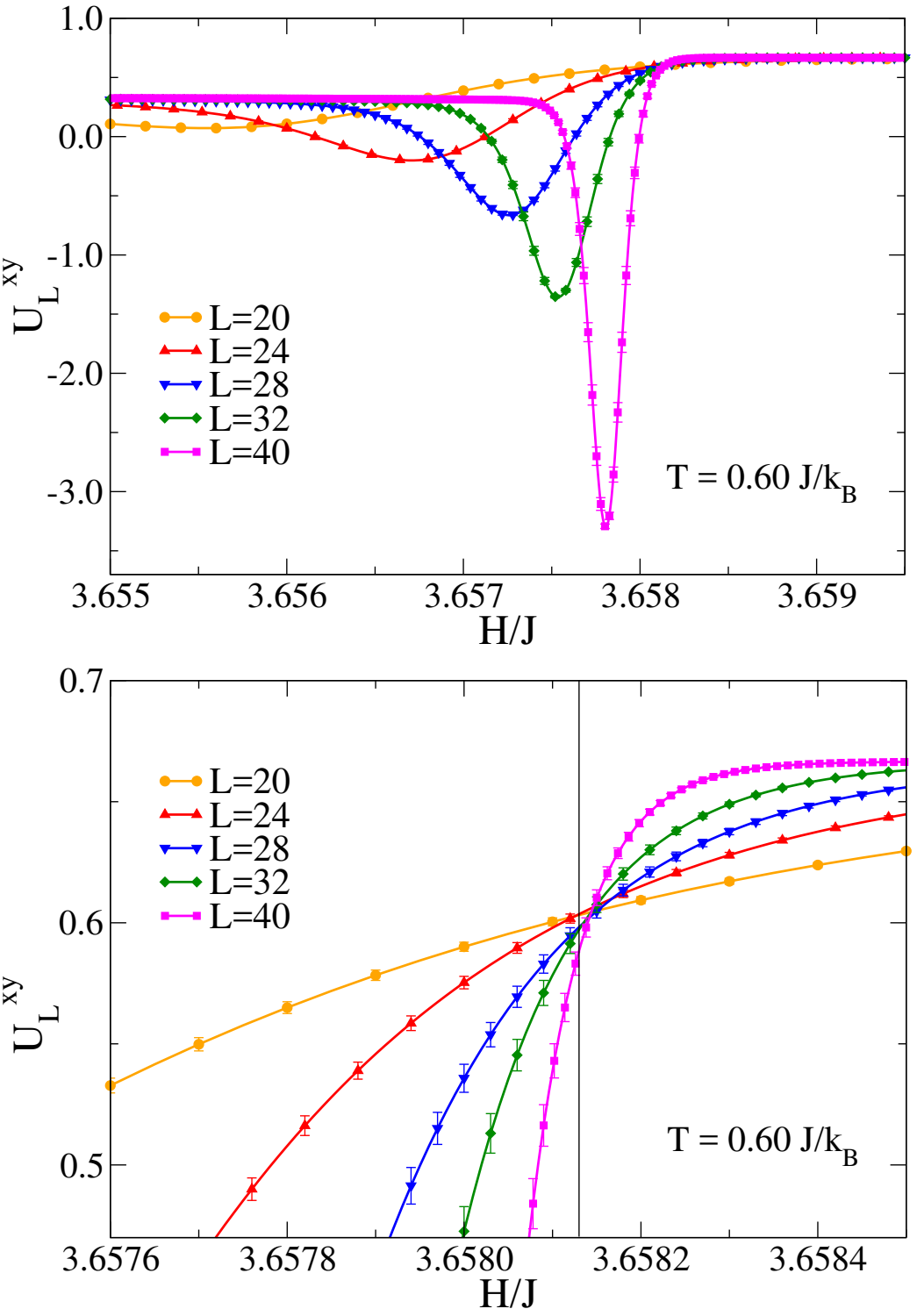

Figure 5.14: Top: Variation of the fourth-order cumulant of the SF order parameter vs magnetic field for different lattice sizes at $T = 0.60J/k_B$. Bottom: Same as above but on a finer scale.

crossing point values are just below $U_\infty^{xy} = 0.6$ and are higher than the predicted value of $U_\infty^{xy} = 0.56056$ assuming an effective value of $q = \pi$. However, the bottom portions of Fig. 5.12 - 5.14 show a clear tendency for the crossing point values to decrease slightly with increasing size, and the predicted value is not inconsistent with an extrapolation to $L = \infty$. [Note: Use of $U_\infty^{xy} = 0.6$ in Eq. (4.23) would yield $q = 5$.]

5.3 Individual moments

As a check on the assumptions about the degeneracy of the SF order parameter, in Fig. 5.15 we show the order parameter distribution in the xy plane at the transition field H_L^t for an $L = 60$ lattice at $T = 0.95J/k_B$. The contours of constant absolute value are almost perfectly circular and show a clear jump from the non-zero value in the SF-phase to a small value in the AF-phase which differs from zero only because of finite size effects.

The probability distributions of the SF order parameter ψ at $T = 0.95J/k_B$, $T = 0.80J/k_B$, and $T = 0.60J/k_B$ are shown at the transition field for different lattice sizes L in Fig. 5.16. For each size we chose the finite size transition field to be located at the same point at which the (symmetric) peaks in the probability distribution for the energy were of equal heights. These data show that the distributions contain two clear peaks at $\pm\psi_\infty$ corresponding to the SF order and a peak centered about zero corresponding to the AF phase. These peaks cannot be described solely by Gaussians since the states describing phase coexistence (from about $|\vec{\psi}| \approx 0.2$ to $|\vec{\psi}| \approx 0.36$ at $T = 0.95J/k_B$) are not yet strongly suppressed. If we "separate" the distributions into two peaks by choosing the minimum probability as the separation point, we can measure the "weight" of each peak by numerically integrating the probability under each peak. As shown in Table 5.2 the relative weight of the sum of the "ordering" peaks and the disordered peak depends upon the exact choice of H^t and is also slightly dependent upon the choice of L. For our best estimate of $H^t/J = 3.838305$

at $T = 0.95J/k_B$, the value appears to be converging for large L at the estimate of $q = \pi$ that was obtained earlier using the two Gaussian approximation. Similar behavior happens for $T = 0.80J/k_B$ and $T = 0.60J/k_B$ as well. Note that the result $q = \pi$ was already predicted from the two delta-function distribution appropriate to the thermodynamic limit in Eq. (4.14).

For completeness we show the probability of the AF order parameter vs $\tilde{m}_z$ in Fig. 5.17. For small systems two peaks are seen at $\pm\tilde{m}_\infty$ with a broad plateau in between, but as L increases three distinct peaks develop. One peak, centered about $\tilde{m}_z = 0$ is for the SF phase

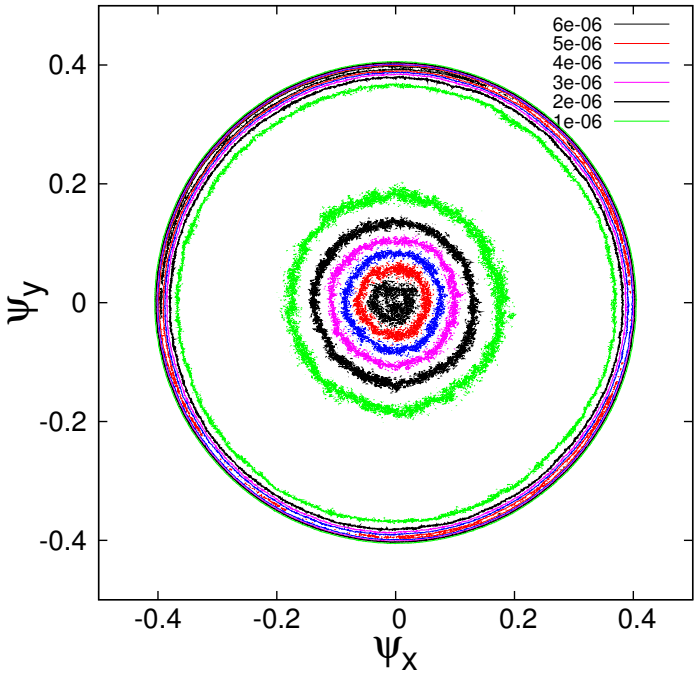

Figure 5.15: Contours for the order parameter distribution $P_L(\vec{\psi})$ with $\vec{\psi} = (\psi_x, \psi_y)$ being the two component order parameter comprising the xy-components of the staggered magnetization in the spin-flop phase for an $L = 60$ lattice at $H = H_L^t$ at $T = 0.95J/k_B$. Different colors denote the magnitude of the probability (from the center outwards the probability first decreases and then increases again).

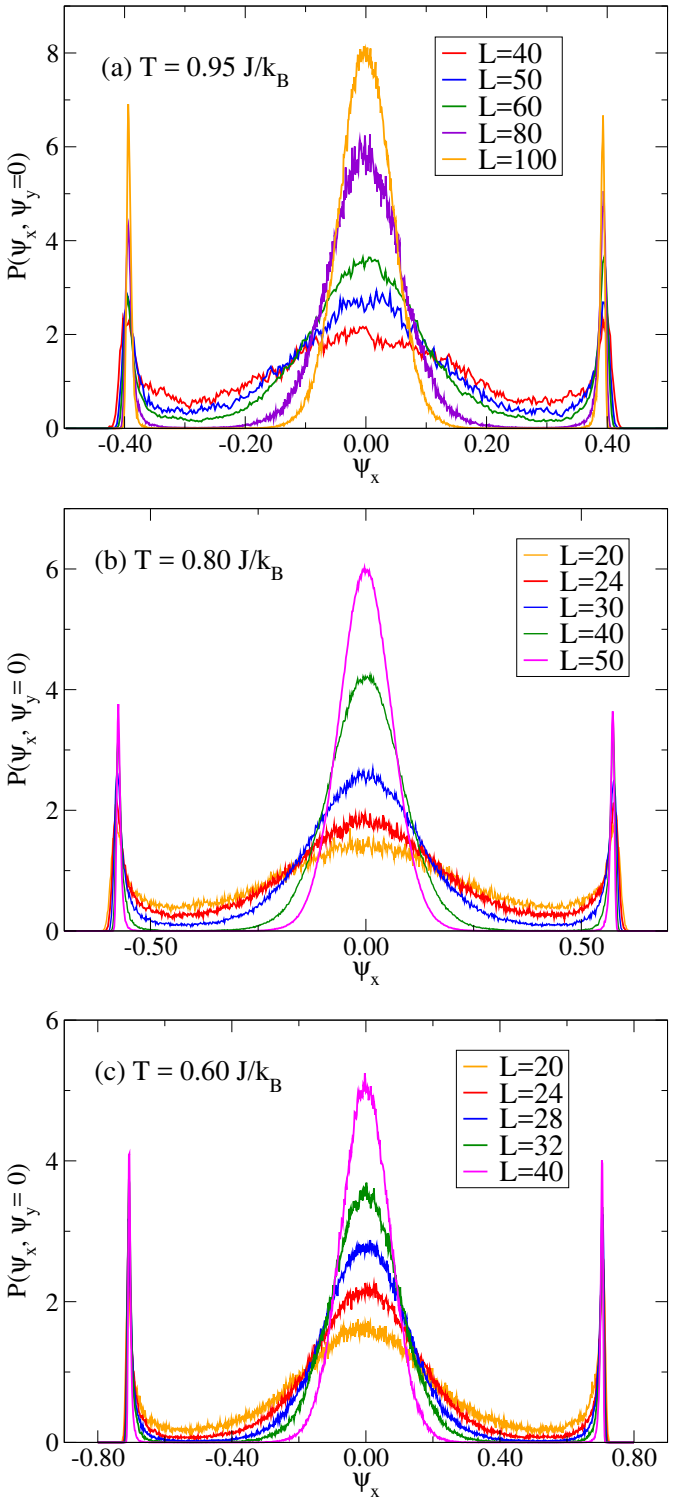

Figure 5.16: Probability density of the SF order parameter ψ_x, with $\psi_y = 0$ for different lattice sizes. (a) $T = 0.95J/k_B$, (b) $T = 0.80J/k_B$, (c) $T = 0.60J/k_B$.

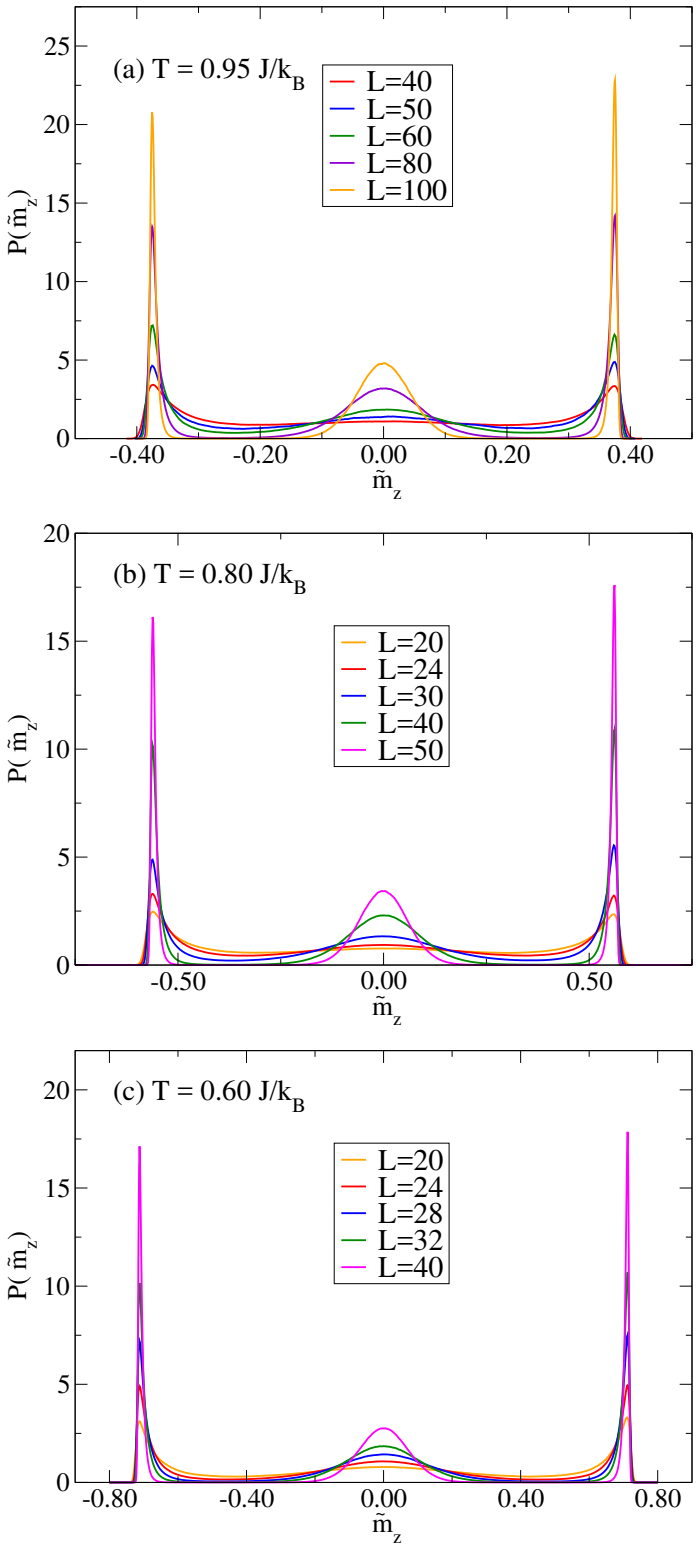

Figure 5.17: Probability density of the AF order parameter $\tilde{m}_z$, for different lattice sizes. (a) $T = 0.95J/k_B$, (b) $T = 0.80J/k_B$, (c) $T = 0.60J/k_B$.

Table 5.2: Estimates for q_{eff} from the ratio of probability distributions of the weights of the peaks for different values of L. (Top) $T = 0.95J/k_B$, (Middle) $T = 0.80J/k_B$, (Bottom) $T = 0.60J/k_B$.

L	$H^t/J = 3.838300$	$H^t/J = 3.838305$	$H^t/J = 3.838310$
60	3.31(23)	3.42(30)	3.53(28)
80	3.15(24)	3.36(26)	3.75(29)
100	2.82(30)	3.19(29)	3.82(30)

L	$H^t/J = 3.740520$	$H^t/J = 3.740525$	$H^t/J = 3.7405230$
30	3.20(29)	3.24(32)	3.27(30)
40	3.16(23)	3.27(25)	3.38(21)
50	3.06(33)	3.28(27)	3.51(31)

L	$H^t/J = 3.658125$	$H^t/J = 3.658130$	$H^t/J = 3.658135$
28	3.30(21)	3.39(23)	3.48(26)
32	3.22(26)	3.36(30)	3.51(31)
40	3.04(24)	3.31(28)	3.62(31)

with no AF order and the peaks at $\pm\tilde{m}_\infty$ are for the AF ordered phase. Again, the minima between the peaks can be interpreted in terms of phase coexistence.

Perhaps the most striking results of our study emanate from Eqs. (4.17), (4.18), (4.20), and (4.21). Plots of $\langle|\vec{\psi}|\rangle_L$, $\langle\psi^2\rangle_L$, $\langle|\tilde{m}_z|\rangle_L$, and $\langle\tilde{m}_z^2\rangle_L$, vs H should show common intersection points for different L at H^t. These features would **not** occur at a second-order transition, but are nicely consistent with our phenomenological theory. In Figs. 5.18 to 5.23 we show data for the first and second moments of ψ, $\tilde{m}_z$ and, for completeness, m_z near the transition. From Eqs. (4.17) and (4.18) we conclude that

$$\frac{\langle|\vec{\psi}|\rangle_L|_{H^t}}{\psi_\infty} = \frac{\langle\psi^2\rangle_L|_{H^t}}{\psi_\infty^2} = \frac{q}{1+q} \approx 0.7585 \tag{5.2}$$

and from Eqs. (4.20) and (4.21)

$$\frac{\langle|\tilde{m}_z|\rangle_L|_{H^t}}{\tilde{m}_{z,\infty}} = \frac{\langle\tilde{m}_z^2\rangle_L|_{H^t}}{\tilde{m}_{z,\infty}^2} = \frac{1}{1+q} \approx 0.2415 \ . \tag{5.3}$$

Here too, the data show small but systematic shifts with increasing system size and we can only say that the predictions are consistent with the current data which yield

At $T = 0.95J/k_B$	At $T = 0.80J/k_B$	At $T = 0.60J/k_B$
$\frac{\langle\|\vec{\psi}\|\rangle_L\|_{H^t}}{\psi_\infty} \approx 0.77(3)$	$\frac{\langle\|\vec{\psi}\|\rangle_L\|_{H^t}}{\psi_\infty} \approx 0.78(3)$	$\frac{\langle\|\vec{\psi}\|\rangle_L\|_{H^t}}{\psi_\infty} \approx 0.79(4)$
$\frac{\langle\psi^2\rangle_L\|_{H^t}}{\psi_\infty^2} \approx 0.74(3)$	$\frac{\langle\psi^2\rangle_L\|_{H^t}}{\psi_\infty^2} \approx 0.75(4)$	$\frac{\langle\psi^2\rangle_L\|_{H^t}}{\psi_\infty^2} \approx 0.76(3)$
$\frac{\langle\|\tilde{m}_z\|\rangle_L\|_{H^t}}{\tilde{m}_{z,\infty}} \approx 0.32(4)$	$\frac{\langle\|\tilde{m}_z\|\rangle_L\|_{H^t}}{\tilde{m}_{z,\infty}} \approx 0.30(4)$	$\frac{\langle\|\tilde{m}_z\|\rangle_L\|_{H^t}}{\tilde{m}_{z,\infty}} \approx 0.29(4)$
$\frac{\langle\tilde{m}_z^2\rangle_L\|_{H^t}}{\tilde{m}_{z,\infty}^2} \approx 0.26(3).$	$\frac{\langle\tilde{m}_z^2\rangle_L\|_{H^t}}{\tilde{m}_{z,\infty}^2} \approx 0.24(3).$	$\frac{\langle\tilde{m}_z^2\rangle_L\|_{H^t}}{\tilde{m}_{z,\infty}^2} \approx 0.25(3).$

These values are in quite reasonable agreement with predictions although more precise values would be needed to draw strong conclusions. However, the discrepancies between the measured and predicted values noted above can probably be attributed to the difference in the location of the intersections and our best estimate for the transition field in the thermodynamic limit. Using more precise data on still larger systems to extrapolate the small finite size variations to $L \to \infty$ could give slightly different estimates than quoted above but would require prohibitively large resources at the present time.

An alternative approach is to base our analysis on Eq. (4.60) which describes the slope of $\langle\psi^2\rangle_L$ at the transition field H^t as a function of H/k_BT. From the corresponding plot of $d\langle\psi^2\rangle_L/d(H/J)|_{H^t}$, normalized by $J\Delta m L^3\psi_\infty^2/k_BT$, vs L^{-3} we expect linear behavior whose intercept is $q/(1+q)^2 \approx 0.182$ if $q = \pi$. Such a plot, shown in Fig. 5.24 is, indeed, reasonably compatible with this conjecture.

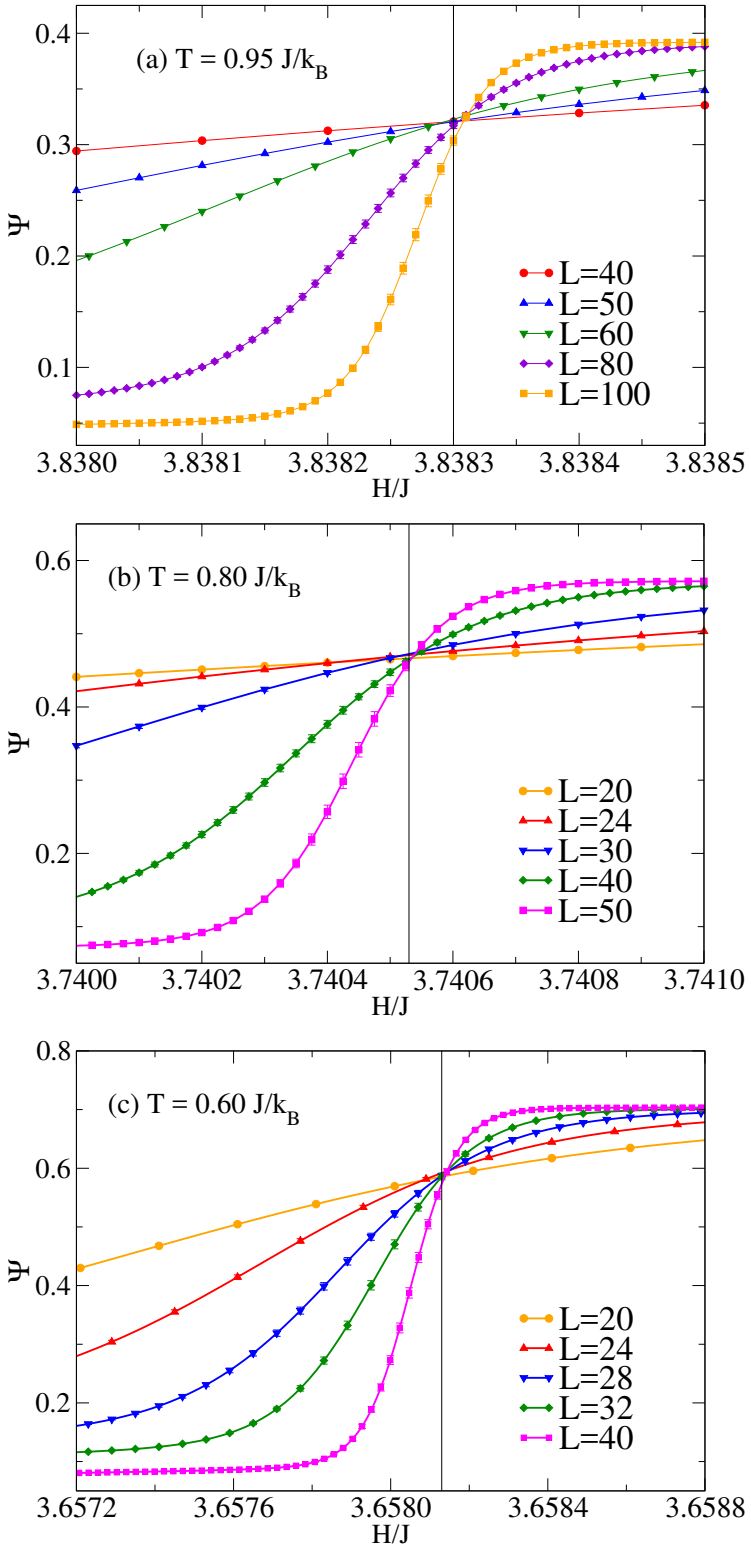

Figure 5.18: Variation of the SF order parameter vs magnetic field for different lattice sizes. (a) $T = 0.95J/k_B$, (b) $T = 0.80J/k_B$, (c) $T = 0.60J/k_B$.

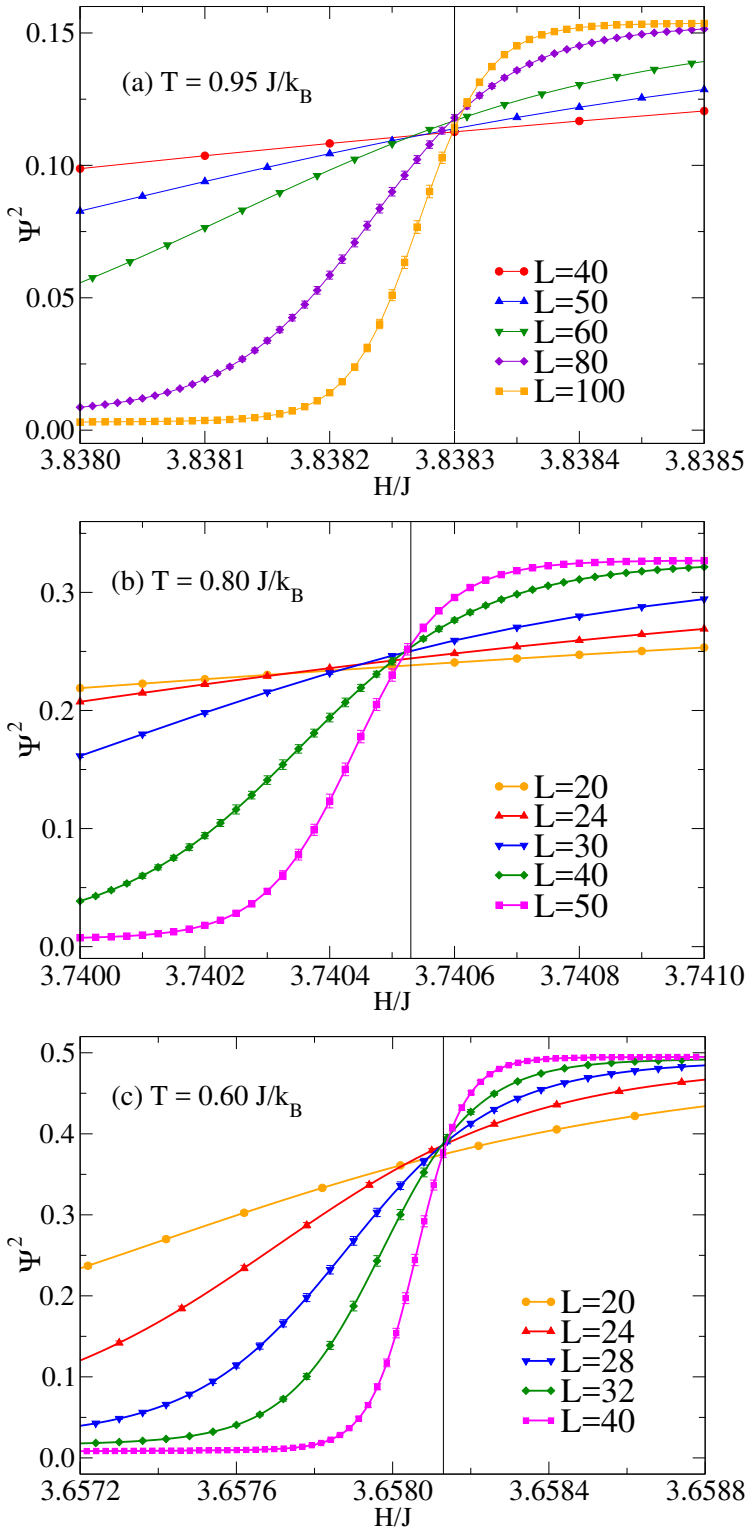

Figure 5.19: Variation of the square of the xy-component of the order parameter vs magnetic field for different lattice sizes. (a) $T = 0.95J/k_B$, (b) $T = 0.80J/k_B$, (c) $T = 0.60J/k_B$.

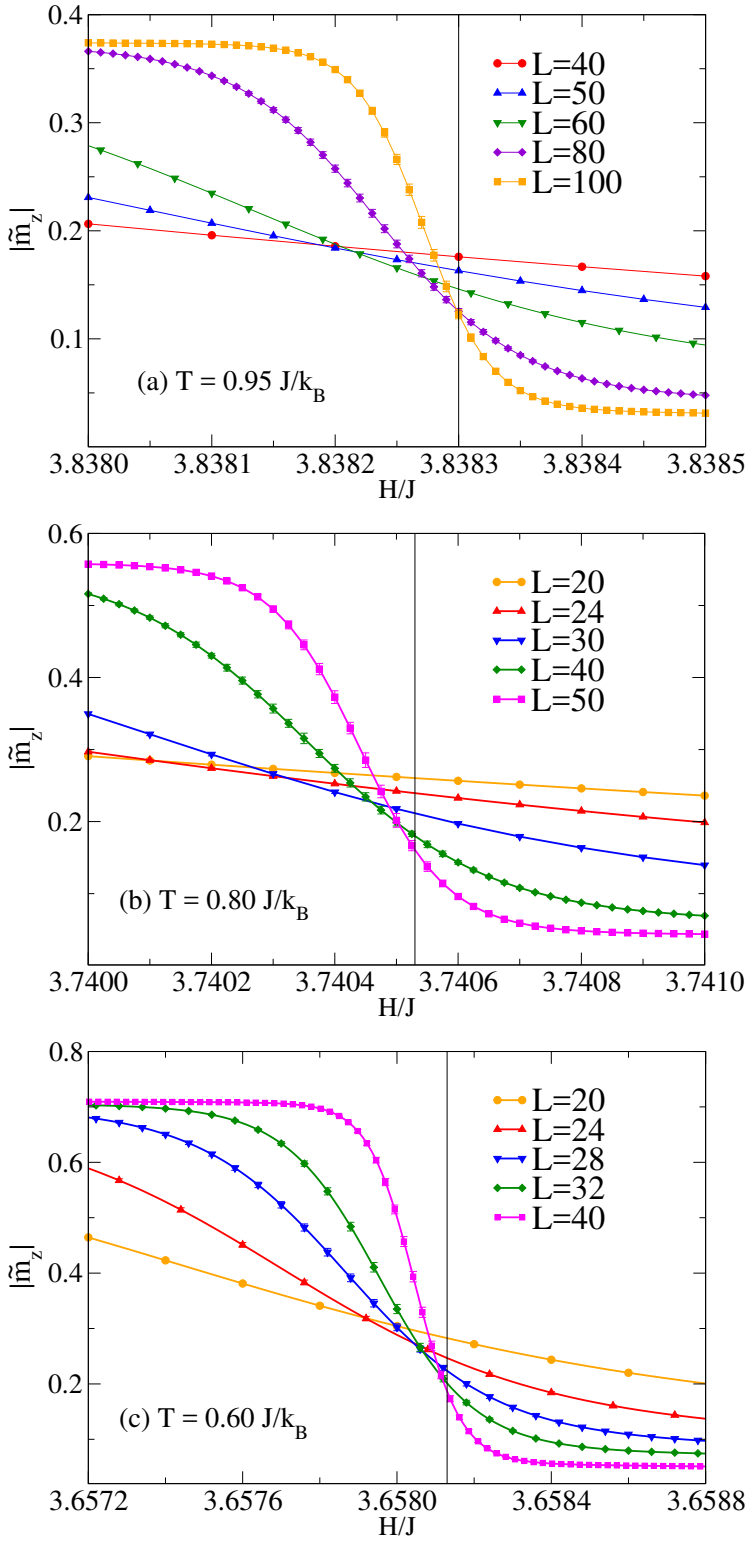

Figure 5.20: Variation of the AF order parameter vs magnetic field for different lattice sizes. (a) $T = 0.95J/k_B$, (b) $T = 0.80J/k_B$, (c) $T = 0.60J/k_B$.

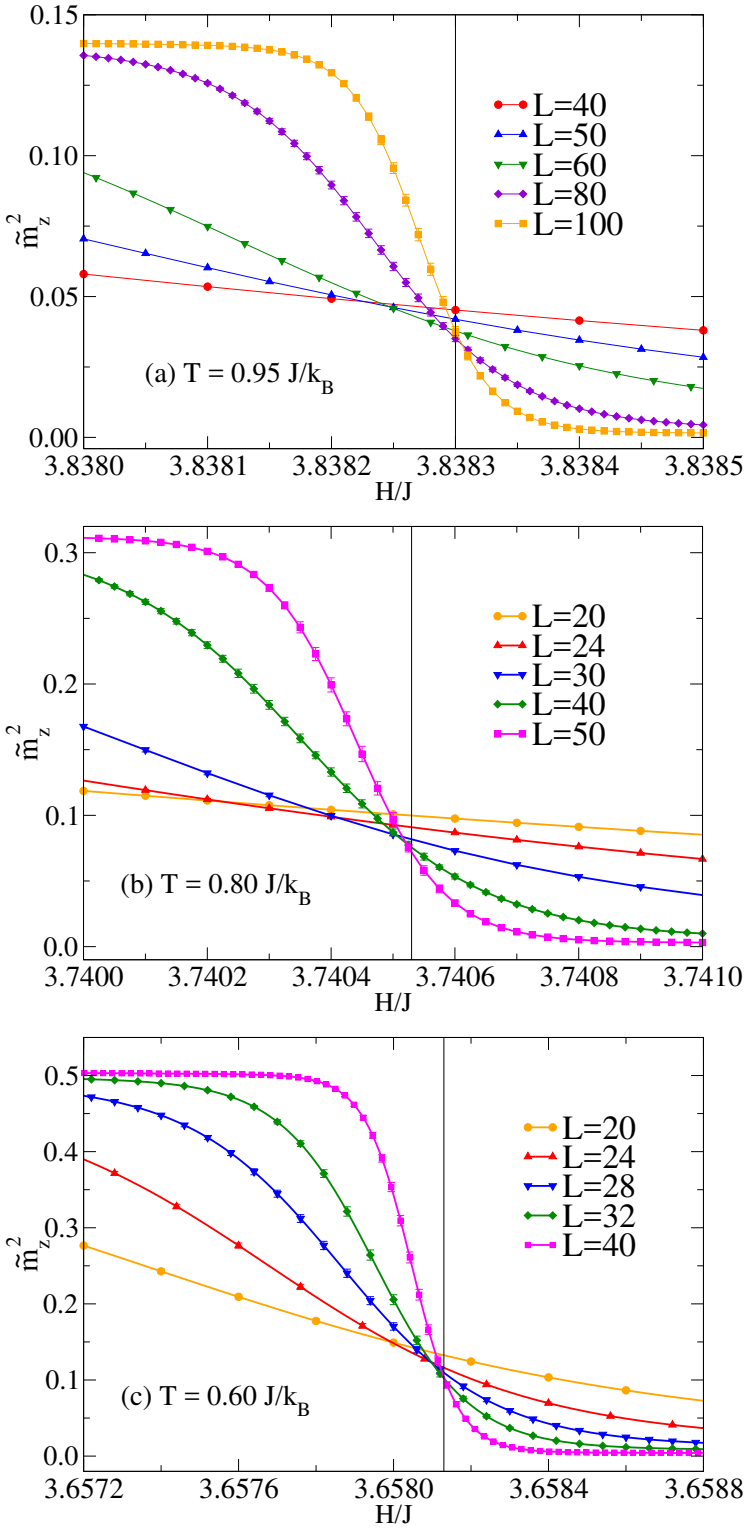

Figure 5.21: Variation of the square of the z-component of the order parameter vs magnetic field for different lattice sizes. (a) $T = 0.95J/k_B$, (b) $T = 0.80J/k_B$, (c) $T = 0.60J/k_B$.

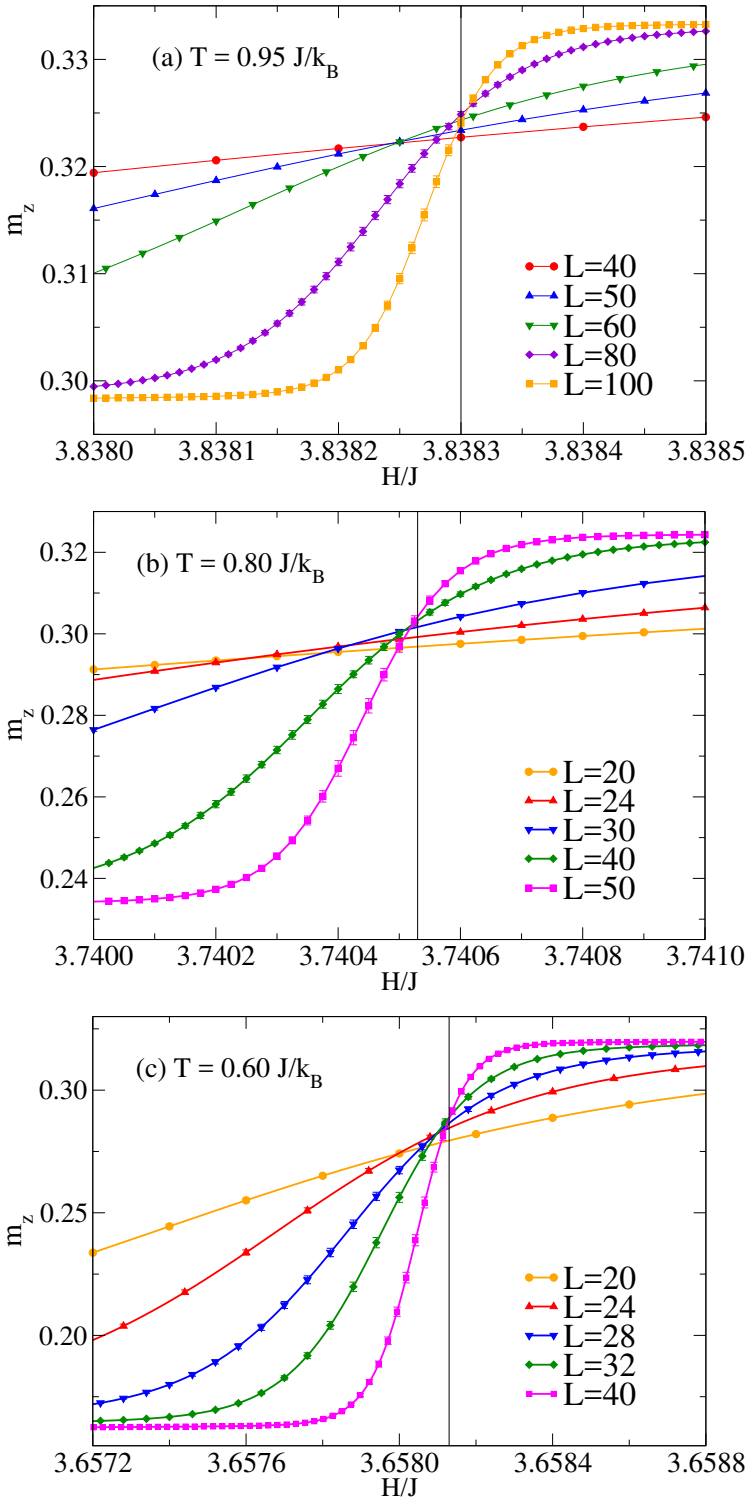

Figure 5.22: Variation of the z-component of the magnetization vs magnetic field for different lattice sizes. (a) $T = 0.95J/k_B$, (b) $T = 0.80J/k_B$, (c) $T = 0.60J/k_B$.

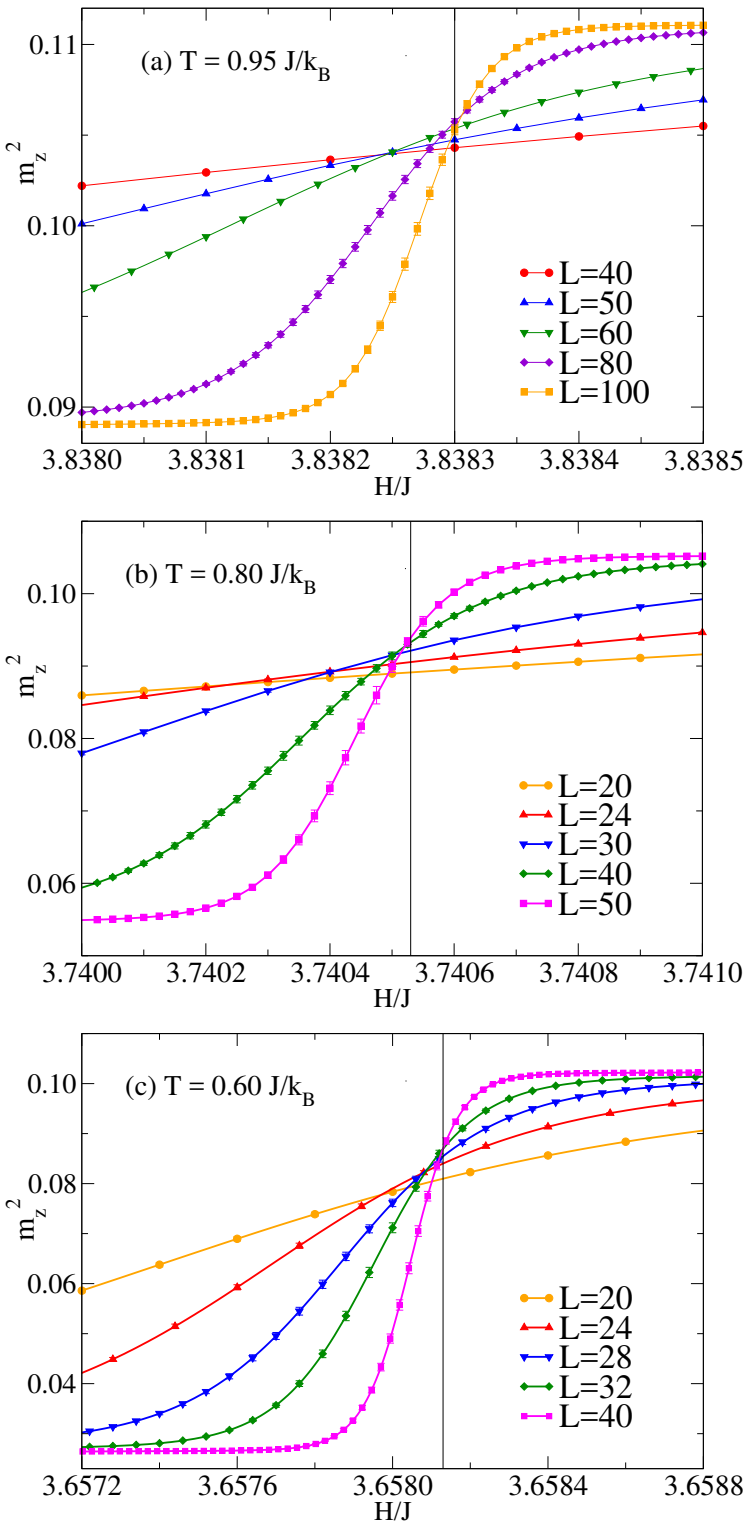

Figure 5.23: Variation of the square of the z-component of the magnetization vs magnetic field for different lattice sizes. (a) $T = 0.95J/k_B$, (b) $T = 0.80J/k_B$, (c) $T = 0.60J/k_B$.

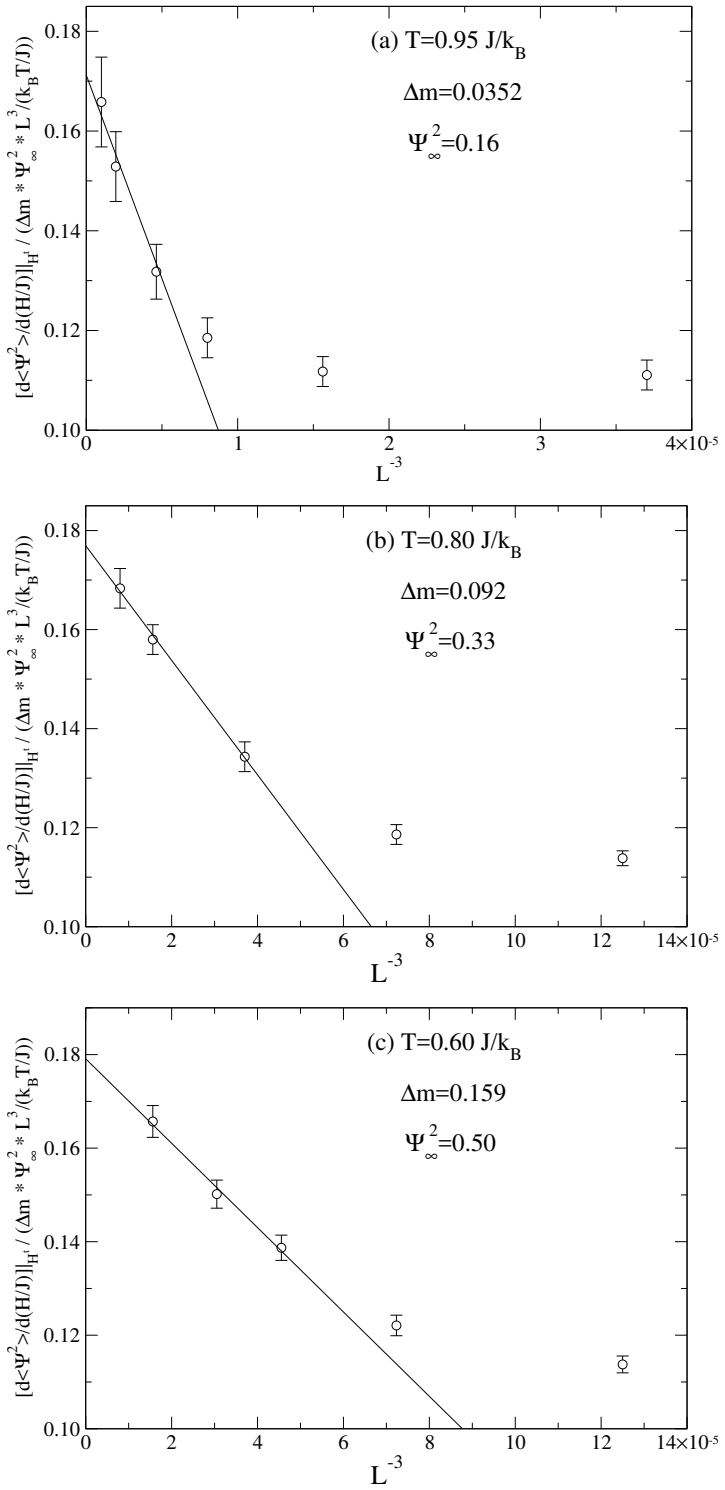

Figure 5.24: Variation of the "normalized" slope of $\langle \psi^2 \rangle_L$ with respect to H at the transition field H^t vs the inverse volume L^{-3} of the system. The straight line is a linear extrapolation to the thermodynamic limit. (a) $T = 0.95 J/k_B$, (b) $T = 0.80 J/k_B$, (c) $T = 0.60 J/k_B$.

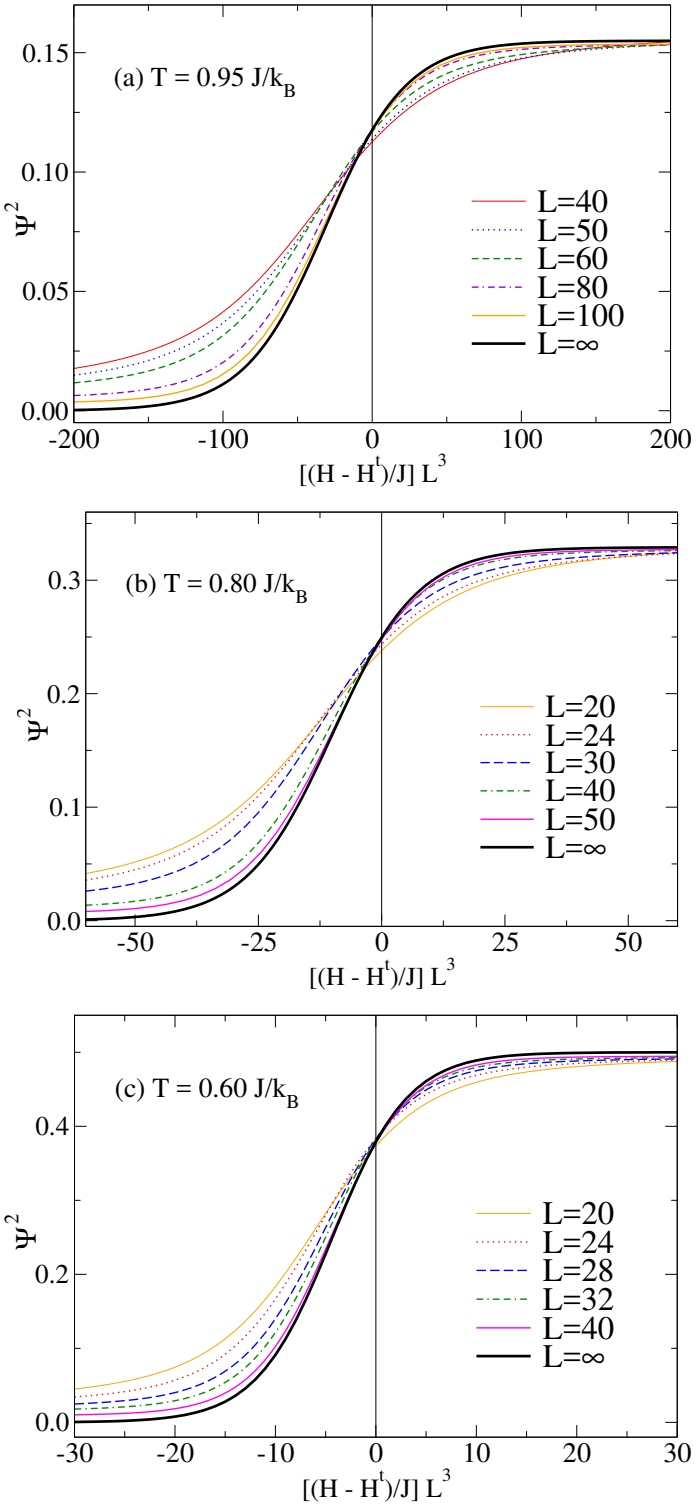

Figure 5.25: Finite size scaling plot for $\langle \psi^2 \rangle_L$. The heavy, solid curve shows the asymptotic theoretical behavior in the limit $L = \infty$. (a) $T = 0.95 J/k_B$, (b) $T = 0.80 J/k_B$, (c) $T = 0.60 J/k_B$.

Near the transition, where b can be neglected, Eq. (4.57) leads to a simple finite size scaling expression for ψ^2 that is tested in Fig. 5.25 in which ψ^2 is plotted vs. $(H - H^t)L^3$ where (a) $H^t/J = 3.83830$ for $T = 0.95J/k_B$, (b) $H^t/J = 3.74053$ for $T = 0.80J/k_B$, and (c) $H^t/J = 3.65813$ for $T = 0.60J/k_B$. For large enough values of L and $H - H^t$, the values for ψ^2 collapse onto a single curve representing a simple analytic scaling function describing the behavior near the transition between these two different ordered phases. For large but negative values of $H - H^t$, curves should instead approach the small constant b in Eq. (4.57) which goes to zero as L^{-3}. The data bear out these predictions.

5.4 Crossover effect between bicritical and spin-flop regions

Here we want to consider the effect of the nearby bicritical point on the finite-size behavior of the fourth-order cumulant of $\tilde{m}_z$ leading to the dramatic variation in crossing points in Fig. 5.9 to 5.11.

When the normal distance $d_{SF}(T, H)$ from the SF-P phase boundary inside the region of SF order is rather small, the correlation length ξ_{SF} of order parameter fluctuations is very large. As is standard for critical phenomena, this is described by the power law $\xi_{SF} \propto d_{SF}^{-\nu_{xy}}$, where ν_{xy} is the (universal) critical exponent of the XY model. Likewise, in the region of the AF phase close to the AF-P phase boundary, the correlation length ξ_{AF} of fluctuations of the AF order parameter is very large, $\xi_{AF} \propto d_{AF}^{-\nu_I}$, $d_{AF}(T, H)$ being the normal distance from the AF-P phase boundary, and ν_I the critical exponent of the Ising universality class. These power laws, however, apply only for a state point (T, H) that is not too close to the bicritical point (T_b, H_b). Close to the bicritical point, all components of the staggered magnetization are simultaneously critical, and the fluctuations are characterized by Heisenberg criticality, with $\xi \propto d^{-\nu_H}$, where d is the distance of the state point from the bicritical point. This

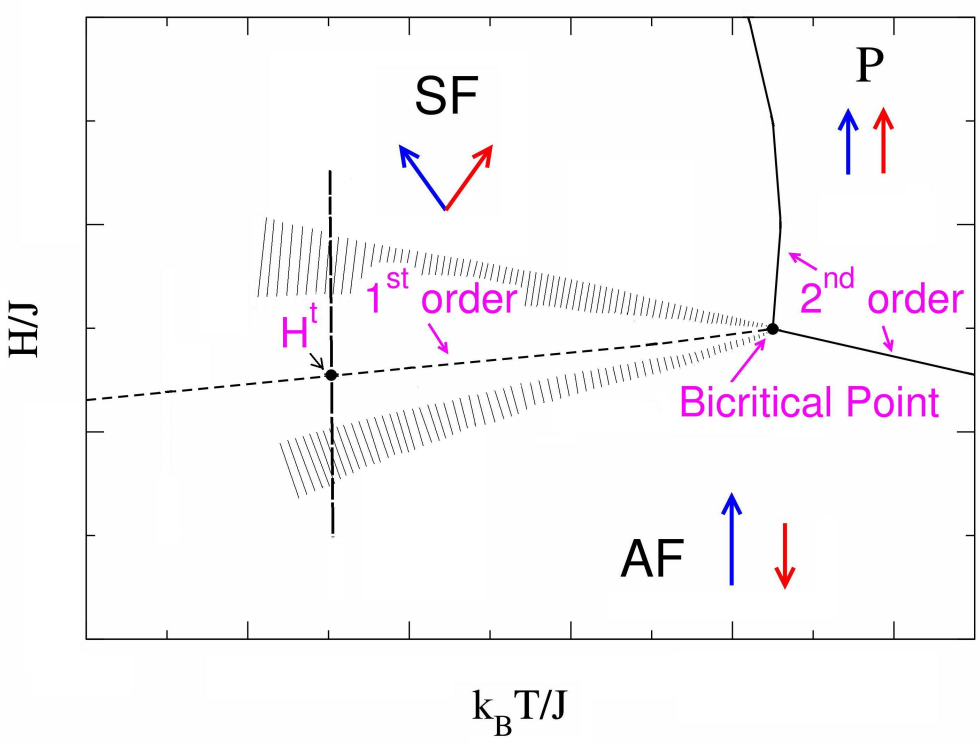

Figure 5.26: Phase diagram near the bicritical point showing crossover (shaded regions) between the bicritical and spin-flop regions. (Crossover regions between the bicritical point and other phase boundaries are omitted for clarity.)

latter relation applies when d is sufficiently small and outside the two shaded regions in the schematic sketch, Fig. 5.26. Within the shaded regions, a smooth crossover to the first-order behavior at the spin-flop boundary occurs.

We conclude that near the AF-SF phase boundary for $T < T_b(H)$ there is a region where order parameter fluctuations of Heisenberg model type occur, and the correlation length ξ of these fluctuations only gradually diminishes with the distance from the bicritical point. Even at the chosen temperature $T = 0.95J/k_B$, this correlation length must still be fairly large; and while we have not determined it directly, we can safely conclude this since probability distributions of energy (Fig. 5.1), magnetization (Fig. 5.2), and order parameter components are still very broad for $L = 40$. Moreover, for smaller L the two coexisting phases can hardly

be recognized from these distributions. The broadness of the peaks for $L = 40$ in these figures is evidence that the corresponding (staggered) susceptibilities are still very large as well.

From these observations we can also conclude that the behavior of various cumulants at $T = 0.95J/k_B$ are still Heisenberg-like when $L \ll 40$, and when $L \approx 40$ a gradual crossover from this critical behavior to the behavior characteristic for the first-order transition begins to set in.

To provide quantitative evidence for this scenario, we recall that for a Heisenberg antiferromagnet the order parameter distribution $P_L(\tilde{\vec{m}})$ exhibits full rotational symmetry in order parameter space. Using polar coordinates

$$\tilde{\vec{m}}_z = \tilde{m}\cos\theta, \quad \tilde{\vec{m}}_x = \tilde{m}\sin\theta\cos\varphi, \quad \tilde{\vec{m}}_y = \tilde{m}\sin\theta\sin\varphi, \tag{5.4}$$

we can write $P_L\left(\tilde{\vec{m}}\right)d\tilde{\vec{m}} = P_L(\tilde{m})\tilde{m}^2 d\tilde{m}\sin\theta d\theta d\varphi$, where only a distribution $P_L(\tilde{m})$ of the magnitude $\tilde{m}$ of the order parameter is needed.

The order parameter cumulant of the Heisenberg model

$$U^H = 1 - \langle(\tilde{\vec{m}}^{\,2})^2\rangle/(3\langle\tilde{\vec{m}}^{\,2}\rangle^2) \tag{5.5}$$

at criticality is well known [88, 89]

$$U_*^H = 0.620(1). \tag{5.6}$$

But Eq. (5.5) is not what has been computed in the main text of this paper, where rather cumulants of $\tilde{\vec{m}}_z$ {Eq. (4.24)} or the transverse order parameter $\vec{\psi} = (\tilde{\vec{m}}_x, \tilde{\vec{m}}_y)$ {Eq. (4.23)} were considered. However, it turns out that it is straightforward to consider these quantities U^z, U^{xy} for Heisenberg criticality as well, and actually both of them can be expressed in

terms of U^H. In order to see this, we first note that

$$\langle \tilde{\vec{m}}^2 \rangle = \int_0^\infty \tilde{m}^4 P_L(\tilde{m}) d\tilde{m} \Big/ \int_0^\infty \tilde{m}^2 P_L(\tilde{m}) d\tilde{m}, \tag{5.7}$$

$$\langle (\tilde{\vec{m}}^2)^2 \rangle = \int_0^\infty \tilde{m}^6 P_L(\tilde{m}) d\tilde{m} \Big/ \int_0^\infty \tilde{m}^2 P_L(\tilde{m}) d\tilde{m}, \tag{5.8}$$

the angular part simply cancels out in both expressions. Now from symmetry it is trivial to conclude that

$$\langle \tilde{\vec{m}}_z^2 \rangle = \frac{1}{3} \langle \tilde{\vec{m}}^2 \rangle, \quad \langle \psi^2 \rangle = \frac{2}{3} \langle \tilde{\vec{m}}^2 \rangle, \tag{5.9}$$

while in $\langle \tilde{m}_z^4 \rangle$, $\langle \psi^4 \rangle$ the angular parts contribute, but are straightforward to compute, e.g.

$$\langle \tilde{\vec{m}}_z^4 \rangle = \frac{\int_0^\infty \tilde{m}^6 P_L(\tilde{m}) d\tilde{m} \int_0^\pi \cos^4\theta \sin\theta d\theta}{\int_0^\infty \tilde{m}^2 P_L(\tilde{m}) d\tilde{m} \int_0^\pi \sin\theta d\theta} = \frac{1}{5} \langle (\tilde{\vec{m}}^2)^2 \rangle \tag{5.10}$$

and similarly

$$\langle \psi^4 \rangle = \frac{8}{15} \langle (\tilde{\vec{m}}^2)^2 \rangle. \tag{5.11}$$

Thus, we find

$$U^z = 1 - \frac{3}{5} \frac{\langle (\tilde{\vec{m}}^2)^2 \rangle}{\langle \tilde{\vec{m}}^2 \rangle^2} = \frac{9}{5} U_H - \frac{4}{5} \quad , \tag{5.12}$$

and

$$U^{xy} = 1 - \frac{2}{5} \frac{\langle (\tilde{\vec{m}}^2)^2 \rangle}{\langle \tilde{\vec{m}}^2 \rangle^2} = \frac{6}{5} U_H - \frac{1}{5}. \tag{5.13}$$

Using Eq. (5.6), we hence predict that in the bicritical region,

$$U_*^z \approx 0.316(2), \quad U_*^{xy} \approx 0.544(1). \tag{5.14}$$

Looking at Fig. 5.9 for $T = 0.95J/k_B$, we see that for $L = 40$, $L = 50$, we still have spurious cumulant crossing somewhere in the region of $U_L^z \approx 0.34(3)$, while for larger L the crossings move towards significantly smaller values. For the pair $L = (80, 100)$ the crossing point is negative. We recall that a degeneracy constant $q = \pi$ (see Eq. (4.24)) implies $U_\infty^z = (2 - q)/3 = -0.3805$. Thus a tentative interpretation of the behavior seen in Fig. 5.9 is a slow crossover from bicritical behavior to first-order-scaling. With respect to U_*^{xy}, Fig. 5.12 did not indicate massive crossover behavior; but this can be understood since U_*^{xy} does not differ much from the first-order scaling prediction $U_\infty^{xy} \approx 0.56$. Thus, the crossover between these values is "masked" by the standard corrections to finite-size scaling.

For $T = 0.80J/k_B$, Fig. 5.10 shows that the cumulant crossing point for pair $L = (40, 50)$ is $U_L^z \approx -0.20(5)$. It looks similar to that for pair $L = (80, 100)$ at $T = 0.95J/k_B$. At $T = 0.60J/k_B$ (Fig. 5.11), the crossing point for pair $L = (32, 40)$ is $U_L^z \approx -0.40(7)$. This indicates that there is a more obvious first-order-scaling behavior as T decreases, which is further away from the bicritical point.

5.5 Discussion

In order to provide an understanding of the finite-size behavior of a first-order transition from a state with simple, discrete degeneracy to a state with an infinite degeneracy, we have performed both theoretical and simulational studies of a uniaxially anisotropic Heisenberg antiferromagnet on finite, simple cubic lattices in an external field H applied along the easy axis.

A phenomenological theory was presented based upon phase coexistence in the thermodynamic limit with probability distributions of the system in each phase described by delta functions. We hypothesized that the relative weights of the AF and SF phases are 2 and 2π by integrating over the angle ϕ of the two-component SF order parameter. For finite volume,

this description was generalized in terms of suitable Gaussian distributions, which led to the prediction that the moments and cumulants of the order parameters of both phases show common intersection points for large L at the transition field H^t (apart from corrections of order L^{-3}). The values predicted for these intersections depend upon the effective, relative degeneracy $q = \pi$. We then tested these somewhat speculative predictions via large scale Monte Carlo simulations.

We determined the finite-size behavior of the model by performing high resolution Monte Carlo simulations. The phase transition can be located quite precisely by using an equal height rule for the probability distribution for the internal energy, and we find that an "equal weight" rule applies for the order parameter at the transition. The locations of the minima in the cumulants for the antiferromagnetic order, spin-flop order, and internal energy extrapolate to the same transition field in the thermodynamic limit as does the "equal weight" rule for the magnetization as predicted by the double Gaussian approximation. Different predictions from the theory yield consistent values for the effective value of the degeneracy q but *only* for quite large values of L. Therefore, we conclude that the simple theory based upon a double Gaussian distribution provides a complete picture of the finite-size effects at first-order transitions between phases with different symmetries of the order parameters. Since the underlying theory does not depend on the fine characteristics of the model, this means that a heretofore unknown kind of universality at a first-order transition has been identified.

Chapter 6

Conclusion

In this work, we have investigated the finite-size behavior at phase transitions with very high precision by using extensive and careful Monte Carlo simulations with specialized algorithms.

In the case of a second-order transition, we have studied a 3D Ising model with the Wolff cluster flipping algorithm, histogram reweighting, and finite-size scaling including cross-correlations using quadruple precision arithmetic for the analysis. Using a wide range of system sizes, with the largest containing more than 10^9 spins, and including corrections to scaling, we have obtained results for the inverse critical temperature K_c as well as critical exponents ν and γ that are comparable in precision to those from the latest sophisticated theoretical predictions and can provide independent verification of the predictions from those methods. Our values provide further numerical evidence that none of the purported "exact" values are correct.

Also, we have determined the probability distribution $P(m)$ of the order parameter m at the critical temperature in a high-resolution manner. The high quality of the distribution permitted us to obtain a precise functional form to describe $P(m)$ in the thermodynamic limit. This expression for $P(m)$ and its parameters provide a valuable benchmark for comparison with results for other models presumed to be in the Ising universality class.

We have also explored the finite-size scaling for a first-order phase transition where a continuous symmetry is broken, and a theory was developed by using an approximation of Gaussian probability distributions with a phenomenological "degeneracy" factor, q, included. We implemented multicanonical Monte Carlo simulations on the three-dimensional, XXZ Heisenberg antiferromagnet in an external field in order to study the finite-size behavior on a $L \times L \times L$ simple cubic lattice for the first-order "spin-flop" transition between the Ising-like antiferromagnetic state and the canted, XY-like state.

For the "spin-flop" transition from a state with simple, discrete degeneracy to a state with an infinite rotationally degeneracy, our theory yielded the effective "degeneracy" factor $q = \pi$, and it predicted that for large linear dimension L the field dependence of all moments of the order parameters as well as the fourth-order cumulants exhibit universal intersections. The values of these intersections at the spin-flop transition point can be expressed in terms of the factor q, and corrections to leading order should scale as L^{-3}. Since the value of q is independent of the fine characteristics of the model (such as the temperature T and the uniaxial exchange anisotropy Δ), and the good agreement between our theory and simulation, it implies a heretofore unknown universality can be invoked for first-order phase transitions.

Bibliography

[1] D. P. Landau and K. Binder, *A Guide to Monte Carlo Simulations in Statistical Physics*, 4th ed. (Cambridge University Press, Cambridge, 2015).

[2] A. M. Ferrenberg, J. Xu, and D. P. Landau, Phys. Rev. E **97**, 043301 (2018).

[3] K. Binder, Z. Phys. B **43**, 119 (1981).

[4] S. El-Showk *et al.*, J. Stat. Phys. **157**, 869 (2014).

[5] S. Hu, S.-H. Tsai, and D. P. Landau, Phys. Rev. E **89**, 032118 (2014).

[6] H. Callen, *Thermodynamics and an Introduction to Thermostatistics*, 2nd ed. (Wiley, New York, 1985).

[7] M. Bachmann, *Thermodynamics and Statistical Mechanics of Macromolecular Systems*, 1st ed. (Cambridge University Press, Cambridge, 2014).

[8] H. E. Stanley, *Introduction to Phase Transitions and Critical Phenomena*, 1st ed. (Oxford University Press, Oxford, 1971).

[9] M. E. Fisher, Rev. Mod. Phys. **46**, 597 (1974).

[10] M. E. J. Newman and G. T. Barkema, *Monte Carlo Methods in Statistical Physics*, 1st ed. (Oxford University Press, Oxford, 1999).

[11] M. E. Fisher, in *Critical Phenomena*, edited by M. S. Green, pp. 1–98, Academic Press, New York, 1971.

[12] M. E. Fisher and M. N. Barber, Phys. Rev. Lett **28**, 1516 (1972).

[13] V. Privman, *Finite Size Scaling And Numerical Simulation Of Statistical Systems* (World Scientific, Singapore, 1990).

[14] K. Binder, in *Computational Methods in Field Theory*, edited by H. Gausterer and C. B. Lang, Springer, Berlin, 1992.

[15] N. Metropolis, A. W. Rosenbluth, M. N. Rosenbluth, A. H. Teller, and E. Teller, J. Chem. Phys. **21**, 1087 (1953).

[16] U. Wolff, Phys. Rev. Lett. **62**, 361 (1989).

[17] B. A. Berg and T. Neuhaus, Phys. Rev. Lett. **68**, 9 (1992).

[18] A. M. Ferrenberg and R. H. Swendsen, Phys. Rev. Lett. **61**, 2635 (1988).

[19] A. M. Ferrenberg and R. H. Swendsen, Phys. Rev. Lett. **63**, 1195 (1989).

[20] M. Weigel and W. Janke, Phys. Rev. Lett. **102**, 100601 (2009).

[21] M. Weigel and W. Janke, Phys. Rev. E **81**, 066701 (2010).

[22] M. N. Barber, in *Phase Transitions and Critical Phenomena*, edited by C. Domb and J. L. Lebowitz Vol. 8, pp. 146–266, Academic Press, New York, 1983.

[23] E. Ising, Z. Phys. **31**, 253 (1925).

[24] L. Onsager, Phys. Rev. **65**, 117 (1944).

[25] A. M. Ferrenberg and D. P. Landau, Phys. Rev. B **44**, 5081 (1991).

[26] Y. Ozeki and N. Ito, J. Phys. A: Math. Theor. **40**, R149 (2007).

[27] H. W. J. Blöte, J. R. Heringa, A. Hoogland, E. W. Meyer, and T. S. Smit, Phys. Rev. Lett. **76**, 2613 (1996).

[28] G. S. Pawley, R. H. Swendsen, D. J. Wallace, and K. G. Wilson, Phys. Rev. B **29**, 4030 (1984).

[29] R. Guida and J. Zinn-Justin, J. Phys. A **31**, 8103 (1998).

[30] A. A. Pogorelov and I. M. Suslov, J. Exp. Theor. Phys. **106**, 1118 (2008).

[31] P. Butera and M. Comi, Phys. Rev. B **65**, 144431 (2002).

[32] A. Pelissetto and E. Vicari, Phys. Rep. **368**, 549 (2002).

[33] A. Rosengren, J. Phys. A: Math. Gen. **19**, 1709 (1986).

[34] M. E. Fisher, J. Phys. A: Math. Gen. **28**, 6323 (1995).

[35] S. El-Showk *et al.*, Phys. Rev. D **86**, 025022 (2012).

[36] F. Kos, D. Poland, D. Simmons-Duffin, and A. Vichi, J. High Energ. Phys. **2016**, 36 (2016).

[37] M. Hasenbusch, Phys. Rev. B **82**, 174433 (2010).

[38] J. Kaupužs, J. Rimsans, and R. V. N. Melnik, Ukr. J. Phys. **56**, 845 (2011).

[39] J. Kaupužs, R. V. N. Melnik, and J. Rimsans, ArXiv e-prints (2014), 1407.3095.

[40] S. Wang, Z.-Y. Xie, J. Chen, B. Normand, and T. Xiang, Chin. Phys. Lett. **31**, 070503 (2014).

[41] Z. Zhang, Phil, Mag. **87**, 5309 (2007).

[42] F. Wu, B. M. McCoy, M. E. Fisher, and L. Chayes, Phil. Mag. **88**, 3093 (2008).

[43] F. Wu, B. M. McCoy, M. E. Fisher, and L. Chayes, Phil. Mag. **88**, 3103 (2008).

[44] M. E. Fisher and J. H. H. Perk, Phys. Lett. A **380**, 1339 (2016).

[45] H. W. J. Blote, E. Luijten, and J. R. Heringa, Journal of Physics A: Mathematical and General **28**, 6289 (1995).

[46] M. Matsumoto and T. Nishimura, ACM Trans. Model. Comput. Simul. **8**, 3 (1998).

[47] N. Ito and G. A. Kohring, Physica A **201**, 547 (1993).

[48] A. Aharony and M. E. Fisher, Phys. Rev. B **27**, 4394 (1983).

[49] M. Campostrini, A. Pelissetto, P. Rossi, and E. Vicari, Phys. Rev. E **65**, 066127 (2002).

[50] J. Kiefer, P. Am. Math. Soc. **4**, 502 (1953).

[51] B. Efron and R. J. Tibshirani, *An Introduction to the Bootstrap* (Chapman and Hall, New York, 1993).

[52] M. S. Guskova, L. Y. Barash, and L. N. Shchur, Comput. Phys. Commun. **200**, 402 (2016).

[53] A. Ferrenberg, D. P. Landau, and Y. Wong, Phys. Rev. Lett. **69**, 3382 (1992).

[54] K. Binder, Z. Phys. B **43**, 119 (1981).

[55] R. Hilfer and N. B. Wilding, J. Phys. A: Math. Gen. **28**, L281 (1995).

[56] M. M. Tsypin and H. W. J. Blöte, Phys. Rev. E **62**, 73 (2000).

[57] J. Wang, Z. Zhou, W. Zhang, T. M. Garoni, and Y. Deng, Phys. Rev. E **87**, 052107 (2013).

[58] H. W. J. Blöte, L. N. Shchur, and A. L. Talapov, Int. J. Mod. Phys. C **10**, 1137 (1999).

[59] Y. Deng and H. W. J. Blöte, Phys. Rev. E **68**, 036125 (2003).

[60] D. S. Gaunt, in *Phase Transitions, Proc. 1980 Cargese Summer Institute*, edited by M. Levy, J. C. Le Guillou, and J. Zinn-Justin, Plenum, New York, 1982.

[61] J. Adler, J. Phys. A : Math. Gen. **16**, 3585 (1983).

[62] D. P. Landau and K. Binder, Phys. Rev. B **17**, 2328 (1978).

[63] R. Folk, Y. Holovatch, and G. Moser, Phys. Rev. E **78**, 041124 (2008).

[64] G. Bannasch and W. Selke, Eur. Phys. J. B **69**, 439 (2009).

[65] W. Selke, Phys. Rev. E **83**, 042102 (2011).

[66] J. Xu, S.-H. Tsai, D. P. Landau, and K. Binder, Phys. Rev. E **99**, 023309 (2019).

[67] M. E. Fisher and D. R. Nelson, Phys. Rev. Lett. **32**, 1350 (1974).

[68] C. J. Gorter and T. Van Peski-Tinbergen, Physica **22**, 273 (1956).

[69] D. P. Landau, Phys. Rev. B **13**, 2997 (1976).

[70] K. Binder and D. P. Landau, Phys. Rev. B **30**, 1477 (1984).

[71] C. Borgs and R. Kotecký, J. Stat. Phys. **61**, 79 (1990).

[72] M. S. S. Challa, D. P. Landau, and K. Binder, Phys. Rev. B **34**, 1841 (1986).

[73] M. E. Fisher, AIP Conf. Proc. **24**, 273 (1975).

[74] D. R. Nelson, J. M. Kosterlitz, and M. E. Fisher, Phys. Rev. Lett. **33**, 813 (1974).

[75] J. M. Kosterlitz, D. R. Nelson, and M. E. Fisher, Phys. Rev. B **13**, 412 (1976).

[76] O. G. Mouritsen, E. K. Hansen, and S. J. K. Jensen, Phys. Rev. B **22**, 3256 (1980).

[77] P. Calabrese, A. Pelissetto, and E. Vicari, Phys. Rev. B **67**, 054505 (2003).

[78] J. Plascak, , J. Magn. Magn. Mater. **468**, 224 (2018).

[79] R. B. Potts, Math Proc. Cambridge **48**, 106109 (1952).

[80] F. Y. Wu, Rev. Mod. Phys. **54**, 235 (1982).

[81] L. D. Landau and E. M. Lifshitz, *Statistical Physics*, 3rd ed. (Elsevier, Amsterdam, 1980).

[82] K. Vollmayr, J. D. Reger, M. Scheucher, and K. Binder, Z. Phys. B **91**, 113 (1993).

[83] M. E. Fisher and V. Privman, Phys. Rev. B **32**, 447 (1985).

[84] K. Chen and D. P. Landau, Phys. Rev. B **46**, 937 (1992).

[85] M. E. Fisher, M. N. Barber, and D. Jasnow, Phys. Rev. A **8**, 1111 (1973).

[86] K. Binder, Phys. Rev. A **25**, 1699 (1982).

[87] J. Lee and J. M. Kosterlitz, Phys. Rev. Lett. **65**, 137 (1990).

[88] C. Holm and W. Janke, Phys. Rev. B **48**, 936 (1993).

[89] M. Campostrini, M. Hasenbusch, A. Pelissetto, P. Rossi, and E. Vicari, Phys. Rev. B **65**, 144520 (2002).